Doctoral Programme in Materials Research and Nanoscience
Division of Pharmaceutical Biosciences
Faculty of Pharmacy
University of Helsinki

BIOPHOTONICS IN BIOPHARMACEUTICAL APPLICATIONS

Jacopo Zini

DOCTORAL DISSERTATION

To be presented for public discussion with the permission of the Faculty of Pharmacy of the University of Helsinki, in Auditorium 2014, Biocenter 2, on the 10th of June 2022 at 12 noon.

Helsinki 2022

ISBN 978-951-51-8212-8 (softcover)
ISBN 978-951-51-8213-5 (PDF)

Unigrafia Oy
Helsinki, Finland 2022

This thesis was examined with Urkund system for plagiarism recognition

Supervisor: **Professor Marjo Yliperttula**
Division of Pharmaceutical Biosciences
Faculty of Pharmacy
University of Helsinki
Finland

Professor Tapani Viitala
Division of Pharmaceutical Chemistry and Technology
Faculty of Pharmacy
University of Helsinki
Finland
and
Laboratory of Pharmaceutical Sciences
Faculty of Natural Sciences and Engineering
Åbo Akademi University
Finland

PhD Heikki Saari
Finnish Red Cross Blood Service
Finland

Reviewers: **Assistant Professor, Randy P. Carney**
Department of Biomedical Engineering
Collage of Engineering
University of California
Davis
The United States

Professor Jouko Peltonen
Laboratory of Molecular Science and Engineering
Åbo Akademi University
Finland

Opponent: **Professor Sebastian Wachsmann-Hogiu**
Bioengineering
Faculty of Engineering
McGill University
Montreal
Canada

Cerca Trova

ABSTRACT

Biopharmaceutical products are composed of proteins, lipids, sugars, nucleic acids, complex and ordinate combinations of these substances, or living cells or tissues. In contrast with completely synthetic pharmaceuticals, biopharmaceuticals are derived entirely or partially from a biological source. Owing to the intrinsic variability of biological systems and the biochemical complexity of the bioprocesses involved in the development and production of these products, new technologies are required to monitor and characterise both the production processes and final products. Ideally, such methods should be rapid, robust, operator-independent, non-destructive, and label-free. Bio-photonics techniques, particularly Raman and infrared (IR) spectroscopy, fit this description. Bio-photonics is a broad and multidisciplinary field in which our understanding of the physics of light and its interaction with matter is combined with the fundamental phenomena of materials in the life sciences to reveal their chemical, physical, and physiological characteristics. The primary objective of this thesis is to confront the current limitations of bio-photonics in the field of extracellular vesicles (EVs) and highlight the development of their instrumentation to overcome several unsolved issues in the fields of EVs and biopharmaceuticals.

EVs are a heterogeneous population of lipid bilayer nanoparticles that are released by any type of cell involved in cell-to-cell communication. Because of their role as natural biomolecule carriers, EVs can potentially be utilised in drug delivery or liquid biopsy for diagnostic purposes. Despite high interest and the number of publications and EV-focussed societies, there are currently no clinical applications of EVs or regulated EV production processes. This is due to the novelty of this relatively new field and the challenges involved in purifying and characterising EVs, which cause difficulties in comparing the results obtained by different research groups.

In this study, I first investigated the applicability of Raman and IR spectroscopy as methods of characterising and assessing the quality of EV suspensions with different degrees of purity. Similar to traditional characterisation methods for EV suspensions, Raman and IR spectroscopy were also able to assess EV purity and characterise EV suspension. Furthermore, these vibrational spectroscopic techniques exhibit different intrinsic advantages because they are label-free and operator-independent. Particularly, Raman spectroscopy may be the most suitable technology because it is less sensitive to water than IR. Raman spectroscopy reveals information on the chemical composition and physical status of an analyte; however, it does not provide information on the environment of the analyte. This information can be gathered by spectrofluorometry. EV trafficking, diffusion, and interactions *in vitro* with cells and *in vivo* with tissues are typically studied using fluorescence-based microscopy methods. However, for spectrofluorometry, EVs must be labelled with a fluorescent dye. Results obtained by fluorescence lifetime imaging spectroscopy highlight the feasibility of the cell uptake of fluorescently labelled EVs; however, attention must be paid to the efficacy of the labelling and the elimination of the

unbound dye because these may severely compromise the results or lead to wrong conclusions on EV functionality.

In a previous study, the combined advantages of Raman spectroscopy and fluorescence decay were obtained using a previously in-house developed Raman spectrometer based on a time-resolved complementary metal-oxide-semiconductor (CMOS) single-photon avalanche diode (SPAD) line sensor. CMOS technology enables the integration of all time-correlated single-photon counting (TCSPC) electronics, thus enabling time-resolved measurement. In such a method, the width of the time gate, which is used to separate the Raman signal from the fluorescence tail, can be modified, even in the data post-processing phase, to obtain the best possible Raman signal-to-noise ratios.

The simultaneously-detected Raman spectra and time-resolved fluorescence decay curves were used to study the diffusion of small molecular drugs in a hydrogel. These spectra together can reveal a sample's chemical composition, physical status, and interaction with the environment. Taken together, the obtained results suggest that the quality of EV suspensions can be assessed by Raman spectroscopy, their cell uptake by fluorescence lifetime spectroscopy, and both Raman spectra and fluorescence decay can be measured simultaneously by a second-generation time-resolved Raman spectrometer.

ACKNOWLEDGEMENTS

This work was carried out at the Division of Pharmaceutical Biosciences, Faculty of Pharmacy, University of Helsinki, funded by professor Yliperttula's Academy of Finland projects and Business Finland EVE ecosystem. In these my doctoral studies, I had the pleasure to work with the Biopharmacy research group of Helsinki University, as well as Oulu and Tampere University. To everyone, I would like to offer my sincere gratitude, as it has been a privilege work with you all.

I wish to thank my supervisors: Professor Marjo Yliperttula, Professor Tapani Viitala and doctor Heikki Saari. I am very grateful for your guidance and support throughout these years.

To Professor Marjo Ylipertulla, I will be forever grateful for taking me in her group as PhD student. Since the beginning of my experience in the Biopharmacy research groups, Marjo let me work independently, supported my ideas and give me the freedom to experiment with new things.

Professor Tapani Viitala has been an outstanding supervisor, thanks for your positive attitude, for encouraging me and for proofreading my EV paper, all 6 final versions of it.

When I started my experience as exchange student here in Helsinki, I was teamed up with Heikki Saari, not yet doctor back then. You have been decisive for my work here in Helsinki, I could always trust your advice and, thanks to your trainings, I gained the confidence to work independently in the lab, to try new things and solutions.

I could write more, but I know you prefer concise and practical things, so I´ll just add: 👍

I would like also to thanks Doctor Jukka Saarinen and Timo Laaksonen. Jukka has been, practically, an unofficial supervisor. You have helped me to improve my understanding of vibrational spectroscopy as well as my running; I have really appreciated our conversation and your encouragement in try new application for Raman and EVs. Timo, I appreciated your work methods and critical thinking, it has been great work with you. And thanks for suggesting the Japanese karaoke back in Kyoto, it was a fun experience.

It is my honour to have Sebastian Wachsmann-Hogiu from McGill University as my opponent, and I greatly appreciate his interest for my work and for the time he took for thesis defense. I would also to thanks my pre-examiners Assistant Professor, Randy P. Carney University of California and Professor Jouko Peltonen Åbo Akademi University and the members of my thesis committee, Jessica Rosenholm from Åbo Akademi and Helder Santos from Helsinki University for the valuable feedbacks.

I would also like to thanks my all my co-author from Oulu University; Ilkka Nissinen and Jere Kekkonen, and from Tampere Univeristy; Kaisa Rautaniemi, Ekaterina Lisitsyna and Elina Vuorimaa-Laukkanena.

Working at the biopharma group gave me the opportunity to meet and work with great people. To Arto, Jasmi, and Elle we have had many great trip, and I have such

great memories of traveling to the GPEN and the other conferences. I am so sorry COVID arrived and had to cancel some of them.

Work in the lab would have been much more difficult without the guidance of Leena Pietilä and Timo Oksanen, I wish to thank you for all the problems and troubles you have helped me to solve in these years.

This thesis would have been impossible to complete without the invaluable work and support of Riina, Raili, Patrick, Sami, Ossi, Giulia, Lisa, Julia, Laura, Kalle and Andres, so thanks you!

I want also to thanks Jaakko, Sirin and Sina for the lunches and coffee breaks. And the "younger" Saara and Ann-Mari of Turku University (Marjo, if you are reading this maybe you should change the name of their group), you have done a great effort in setting up a new cell lab, you both are intelligent and motivated, just don´t stress too much about the contaminations.

Lastly, I want to thanks my friend form the rowing club, my parents and my siblings for they support. A special mention goes to my sister Maria Giulia, who actually helped me to understand some mathematical issue explained further in this work.

Jacopo
Helsinki
June 20220

CONTENTS

LIST OF ORIGINAL PUBLICATIONS

This thesis is based on the following publications:

I **Jacopo Zini**, Heikki Saari, Paolo Ciana, Tapani Viitala, Andres Lõhmus, Jukka Saarinen, Marjo Yliperttula. Infrared and Raman spectroscopy for purity assessment of extracellular vesicles. Journal of European Pharmaceutical Sciences 172 (2022) 106135, https://doi.org/10.1016/j.ejps.2022.106135

II Kaisa Rautaniemi, **Jacopo Zini**, Emilia Lofman, Heikki Saari, Iida Haapalehto, Johanna Laukka, Sami Vesamaki, Alexander Efimov, Marjo Yliperttula, Timo Laaksonen, Elina Vuorimaa-Laukkanen and Ekaterina S. Lisitsyna. Addressing challenges in the removal of unbound dye from passively labelled extracellular vesicles. Advanced article published in Nanoscale Advances on 23.11.2021, https://doi.org/10.1039/D1NA00755F

III **Jacopo Zini**, Jere Kekkonen, Ville A. Kaikkonen, Timo Laaksonen, Pekka Keranen, Tuomo Talala, Anssi J. Makynen, Marjo Yliperttula, Ilkka Nissinen. Drug diffusivities in nanofibrillated cellulose hydrogel by combined time-resolved Raman and fluorescence spectroscopy. Journal of Controlled Release 334 (2021) 367-375, https://doi.org/10.1016/j.jconrel.2021.04.032

LIST OF ADDITIONAL PUBLICATIONS

Additional publications, which are not included in the experimental part of this Thesis are listed below.

1 Arto Merivaara, **Jacopo Zini**, Elle Koivunotko, Sami Valkonen, Ossi Korhonen, Francisco M Fernandes, Marjo Yliperttula. Preservation of biomaterials and cells by freeze-drying: Change of paradigm. Journal of Controlled Release 336 (2021) 480-498, https://doi.org/10.1016/j.jconrel.2021.06.042

2 Elle Koivunotko, Arto Merivaara, Akseli Niemelä, Sami Valkonen, Kalle Manninen, Henrik Mäkinen, Mira Viljanen, Kirsi Svedström, Ana Diaz, Mirko Holler, **Jacopo Zini**, Lauri Paasonen, Ossi Korhonen, Simo Huotari, Artturi Koivuniemi, Marjo Yliperttula. Molecular Insights on Successful Reconstitution of Freeze-Dried Nanofibrillated Cellulose Hydrogel. Applied Bio Materials, 2021, 4, 9, 7157–7167, https://doi.org/10.1021/acsabm.1c00739

LIST OF ABBREVIATIONS

2D	two-dimension
3D	three-dimension
AD	Alzheimer's disease
AEC	anionic exchange chromatography
AFM	atomic force microscope
ANFC	anionic nanofibrilated cellulose
ATR	attenuated total reflectance
AUC	area under the curve
BBL	Bouguer-Beer-Lambert Law
BCA	bicinchoninic acid assay
BM	biomarker
BP	4,4-difluoro-1,3,5,7,8-pentamethyl-4-bora-3a,4a-diaza-s-indacene
BPC12	4,4′-difluoro-4-bora-3a,4a-diaza-s-indacene meso-substituted with para-dodecylphenyl moiety
BPM	biotinylated protein mixture
CARS	Coherent anti-Stokes Raman spectroscopy
CCM	cell conditioned media
CMOS	metal-oxide-semiconductor
CW	continuous wavelength
DC	differential centrifugation
DHPE-OG	Oregon Green™ 488 1,2-dihexadecanoyl-sn-glycero-3-phosphoeth
DiO	3,3′-dioctadecyloxacarbocyanine perchlorate
DLS	dynamic light scattering
DLS	dynamic light scattering
DPBS	Dulbecco′s phosphate buffered saline
EMA	European Medicines Agency
EP	European pharmacopea
ESCRT	endosomal sorting complexes required for transport
EV	extracellular vesicle
FDA	Food and Drug Administration
FLIM	fluorescence lifetime microscopy
FLT	fluorescence lifetime
FRET	Förster resonance energy transfer
FT	Fourier transform
G	density gradient centrifugation
HVCMOS	high-voltage complementary metal-oxide-semiconductor
IR	infrared
LDA	linear discriminant analysis
Li/Pr	lipid to protein ratio

MALS	multi angle light scattering
MHC -I	class I major histocompatibility complex
MHC -II	class II major histocompatibility complex
MS	mass-spectrometry
MV	microvesicle
MVB	multi-vesicular body
MW	molecular weight
NIR	near IR
NTA	nanoparticle tracking analysis
Pa/Pr	particles to protein ratio
PAT	process analytical technology
PCA	principal component analyses
PLS	partial least square
Ptx-OG	Oregon Green 488 taxol
QbD	quality by design
RI	refractive index
RRS	resonance Raman spectroscopy
RT	room temperature
SEC	size exclusion chromatography
SERS	surface enhanced Raman spectroscopy
SPAD	single-photon avalanche diode
SPR	surface plasmon resonance
SRG	stimulated Raman gain
SRL	stimulated Raman loss
SRS	stimulated Raman spectroscopy
TEM	transmission electron microscopy
TERS	tip enhanced Raman spectroscopy
TG-Raman	time gated Raman
ToA	time of arrival
UF	ultrafiltration
UV	ultra-violet
VIS	visible light
WB	western blot

1 INTRODUCTION

Modern physics considers light composed of photons as elementary particles that possess both wave- and particle-like attributes. Photonics belongs to the natural sciences and biophotonics to the biosciences, both of which study the generation, detection, and interaction of photons with matter.

The concept of the photon was discovered by Einstein[1] in 1905, In his 'photoelectric paper', he purposed the idea of *light quanta* as blackbody radiation that distributes energy within the increasing volume-dependence of entropy. This quantum theory of light represents the idea that light exists as tiny packets, or particles, which are known as photons. These photons can be generated and absorbed only as complete units. However, the term photons was coined by Lewis in 1925 to describe something that plays an essential part in every radiation process.[2]

Owing to the efforts of scientists, our understanding of the nature of light and photons is increasing exponentially; a paradoxical nature of photons has become more evident than the 'simple' model Einstein conceived.

Among these efforts, theorisation and fundamental work by Townes, Basov, and Prokhorov (Nobel prize in 1964 for the maser-laser principle) in the field of quantum electronics, which led to the construction of oscillators and amplifiers, are particularly relevant for this PhD thesis. Light amplification via the stimulated emission of radiation, known as laser light, opened up a new field of science known as photonics. Over the years, a range of different and exotic phenomena have been described in the photonics and biophotonics fields, which has led to new applications and a deeper understanding of natural phenomena.

In this thesis, I focus on a particular area of photonics known as biophotonics, which is a multi-disciplinary combination of biology and technology for generating, manipulating, and detecting photons, applied to biopharmaceutical sciences.

Biophotonics have gained an important role in the life and medical sciences as a tool for cell imaging (both two-dimensional (2D) and three-dimensional (3D)), non-invasive measurements of metabolites, such as glucose and blood oxygen levels, the detection of diseased cells or tissues and their therapeutic treatment, and surgical procedures. Moreover, the same technology can be applied in the pharmaceutical field and in different steps within biopharmaceutical production, from raw material control, throughout bioprocess monitoring, and final product quality.

To achieve different applications, biophotonic methods rely on various technologies to generate photons with different intensities and wavelengths and investigate their emission and detection. Despite the broad use of different technologies, the wavelength used in biophotonics typically ranges from 190 nm to 10.6 μm, which includes the infrared (IR), visible (VIS), and ultra-violet (UV) regions of the electromagnetic spectrum (Figure 1).

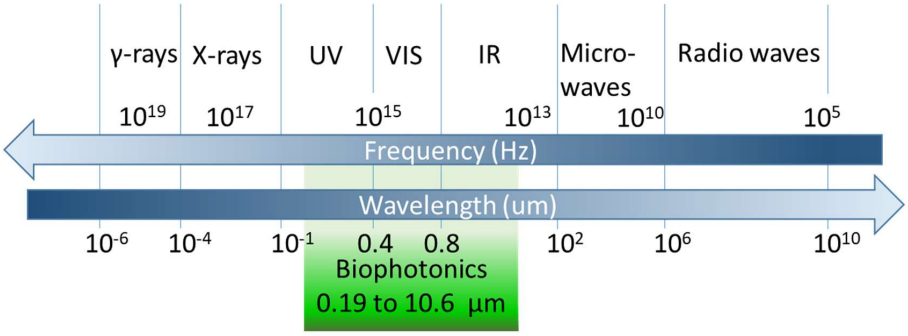

Figure 1 Spectrum of electromagnetic radiation. The frequencies utilised in bio-photonics are highlighted in green.

Light can be described as electromagnetic waves that move perpendicular to the direction in which the wave travels. To describe wave optics, we can focus on the characteristics of a monochromatic wave that consist of a sine wave of infinite extent with an amplitude A and wavelength λ.

The International Standards Organization (ISO) gives specific ranges for the photon energies and wavelengths of the spectral areas used in photonics (Figure 1). When photons with different energies interact with matter, different phenomena can occur. Low-energy photons (that is, long wavelengths and low frequencies), such as radio waves, can magnetically induce changes in the spin states of electrons. Furthermore, microwaves cause molecular rotations, IR radiation induces molecular vibrations, and visible light can lead to the transition of valence electrons. High-energy photons may result in molecular and atomic ionisation (UV, mainly UV-C), the transition of electrons in the inner shells of atoms (X-ray), or nuclear reactions (gamma rays). Regarding biophotonics, we are mostly interested in the electromagnetic spectrum between 190 nm and 10.6 µm (approximately 6.5–0.23 eV). Within this energy range, electromagnetic radiation results in vibrational transitions, associated with IR absorption and Rayleigh, Stokes, and anti-Stokes scattering, or electron transitions, which results in fluorescence phenomena. The Jablonski diagram in Figure 2 shows several of the electronic states (S_0 and S_1), the vibrational energy level (0, 1, 2, and 3) of a molecule, and transitions between the electronic states and vibrational energy level caused by interaction with the incident photon. At room temperature, most molecules are in the ground vibrational state because thermal energy is insufficient to significantly populate the excited vibrational states. Following light absorption, electrons can either be excited to a higher electronic state (S_0 to S_1 or S_2) or vibrational level (0 to 1 or 2) or to a virtual excited state. This last state is not a real molecular state and is only created once polarisation is induced by the interaction of matter with light. The energy of the virtual excited state depends on the frequency of the light. Independent of whether the electronic state or vibration level is reached, molecules return to the S_0 level. Fluorophores are excited to a higher vibrational level of S_1 or S_2, with rare exceptions, and relax to the lowest vibrational level of S_1. This radiationless process, known as internal conversion, generally occurs in 10^{-12} s.

Subsequently, a radiative transition between two electronic states (S_1 to S_0) of the same spin multiplicity occurs (10^{-10}–10^{-7} s). This transition implies the release of a red-shifted photon. Otherwise, molecules in the S_1 state can convert to the first triplet state T_1 (not shown in the figure). This conversion indicates spin conversion and is known as an intersystem crossing; it is the basis of phosphorescence phenomena.

Different vibrational energy states occur within the electronic state. These states are caused by the periodic motion (vibration) of the atoms within the molecule. The different types of vibrations are shown in Figure 3.

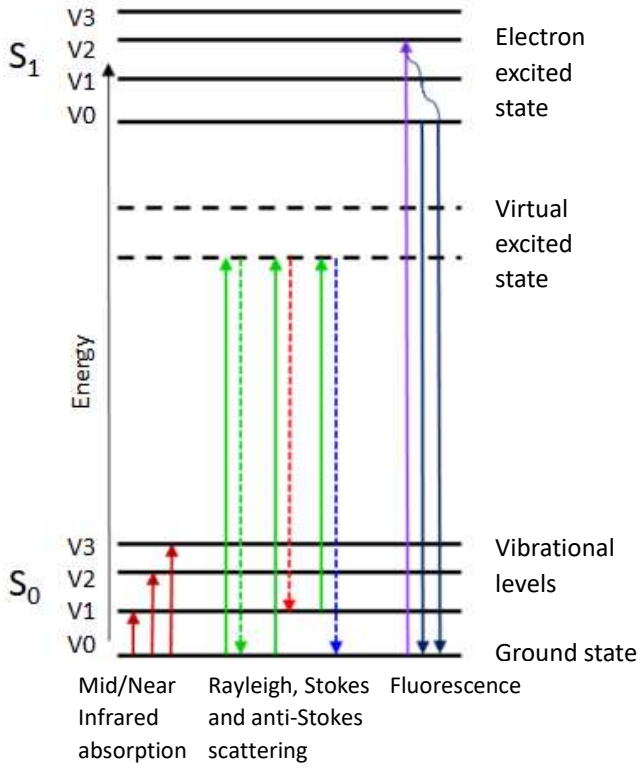

Figure 2 Jablonski diagram. Dark red arrows represent the absorption of near and mid-infrared radiation, which are measured using IR spectroscopy. Green arrows show the absorption of photons, which occurs in Rayleigh, Stokes, and anti-Stokes scattering, while the dashed arrows indicate radioactive relaxation in Rayleigh (green), Stokes (red), and anti-Stokes (blue) scattering. (Figure adapted from Principle of Fluorescence Spectroscopy, J.R. Lakowic, 3rd edition).

Vibrational spectroscopy techniques, such as Raman and IR spectroscopy, are based on the following phenomena: IR spectroscopy measures the absorption, emission, or reflection of IR light, which occur when there are changes in the dipole moment during vibration. Rayleigh, Stokes, and anti-Stokes scattering are a result of photons released by the relaxation of an electron previously excited from the ground state to a virtual excited state. The scattered photon can have the same energy as the

incident photon (Rayleigh scattering) or a different energy, that is, a lower energy in Stokes and a higher energy in anti-Stokes scattering. In particular, Raman spectroscopy is based on inelastic scattering (Stokes) and detects changes in polarisability in the molecule.

At a first glance, fluorescence and Stokes scattering are similar phenomena; both involve the emission of photons that are shifted in frequency relative to the incident light. However, fluorescence implies the excitation of photons to a higher energy state (S_1 or S_2), whereas in Stokes scattering, there is no excited state, only a short-lived virtual excited state. This difference is reflected in the 'speed' of emission: Raman scattering is an immediate phenomenon (10^{-15}–10^{-12} s), whereas fluorescence generally occurs within 10^{-12}–10^{-7} s. Additionally, fluorescence is a far more common phenomenon and is thus more intense than the Raman effect. This can result in interference between Raman and fluorescence detection, with the fluorescence signal overwhelming the Raman signal. This is one of the most common disadvantages of Raman spectroscopy and is common in many different pharmaceutical and biopharmaceutical applications.[3]

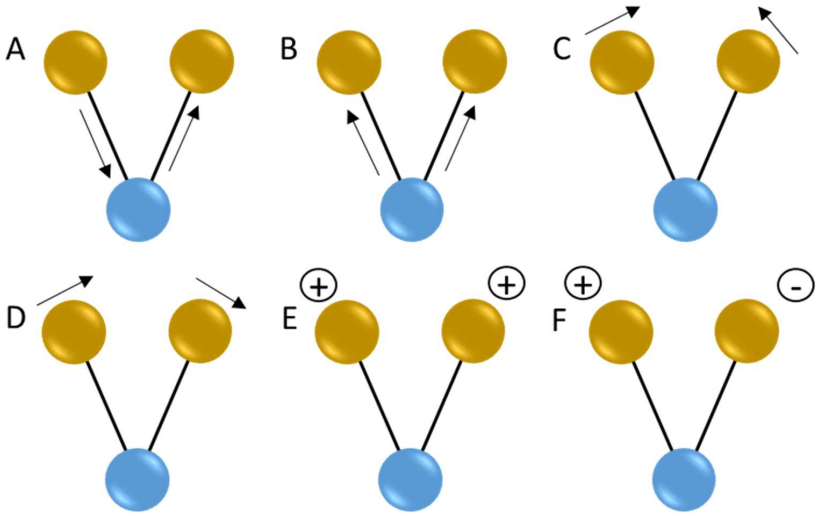

Figure 3 Molecular vibrations of the XY_2 group. (A) Asymmetric stretching, (B) symmetric stretching, (C) scissoring, (D) rocking, (E) wagging, and (F) twisting. Circles with + indicate atoms moving out of the page plane, while circles with – indicate atoms moving into the page plane. Figure adapted from J. Saarinen, 2018.[4]

Biophotonics techniques are rapidly gaining interest in the biopharmaceutical field. Among these techniques, Raman spectroscopy displays unique ductility.[5] However, its routine use is partially prevented by the interference of fluorescence.

In this study, I applied three different biophotonics techniques, namely IR and Raman spectroscopy and fluorescence lifetime microscopy (FLIM). IR spectroscopy,

Raman spectroscopy, and FLIM were used to study the properties of extracellular vesicles (EVs) extracted from *in vitro* cell cultures.

EVs are a heterogeneous group of lipid-enveloped nanoparticles released by cells in all biological fluids, where they act as natural carriers. Owing to this role, numerous research groups are exploring the possible use of EVs as diagnostic tools or drug delivery systems. The study of EVs is challenging; EV preparation is heterogeneous, biochemically complex, contains a wide range of impurities, and has no standard method for the characterisation or assessment of sample purity. In this context, biophotonic methods, particularly vibration spectroscopy, could play a decisive role in the implementation of medical applications of EVs. Raman and IR spectroscopy can both be used to resolve the chemical composition of complex samples; thus, they can potentially find a role in either diagnostic methods based on EVs or as a quality control tool. In this study, the characteristics of EV preparation purified with different purification protocols were compared with IR and Raman spectroscopy and further labelled by various fluorescent molecules for cell uptake studies with FLIM. Finally, a second-generation time-resolved fluorescence Raman spectrometer coupled with a sensor utilising time-gated single-photon avalanche diodes (SPADs) fabricated as a standard high-voltage complementary metal-oxide-semiconductor (HVCMOS) was constructed and used to investigate the diffusion of small drugs in a biomaterial hydrogel.

2 REVIEW OF LITERATURE

2.1 INFRARED SPECTROSCOPY

IR spectroscopy studies the interaction of infrared light with matter. IR spectroscopy is used to obtain information on both the chemical and structural properties of a sample, originating from the vibrations of different functional groups that depend on the wavelengths absorbed. IR spectroscopy was developed in the 1940s for the identification of organic compounds in the petrochemical field.

IR absorption is a one-photon phenomenon that occurs when a beam of IR light passes through a sample that absorbs the IR frequency, which is equal to the vibrational frequency of the functional group of the studied sample.

IR spectra are presented as 2D Cartesian coordinate systems, where the *x*-axis represents the frequency in wavelengths (μm) or wavenumbers (cm^{-1}), and the *y*-axis is the intensity in transmittance (%) or absorbance.

The frequency of the IR absorption of a particular functional group in a molecule depends on the mass of the atoms and the nature of their bonds according to Hook´s law for harmonic oscillation (eq. 1).

(1) $$f = \frac{1}{2\pi}\sqrt{\frac{k}{u}} \quad ,$$

(2) $$u(AB) = \frac{mA\ mB}{mA+mB} \quad ,$$

where *k* is the spring constant of the bond between atoms A and B in the molecule, and *u* is the reduced mass of the AB system.

Atoms in the functional groups of molecules with a high bond order, such as alkynes, will vibrate at a high frequency, whereas in molecules that have functional groups with a low bond order, such as alkenes, the atoms vibrate at a lower frequency. The mass of the atoms also affects the frequency; atoms with high masses generate high *u*, and thus the vibrations occur at a low frequency. However, the intensity is due to the derivation of the dipole moment with respect to interatomic distances in intramolecular systems. Overall, the absorption can be assumed to be proportional to the molar dielectric coefficient ε, concentration *c,* and path length *l*, as summarised by the Bouguer–Beer–Lambert Law (BBL) (eq. 3).

(3) $$A \approx l\ \varepsilon\ c.$$

The linearity of the BBL law is not always respected in IR spectroscopy. Chemical and instrumental factors might cause deviation from the linearity of the BBL law. For instance, high concentrations of samples might induce changes in the refractive index (RI), leading to deviations in ε owing to electrostatic interactions between molecules

in proximity to each other. Moreover, fluorescent and phosphorescent scattering of light due to particulates in the sample will also affect the linearity of the BBL law. Nevertheless, this law and its derivations are routinely used for the quantification of biomolecules from IR data, or more commonly, using partial least squares (PLSs) and principal component analyses (PCA) of the data.[6]

There are different ways in which IR light can be focussed on the sample and spectra can be recorded. The most immediate method is transmission, where IR radiation is transmitted through the sample, and the resulting transmitted radiation is recorded. This method requires sample preparation, that is, solid samples must be dispersed in an IR transparent substrate (for example, KBr, CaF_2), which does not have good mechanical properties.[7] During transfection, the sample is placed on an IR reflective substrate, and the absorption of the IR radiation is recorded after the IR light transits through the sample, reflects off the substrate, and transits again through the sample. The absorption data might be non-linearly distorted with respect to thickness, leaving quantitative measurement unreliable.[8] The attenuated total reflectance-Fourier transform IR (ATR-FTIR) is probably the most popular measurement configuration. ATR partially compensates for the disadvantages of the two IR techniques mentioned above. ATR-FTIR consists of placing the sample in intimate contact with a crystal (for example, diamond, beryllium), and IR radiation is directed into this crystal above its critical angle. The critical angle depends on the crystal material and is a function of the refractive indices of the two surfaces, that is, the crystal and sample. Subsequently, the light 'bounces' through the crystal and is collected. The 'bounces' are the flexing points of the propagating light, and evanescent waves are generated at these points. Thus, chemical information on the samples is obtained by the interaction of the evanescent waves and samples, which is then carried by the IR radiation to the detector. The evanescent waves are standing waves, which propagate through the samples at a certain penetration depth (D_p). In ATR-IR, the path length is the sum of the D_p values of the evanescent waves. D_p is affected by the wavenumber of the light, the angle at which the light interacts with the crystal surface, and the RI of the crystal. Light with a low wavenumber (that is, high wavelength, low energy) penetrates deeper into the samples than IR radiation with a high wavenumber. D_p decreases when the angle of incidence decreases and the RI of the crystal is high. Commonly used crystal diamonds have an RI of 2.4 and a D_p of 2 μm, whereas Germanium crystals have an RI of 4 and a D_p of 0.4 μm.

2.1.1 BIOPHARMACEUTICAL APPLICATIONS OF IR SPECTROSCOPY

IR spectroscopy is widely used in the pharmaceutical industry,[9] both in production and research and development. IR spectroscopy is cited 1353 times in the 10th edition of European Pharmacopoeia (EP10). EP10 allows the use of IR spectroscopy for chemical and physical analysis. It highlights the applicability of IR spectroscopy in the identification and quality assessment of active substances, excipients, manufacturing intermediates, chemicals, and packaging materials, including batch-to-batch comparison. Moreover, IR spectroscopy, among others, can be applied for on-line monitoring of chemical synthesis, the determination of polymorphism, the

quantification of active substances in a sample matrix, the determination of water and solvent content, and the quantification of impurities. However, EP10 also underlines the limitations of IR spectroscopy because IR spectroscopy might be unable to unambiguously identify a substance. Additional techniques may, therefore, be required. The identification or determination of low concentrations of substances via IR spectroscopy might be difficult, especially if the compounds are not highly IR active. Moreover, IR spectroscopy exhibits limitations in the analysis of heterogeneous samples and is unable to, for example, discriminate between the pure enantiomers of molecules. Lastly, EP10 highlights the possibility of using IR spectroscopy as a process analytical technology (PAT) tool for advanced control strategies.

Biopharmaceutical applications of IR spectroscopy are related to the quantification and identification of biomolecules, such as lipids or proteins, the study and determination of the secondary structure of proteins, quality control, and discrimination between physiological and pathological patient conditions. The quantification of proteins is usually achieved using the intensity or the area under the curve (AUC) of the amide I peak and interpolating the data with a calibration curve. The secondary structure of proteins is determined by the deconvolution of the amide peak region, which highlights the contribution of the different components (that is, α-helices and β-sheets) of the band.[10] Thus, changes in the amide I area can be associated with the denaturation of proteins and the loss of their functionality. Lastly, the fingerprint region (700–1300 cm^{-1}) and functional group (1300–1800 cm^{-1} and 2700–3500 cm^{-1}) areas can reveal differences in biofluids or cell compositions, allowing discrimination between physiological and pathological status through multivariate analysis of the entire measured IR spectrum.[11–14] This type of IR spectroscopy application has garnered increasing interest in recent years. Several studies have noted the feasibility of using IR spectroscopy and its derived techniques as diagnostic tools (Table 1). The results of these studies highlight the advantages of IR spectroscopy compared to UV-Vis spectroscopy and molecular biology techniques. In other words, IR spectroscopy is a label-free, rapid, and user-independent technique that requires only a small amount of the sample (that is, a few μls) and a few minutes to detect the IR spectrum of the sample. The results reported in Table 1 indicate that several research groups have developed reagent-free protocols to determine qualitative and quantitative clinical parameters in different bodily fluids by combining IR data with multivariate analysis. However, UV-Vis spectroscopic measurements require either a direct measurement of a specific chromophore, an indirect measurement of a dye used as a fluorescent label, or a reaction catalysed by enzymes, whereas molecular biology techniques often require the use of antigen–antibody interactions. In each of these cases, the use of specific additional reagents is required, which makes UV-Vis spectroscopic and molecular biology techniques expensive, not only due to the reagents themselves, but also for the time-consuming handling procedures, specific storage conditions, inventory control, and operator salaries. Besides the advantages of applying IR spectroscopy in diagnostics, there are several critical points to consider. First, quantification via IR spectroscopy requires calibration of the spectrometer. Calibration should be performed with a high quality standard and reference methods

and should cover a range of concentrations near the expected concentration range of the analyte in clinical samples. The calibration process for IR spectroscopy is labour-intensive; however, once completed, it is valid indefinitely because the IR signal does not change over time.[15,16] Second, water has high absorbance in the IR region of 4000–500 cm^{-1}, which interferes with the analysis. Water interference can be suppressed by drying the sample, subtracting the water spectra, or a combination of the two.[17] Lastly, the complexity and heterogeneity of biological samples may lead to erroneous results in multivariate analysis. Thus, the use of chemometric algorithms may be necessary to remove the interference of the matrix in which the analyte is included.[15]

Table 1 Summary of IR spectroscopy and its derived techniques proposed as diagnostic tools for clinical applications.

Sample	Technique	Analyte	Outcomes	Ref
Blood	ATR-FTIR	Albumin, glucose, total cholesterol, total protein, triglycerides, urea	PLS model predicts the concentration of the analytes	18
Plasma	ATR-FTIR and transmission	Albumin, Apolipoproteins, cholesterol, immunoglobulin, lactate, urea, total protein	PLS model predicts the concentration of the analytes	16,18,19
Serum		Albumin, creatinine, glucose, HDL, LDL total protein, cholesterol	Concentration of the analytes measured using IR is comparable to the concentration measured using accepted reference clinical chemical methods	15,20–22
Urea	ATR-FTIR	Creatinine, inorganic phosphate, total protein, urea, uric acid	Protein concentrations are often too low to be detected	18
Amniotic fluid	Transmission	Albumin, lecithin, sphingomyelin, surfactant	Assessment of foetal lung maturity	23,24
Saliva	ATR-FTIR	α-amylase, cortisol, phosphate, IgA, total protein, urea, EVs	Train induced stress determination in professional athletes	25
EVs	ATR-FTIR and transmission	Discrimination between EV subpopulations and between EVs generated by different cell lines	PCA in the fingerprint region	26

2.2 RAMAN SPECTROSCOPY

Adolf Smekai first theorised the inelastic scattering of light in 1923. The phenomenon was detected in practice by C.V. Raman (Nobel prize in Physics 1930) with Krishnan in 1928 using organic liquid measurements and simultaneously by G. A. Landsberg and L. Mandelstam in inorganic crystals.

Raman scattering is a two-photon phenomenon based on the inelastic scattering of electromagnetic radiation, which contains information about the molecular composition of a sample. It has been applied to solid, liquid, and gas samples and is a non-destructive technique that can be applied directly to samples without any extra sample handling, manipulation, or labelling. The principle of Raman scattering experiments is based on the interaction between monochromatic electromagnetic radiation and the electrons of the sample. This interaction induces a dipole moment within the molecule based on its polarisability.

When light interacts with matter, it can transfer part of its energy to the molecules causing distortion and polarisation of electrons. Consequently, the excited electrons reach a high-energy arrangement at a virtual state with a short half-life, which then rapidly relax back from their virtual state to the ground state. During this relaxation, a photon is emitted in different directions. The incident radiation can generate either elastic or inelastic scattering.

From these, elastic scattering, also known as Rayleigh scattering, is the most intense. In elastic scattering, there is no appreciable change in the energy between the incident and emitted photon, and the electron returns after excitation to the same vibrational level of the ground state. Rayleigh scattering occurs when distortion affects only the electrons, and no nuclear motion is induced. In Raman spectroscopy, Rayleigh scattering is usually filtered out. However, this phenomenon is utilised in other techniques, such as dynamic light scattering (DLS), a technique that is used to, for example, determine the size distribution profile of nanoparticle suspension.

In contrast, inelastic scattering occurs when the deformation of electrons induces motion in the nuclei of the atom. This motion transfers energy from either the molecule to the scattered photon or the incident photon to the molecule. In both cases, the emitted photon will have a different energy than the incident photon. This phenomenon is referred to as anti-Stokes scattering, that is, the scattered radiation has a higher energy than the incident radiation, whereas in Raman–Stokes scattering, the scattered radiation has a lower energy than the incident radiation (Figure 2). Usually, Stokes scattering is preferred in Raman spectroscopy because it has a higher probability of occurring than anti-Stokes scattering owing to the low energy state of most molecules at room temperature. Interestingly, the temperature can be measured by determining the differences between the intensities of Stokes and anti-Stokes scattering.[27]

Raman spectroscopy measures the wavelength shift between the incident light and the scattered photons. This shift is used to resolve the chemical composition of samples. Different functional groups scatter photons at different wavelengths. Similar to IR spectroscopy, the frequency of the scattered radiation depends on the mass of the atoms and the bond strengths involved (see eq. 1 and 2), whereas the intensity, or

the amount of scattered photons, depends on the polarisability of the electrons in the molecule, as described by eq. 4.

$$I = Kla^2\omega^{-4}, \quad (4)$$

where I is the intensity, K is the speed of light constant, l is the laser power, a is the polarisability of the electrons, and ω is the frequency of the incident radiation.[28,29]

Raman and IR spectroscopy are considered complementary techniques. Both directly measure the atomic vibrations in a molecule; however, IR active vibrations depend on changes in the dipole moment in a molecule during the vibration, whereas Raman active vibrations depend on changes to the polarisability of the molecule and thus to the distortions of the electron cloud around the atomic nuclei. Consequently, polar bonds usually display strong IR absorption, while apolar bonds exhibit a strong Raman signal. As an example, Figure 4 displays the IR and Raman spectra of the same EV suspension. The Raman peaks for the CH_2/CH_3 stretching area (2800–3000 cm^{-1}) have higher intensities than the amide I peak (1650 cm^{-1}, C=O). The IR spectrum exhibits the opposite behaviour, that is, the IR peaks for apolar groups have lower intensities, whereas the IR peaks for the polar groups have higher intensities.

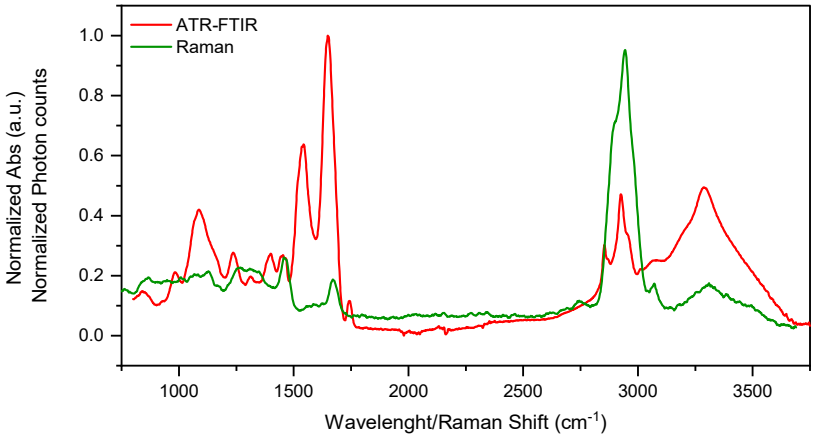

Figure 4 IR and Raman spectra of PNT2 derived EVs purified by differential centrifugation.

In Raman spectroscopy, the operator can control two parameters, that is, the laser power and the frequency of the incident light, whereas only the length of the light path (l in eq. 3) can be controlled in IR spectroscopy. This difference between Raman and IR spectroscopy gives Raman spectroscopy its peculiar ductility. In other words, increasing the laser power (I) directly affects the intensity of the Raman signal. However, the use of a powerful laser can cause photodegradation or heat damage to the samples, which affects their chemical composition. The frequency of the laser (ω)

can also be adjusted to improve the sensitivity of the Raman signal because the laser intensity depends on the fourth power of the frequency (eq. 4.). Increasing the frequency, for example, using a UV laser, appears to be an obvious method of improving the intensity. If fluorescence occurs, it has a lower energy than the UV light used. However, this approach to improve the Raman signal has a drawback: UV light has a high frequency with high energy, which is absorbed by many molecules. Therefore, increasing the laser power or frequency of the used excitation light increases the risks of photodegradation and oxidation of the samples. Near IR (NIR) or IR lasers are also widely used in Raman spectroscopy because only a few samples have a fluorescence signal at these wavelengths. However, the use of lasers with longer wavelengths for excitation might lead to a low intensity (eq. 4). Thus, high power NIR lasers are required, and the heating and degradation of the samples should therefore be controlled.

Both Stokes and anti-Stokes scattering are rare events. For example, Raman–Stokes scattering occurs with a probability from 1×10^{-6} to 1×10^{-8}. However, the low density of scattered photons is often not a problem. The density of photons delivered to the samples can easily be increased using a combination of a high-power laser and microscope. However, this approach can trigger other phenomena, such as sample degradation and an increase in the fluorescence background. Different solutions are proposed to overcome the fluorescence interference and increase the capability of Raman spectroscopy. These topics are summarised in Figure 5 and Table 2 and will be further discussed in the following chapters.

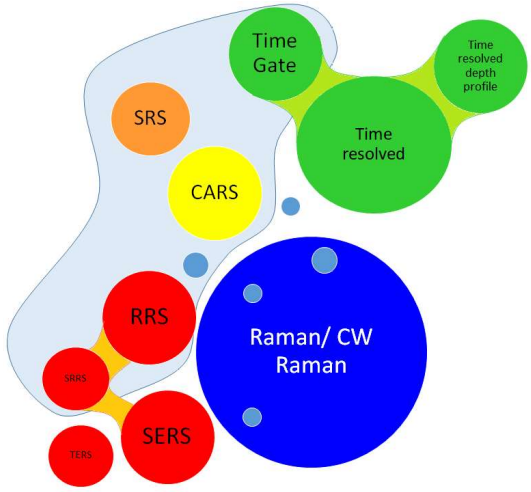

Figure 5 Conceptual map of the different Raman spectroscopy techniques. CW = continuous wavelength, SERS = surface enhanced Raman spectroscopy, TERS = tip-enhanced Raman spectroscopy, RRS = resonance Raman spectroscopy, CARS = Coherent anti-Stokes Raman spectroscopy, SRS = stimulated Raman spectroscopy

Table 2 Summary of Raman spectroscopy techniques, their advantages, and disadvantages.

Technique	Unique advantages	Limitations
Spontaneous Raman spectroscopy	Conceptually/instrumentally simple Highly reproducible Mature technology Many commercially available systems/manufacturers	Low number of photons and low probability Susceptible to fluorescence interference
Surface enhance Raman spectroscopy (SERS) Tip-enhanced Raman spectroscopy	Used in combination with simple and lower specification Raman spectrometers. High sensitivity, theoretically down to a single molecule	Poor reproducibility Expensive substrate costs Complicated analyte–substrate dynamics for biogenic materials
Time-gated Raman spectroscopy	Fluorescence suppression Commercially available systems	Pulsed laser is more likely to damage the sample
Coherent anti-Stokes Raman spectroscopy (CARS)	Fluorescence suppression Rapid	Shift in Raman peaks Measures only a small area of the spectra Non-linear concentration dependence Non-resonant background
Simulated Raman spectroscopy	Rapid No non-resonant background present Linear concentration dependence Spectra match spontaneous Raman spectrum	Measures only a small area of the spectra
Resonance Raman spectroscopy	Strong Raman signal	Occurs only at specific vibrations

2.2.1 CONTINUOUS-WAVELENGTH AND TIME-GATED RAMAN SPECTROSCOPY

Traditionally, Raman spectroscopy is referred to as continuous-wavelength (CW) Raman spectroscopy, where a UV, Vis, or IR CW laser is used to illuminate the sample. CW lasers emit constant light with a specific intensity and wavelength. As previously mentioned, the main problem of Raman spectroscopy is the fluorescence signal, which can overwhelm the Raman signal (Figure 6A). Fluorescence appears as a redshifted broad band, indicating that fluorescent radiation has a lower energy and frequency than the incident radiation. Thus, fluorescence is observed only in the Stokes part of the spectra. Different methods of suppressing fluorescence in spontaneous Raman scattering have been proposed and discussed.[30] These methods can be briefly summarised in five main categories:

1. Time domain methods, which make use of the different lifetimes of fluorescence (ns) and Raman scattering (ps) responses.
2. Frequency domain methods, which translate the difference in the lifetime of fluorescence and Raman scattering into a larger phase delay. This requires a high-frequency excitation laser.
3. Wavelength domain methods, which are based on Raman peak shifts according to the excitation wavelength of the used laser. The fluorescence band is not affected by these changes.
4. Computational methods, which are algorithm-based baseline correction methods.
5. Other methods; for example, photobleaching.

This thesis focusses on the time domain methods because the in-house-developed Raman spectrometer can detect a time-resolved fluorescence signal. The suppression of the fluorescence background in Raman scattering is achieved by combining a pulsed laser with a time-resolved complementary metal-oxide-semiconductor (CMOS) single-photon avalanche diode (SPAD) line sensor.

The principle behind the time-gated Raman spectrometer is shown in Figure 6B, which highlights the temporal profile of the incident laser pulse and the emitted Raman and fluorescence signals. Raman scattering and fluorescence have different response timescales: Raman scattering is a rapid event that occurs almost instantly less than several picoseconds after excitation, whereas fluorescence occurs in hundreds of picoseconds to a few nano- to microseconds. The difference in time between these two phenomena can be utilised to suppress and discriminate fluorescence radiation from Raman scattering using a short-pulsed laser and time-gated detector instead of the conventional CW laser and continuous-time detector.[31]

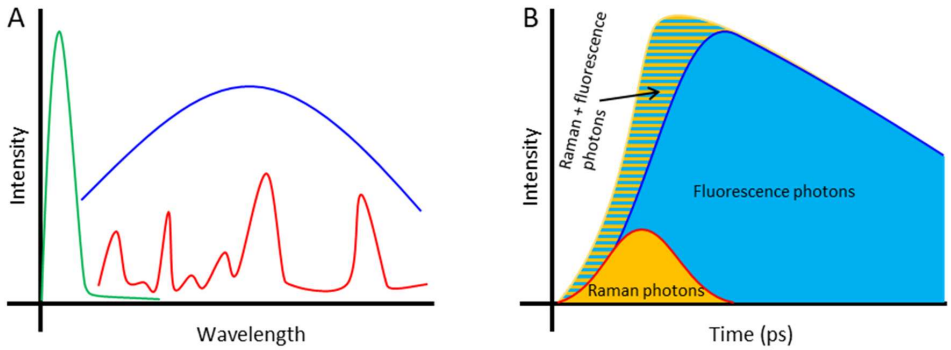

Figure 6 A) Wavelength distribution Raman scattered photons (Red) and fluorescence emitted photons (Blue) after excitation with a laser pulse. B) Time distribution of Raman scattering and fluorescence emitted photons.

In this study, we used the SPAD sensor fabricated with standard CMOS technology and a pulsed laser.[32–34] SPAD can detect the signal generated by a single photon. Thus, this type of sensor is efficient in detecting the few Raman scattered photos. CMOS SPAD sensors can also record the time of arrival (ToA) of photons. This information, along with the wavelength shift between the incident light and the scattered photons, allows for the simultaneous measurement of the spectral and temporal distributions of the Raman scattered photons. Hence, spectral distribution data are used to obtain the Raman spectra, whereas the temporal distribution is used to obtain the fluorescence lifetime.

2.2.2 COHERENT ANTI-STOKES RAMAN AND STIMULATED RAMAN SPECTROSCOPY

Coherent anti-Stokes Raman spectroscopy (CARS) and stimulated Raman scattering (SRS) spectroscopy are evolutions of spontaneous Raman spectroscopy intended to compensate for the weakness of the spontaneous Raman process. Hence, these techniques enhance the Raman signal in real-time, making them suitable for imaging living cells and organisms. Both techniques only generate the signal at the small focal point; therefore, they are inherently confocal and allow 3D sectioning.

CARS is a third-order non-linear method based on the stimulated Raman effect, which was first described by the Ford Motor Company in 1965. CARS microscopy was further developed by Duncan et al. and Zumbusch et al. almost 20 years later. CARS is a four-wave mixing process,[35] which involves four photons, three of which are generated by the laser beams and are known as 1) the pump (ω_p), 2) Stokes (ω_S), and 3) the probe (ω_{pr}). ω_p and ω_{pr} typically originate from the same source and have the same wavelength, whereas ω_S has a different source and wavelength. ω_S or ω_p and ω_{pr} can be tuned in a manner where the energy difference between ω_S and ω_p corresponds to the molecular vibration frequency of interest. The ω_S, ω_p, and ω_{pr} photons spatially and temporarily overlap at a small focus point in the sample, causing

coherent excitation, which leads to the release of the fourth photon (ω_{aS}). This final photon is the one detected by the sensor. ω_{aS} is the anti-Stokes, blue-shifted wavelength, and its energy is described by eq. 5.

(5) $$\omega_{aS} = \omega_p - \omega_S + \omega_{pr}.$$

Currently, there are two different approaches to CARS: single frequency and broadband CARS. Single frequency CARS is suitable for imaging owing to the rapid acquisition of a single vibrational resonance improved signal-to-noise ratio. However, this technique lacks spectral information; thus, it is not suitable for revealing the chemical composition of the sample. In contrast, the broadband CARS approach allows for the acquisition of a broad range of vibrational resonances simultaneously. Broadband CARS is slower when compared to single-frequency CARS. Nevertheless, its application in imaging allows for the measurement of the entire spectrum at each pixel and facilitates quantitative analysis. To perform a quantitative analysis using CARS, it is critical to consider the parameters that affect the intensity of the CARS signal (I_{aS}), which can be divided into two parts with the resonant and non-resonant terms (eq. 6).

(6) $$I_{aS} \propto |\chi^{(3)}|^2 = |\chi_R^{(3)} + \chi_{NR}^{(3)}|^2.$$

The resonant term ($\chi_R^{(3)}$) contains quantitative and qualitative information about the chemical nature of the samples,[36] while the non-resonant term ($\chi_{NR}^{(3)}$) depends on the electronic proprieties of the material and is independent of the frequency used for excitation. The resonant term ($\chi_R^{(3)}$) can be compared to the Raman spectra and is linearly proportional to concentration (eqs. 7 and 8). As summarised by Day et al., $\chi_R^{(3)}$ can be extrapolated from eq. 6 by obtaining the phase of the CARS field (Θ), as shown in eq. 9.

(7) $$I_{Raman} \propto \frac{NA\Gamma}{(\Omega-\omega_0)^2+\Gamma^2},$$

(8) $$Im[\chi_R^{(3)}] \propto \frac{NA\Gamma}{((\Omega-(\omega_p-\omega_0))^2+\Gamma^2},$$

(9) $$Im[\chi_R^{(3)}] = |\chi^{(3)}| sin\Theta \propto \sqrt{I_{aS}}\, sin\Theta.$$

Similar to CARS, SRS is a coherent Raman technique. SRS was first described by Woodbury in 1962, and its theory was further revealed by Hellwarth.[37] An SRS signal is generated when the energy difference of the two co-align beams, pump, and Stokes beams match the molecular vibration, resulting in excitation of the Raman active molecular vibration. The enactment of the signal is due to two complementary phenomena: stimulated Raman loss (SRL) and stimulated Raman gain (SRG). SRL is the loss of intensity in the pump beam, the energy of which is subsequently gained by

the Stokes beam, resulting in a strong Raman signal. SRS signals are superior to spontaneous Raman signals but less intense than those of CARS. SRS has several remarkable advantage over CARS. First, SRS is not affected by non-resonant background; thus, the SRS signal matches the spontaneous Raman spectrum and is linearly dependent on the concentration. The absence of non-resonant background also facilitates imaging. As previously mentioned, CARS measures the difference in energy between the pump and the Stokes photons emitted in the anti-Stokes region, a process in which there is no energy transfer to the sample. In SRS, the frequency differences between the beams must match for molecular vibration to occur. Consequently, the SRS process cannot occur when the frequency difference does not match the molecular vibration, whereas CARS can occur when there are no resonant molecules.

2.2.3 BIOPHARMACEUTICAL APPLICATIONS OF RAMAN SPECTROSCOPY

Raman and IR spectroscopy has applications in biopharmaceutical and clinical research as well as in the biopharmaceutical industry. Owing to its relatively simple instrumentation and the variety of commercialised models, spontaneous Raman scattering-based spectrometers are most commonly used in biopharmaceutical production. Similar to IR spectroscopy, Raman spectroscopy has its own monograph in EP10. However, Raman spectroscopy in EP10 is far less cited than the monographs for IR spectroscopy, that is, only 76 times. EP10 highlights Raman spectroscopy as a tool for chemical, physical, and process analysis. It can identify and quantify substances, their solid forms, and crystallinity and can monitor biological and chemical processes, such as synthesis, crystallisation, granulation, mixing, drying, lyophilisation, extrusion, encapsulation, and coating. In the biopharmaceutical field, regulatory agencies such as the European Medicines Agency (EMA) and the Food and Drug Administration (FDA) demand a thorough understanding and control of the biological processes involved in drug production. This has led to the adoption of efficient process management systems such as Quality by Design (QbD) and PAT.[38–40] Both of these processes require new analytical technologies suitable for rapid, non-contact, non-destructive, highly sensitive, and multiparametric analysis to assess the molecular composition and variance of often complex mixtures. Among these new technologies, Raman spectroscopy has been applied successfully in different key steps of biopharmaceutical production. For example, the control of raw material and cell culture media, the analysis and monitoring of the bioprocess, and the analysis of the final biopharmaceutical products and their stability.[5] In the biopharmaceutical process, cell culture media and their complex biological derivatives, are used to provide nutrients to cells and provide stable and suitable conditions for their growth and metabolism. The complexity and batch-to-batch variation of such media require extensive testing, which is often carried out using expensive and destructive methods based on separation techniques. Raman spectroscopy can provide information on media composition and the variance between the measured spectra of different batches, which can be correlated to the critical process parameters or quality attributes.

In particular, Raman spectroscopy combined with chemometric data analysis can characterise and assess the lot-to-lot and batch-to-batch variances in complex cell-media components.[41] Unfortunately, owing to the complexity of cell media and differences in the concentrations of its components, it is practically impossible to quantify or identify specific analytes in cell culture media. Thus, in such cases, chromatographic or mass spectrometry (MS)-based techniques are still irreplaceable. Raman spectroscopy is, however, suitable for both off- and on-line process analysis measurements. Off-line measurements of bioreactor broth were first proposed in 1997, and it was already possible at that time to monitor the concentrations of glucose, glutamine, and lactic acid.[42] More recently, Raman spectroscopy was used as an inline technique to monitor the lab-scale production of phenylalanine by a strain of *E. coli*.[43] The reliability of Raman spectroscopy as a tool for industrial-scale bioprocessing was subsequently suggested by Abu-Absi and colleagues who monitored the concentrations of lactate, ammonia, glucose, glutamate, and glutamine via multiple Raman immersion probes.[44] The same research group was also able to correlate the data measured by Raman spectroscopy with the total cell density. The metabolite concentrations and cell growth measured by Raman spectroscopy presented a good correlation with the off-line measurements.[44] In view of this and other results, it can safely be concluded that Raman spectroscopy is a well-established technique that can be used to monitor bioprocesses. It is worth noting that given a rapid and reliable in-line monitoring method coupled with a closed-loop feedback control system, the concentrations of specific metabolites can be maintained within pre-established concentrations.[45,46] Raman spectroscopy has also proved to be suitable for monitoring the freeze-drying cycle.[47] Freeze-drying is not a bioprocess; however, most biopharmaceutical products have a lyophilisation step in their manufacturing process. In particular, a Raman spectrometer combined with NIR might be profitably applied as PAT tools in the freeze-drying process. This is because the Raman signal can follow ice nucleation and the primary drying process owing to a peculiar ice peak at 215 cm^{-1},[47] thus revealing information on the physical state of the product. The application of Raman spectroscopy in the freeze drying of biomaterials has been discussed in further detail in a review paper by Merivaara et al. [48]

However, there are several critical points to be considered when a Raman spectrometer is applied in biopharmaceutical production processes. Raman scattering is a weak phenomenon, particularly in spontaneous Raman scattering spectroscopy, and the use of, for example, a UV laser or surface-enhanced Raman scattering (SERS) has been suggested as solutions to improve the signal-to-noise ratio. However, both of these methods have critical drawbacks. SERS is non-reproducible and has more affinity to certain types of molecules. UV is high-energy radiation, and thus may result in photodegradation of the studied sample. Another significant complication is the susceptibility of many biopharmaceutical analytes to fluorescence inference because these samples often have low concentrations in aqueous solutions, which may contain multiple fluorophores. Moreover, the complex and heterogeneous compositions of typical biological samples result in complex Raman spectra with low signal-to-noise ratios. Therefore, interpretation of the results may require complex data processing. Improvements in the performance of the spectrometers, development of new

approaches, such as time-gated Raman spectrometers and coherent Raman scattering techniques, and further commercialisation of these spectrometers can help overcome these critical points. Raman spectrometers are significantly more expensive than FTIR, NIR, UV-Vis, and fluorescence spectrometers, which may be one of the reasons why Raman spectrometers are too expensive for use in undergraduate teaching laboratories. Therefore, students cannot obtain any practical experience of Raman spectroscopy, and it remains an obscure technique that should be avoided.

2.2.4 PRECLINICAL APPLICATION OF RAMAN SPECTROSCOPY

The applications of Raman spectroscopy techniques in biopharmaceutical or preclinical research areas are extensive. The variety of these applications depends on the wide range of Raman spectrometers available in the market. These applications can focus on the discrimination of healthy samples or tissue from pathological ones or cell and tissue structure studies. Excellent review articles have been written on all these topics.[49–51] Thus, in this section, a basic overview of the applications of Raman spectroscopy is given, with a focus on its advantages and drawbacks.

Raman spectroscopy is label-free and non-destructive, and its fingerprinting capability makes it a promising tool for diagnostics and other investigative procedures. Numerous studies have highlighted the capability of various types of Raman spectroscopies in discriminating between pathological and non-pathological tissues, cells, and liquid biopsies. As an example, Corsetti et al. differentiated between late-stage androgen-resistant prostatic cancers and non-androgen-resistant cell lines by analysing three wavenumber regions of Raman spectra: 330–1350 cm^{-1}, 1400–1800 cm^{-1}, and 2800–3100 cm^{-1}. The authors used a spontaneous Raman spectrometer and analysed the data using PCA and Linear Discriminant Analysis (LDA), which underline the differences between phenylalanine, tyrosine, DNA, amide III, and L-arginine content.[52] Other studies on prostatic cancer biopsies successfully distinguished between benign and malignant prostate tissues[53] and aggressive and non-aggressive prostatectomy cancer tissues.[54] This study was conducted with a Raman confocal micro-spectrometer. Subsequently, CARS has been used to identify a glioma within the healthy brain tissue of a fresh unfixed *ex vivo* mouse brain.[55] This study suggests that CARS microscopy has the potential to be applied as an *in vivo* imaging technique owing to its high sensitivity for chemically selective 3D imaging without exogenous labelling agents. Additionally, non-invasive biopsy screening can also be performed by Raman spectroscopy. Li et al. used the SERS spectra of serums from healthy people and cancer patients to classify the samples as cancerous or healthy using a supervised machine learning model.[56] Independent of the disease and type of biopsy, the workflow in clinical diagnosis is based on vibrational spectroscopy data. This can be summarised in five main steps, as presented in Figure 7: i) sample collection and preparation, ii) spectra acquisition, iii) data processing, iv) model validation, and v) diagnosis. Each of these steps has its own peculiar critical points and directly affects the subsequent stage and outcome.

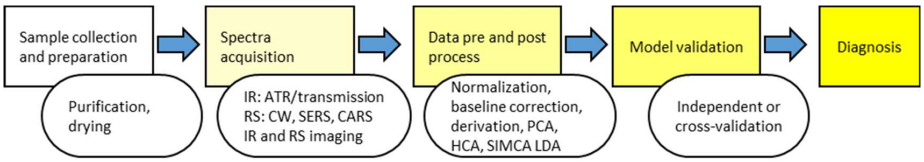

Figure 7 Diagram describing the steps required to develop a diagnosis method based on spectroscopy techniques.

Ideally, sample collection and preparation should be rapid and simple. Laborious and expensive purification methods might discourage clinical laboratories from investing in such techniques. The spectra acquisition process is directly affected by the features and quality of the spectrometer used. Spontaneous Raman spectrometers are widely available in the market; however, the fluorescence interference and intrinsic weakness of the spontaneous Raman signal might make the analysis difficult. Time-gated CARS and SRS spectrometers can help overcome these problems. However, there are currently (March 2022) no CARS and SRS spectrometers available in the market and the ones used in the cited publications are all home-built instruments. Time-gated spectrometers, however, are already commercially available. Sample preparation and the standardisation of spectrum measurement protocols are critical for the successful development of a diagnostic workflow. The development of protocols for sample preparation to measure spectra for clinical purposes should be guided by established methods in clinics, and with these spectra measurements, the robustness and reproducibility of these methods should be validated. Once the spectra are measured, raw data must be processed to obtain information on the samples. Data processing is usually divided into pre-processing and chemometric data analysis. The spectra of biological samples are often complex and difficult to interpret; thus, data treatment is necessary. First, all spectra should undergo quality control to exclude eventual artefacts or spectra with low signal-to-noise ratios. Second, further steps such as baseline correction, derivatisation, smoothing, and normalisation are performed. The following crucial factor is the choice of an appropriate statistical method for qualitative or quantitative analysis. These methods can be briefly classified as supervised and unsupervised methods. Supervised methods use a category membership of samples to define classes and are recommended for the identification of samples, whereas unsupervised methods are used to sort spectra and obtain information on the complexity, heterogeneity, and similarity of the dataset. Data processing protocols might be complex and require a broadly interdisciplinary approach. It has become clear that shared established protocols are required to gain consensus on, and appropriate reproducibility of, data treatment.[57–59] Once the protocols are established, the results of Raman studies must be compared with state-of-the-art diagnostic tools; as an example, Li et al. conducted their study on a group of 93 histology-confirmed prostate cancer patients and 68 healthy voluntaries.[56] To date, there are no Raman-based diagnosis protocols accepted by the EMA or FDA. However, national and international research networks are working towards this.

Among these initiatives, it is worth mentioning the UK EPSRC Clinical Infrared and Raman Spectroscopy for Medical Diagnosis Network, the EU COST Raman4Clinics Action, and the International Society for Clinical Spectroscopy (http://www.clirspec.org). Raman spectroscopy is widely applied in fundamental and applied research. The ductility of Raman-based techniques allows for not only the identification of pure substances, but also suitability in more refined studies. For example, spontaneous Raman microscopy may localise the uptake of drugs at the cellular level, as suggested by El-Mashtoly et al. In this study, the authors note that the distribution and metabolism of erlotinib can be entirely studied using Raman spectroscopy.[60] The detection of the distribution of erlotinib within cells using Raman spectroscopy is possible owing to its peculiar chemical structure; erlotinib presents an alkyne bond, which generates a Raman signal at 2100 cm^{-1}. This signal falls into the silent wavenumber region of the Raman spectrum and is not present in the Raman spectra of cells. Thus, through accurate mapping, it is possible to highlight the distribution of the drug and its metabolites. Erlotinib presents four different metabolites according to an analysis of the Raman spectra of the highlighted spots, and thus it is possible to discriminate between them. Raman spectrum analysis suggests the presence of desmethyl-erlotinib, which has been confirmed using mass spectrometry methods in other studies.[61,62] The authors, however, note that the concentration of erlotinib used was significantly higher than the concentration that can be reached in an organism. A high concentration of the drug was necessary because of the weakness of spontaneous Raman phenomena. Other studies where either CARS or SRS were used suggest that these techniques are suitable to study the distribution and metabolism of drugs and nanoparticles as well as their internal cellular trafficking. Raman spectroscopy is widely used in research; thus, most spectrometers are made with a broad range of settings, which enables their use in many analytical applications. Instruments with such designs may not be suitable for a clinical environment. Therefore, the development of Raman spectrometers designed to robustly repeat analyses might help Raman spectroscopy become accepted as a diagnostic tool.

2.3 FLUORESCENCE AND FLUORESCENCE LIFETIME

Fluorescence, along with phosphorescence, is part of luminescence phenomena. Luminescence is the emission of light, which occurs from electronically excited states. Phosphorescence is the emission of light from a triplet excited state, where the spins of the excited electron and ground state electron have the same orientation. In fluorescence, the emission of light is caused by the relaxation of the electron in the excited state (singlet state) that has the opposite spin of the electron in the ground state. Fluorescence emission rates are close to 10^9 s^{-1} and its lifetime (FLT) is close to 10 ns. FLT is the average time taken for the excitation of an electron and its return to the ground state. For Raman scattering, the Jablonski diagram (Figure 2) helps us understand the luminescence process. Following light absorption, the electrons of the fluorophore are excited to different vibrational levels of the electronically excited states S_1 or S_2 etc. This process takes place in the order of 10^{-15} s. Once the fluorophore

is excited, internal conversion occurs. This is a rapid non-radiative process that includes relaxation from S_2 or higher electronically excited states to the first vibrational state of S_1 within 10^{-12} s. Subsequently, the electron in the S_1 excited level can decay to different vibrational states of the electronic ground state S_0 by emitting a photon, that is, via fluorescence. This relaxation can also occur through a radiationless process, that is, internal conversion. In both cases, the energy released during relaxation is less than that of the incident light. Thus, in fluorescence, the emitted photons are 'Stokes shifted' compared to the incident light. During these processes, the electron spin is retained. Generally, the same fluorescence emission spectrum is observed, regardless of the excitation wavelength; the excess energy, which may lead to higher electronic and vibrational levels, are dissipated by internal conversion, leaving the electron in the lowest vibrational level of S_1. Thus, the fluorescence emission spectrum is usually due to the S_1–S_0 decay. The absorption and emission spectra mirror each other because the same transitions are involved in both phenomena, and the vibrational energy levels of S_0 and S_1 are not significantly altered by the different electronic distributions of these energy levels.

The emission and absorption spectra are not the only characteristics of fluorophores. The FLT and quantum yields are other important parameters used in fluorescence spectroscopy. Quantum yield is the relative number of emitted photons compared to the number of absorbed photons. Molecules with a quantum yield of 1 have the highest emission, and no radiationless transfer occurs. FLT is the average time the electron stays in the electronically excited state before returning to the ground state. During that time, the fluorophore loses some of its energy as heat via vibrational relaxation. FLT (τ) is defined as the time it takes for the fluorescence intensity to decrease to 1/e from its original value and is described by eq. 10.

$$\tau = \frac{1}{k_f + k_{nr}}, \tag{10}$$

where k_f is the rate constant of fluorescence, and k_{nr} is the sum of the rate constants of non-radiative processes.

In a dilute solution of fluorophore, the fluorescence decay follows a first-order decay, whereas if several fluorophores with different individual decays are present, the FLT is defined as a weighted arithmetic mean of all the lifetime components. FLT is a long process compared to the timescale of other light–matter interactions: For organic molecules, the lifetime of the singlet state ranges from tens of pico-seconds to hundreds of nanoseconds. However, the phosphorescence lifetimes are longer spanning from seconds to minutes. During the fluorescence decay, a variety of events can occur in the fluorophore, such as electron redistribution, geometric alteration, reorganisation of the surrounding molecules, and chemical transformation. These events, collectively referred to as quenching, result in a loss of energy in non-radiative events, which shortens the FLT. Quenching events are categorised based on the manner in which energy is dissipated; thus, the quenching processes are divided into internal and external quenching.

Internal rotation, electron distribution in excited states, and the internal heavy atom effect affect molecular vibrations and rotations; hence, they are also considered internal quenching mechanisms. In general, the presence of heavy atoms as substituents of aromatic molecules (that is, Br, I) results in fluorescence quenching because of the increased probability of intersystem crossing.

The internal rotation affects the FLT as described by eq. 11.

$$\tau = \frac{1}{k_f + \frac{k_B T}{4\pi r^3 \eta}}, \quad (11)$$

where k_B is the Boltzmann constant, T is the temperature, r is the radius in meters, and η is the solvent viscosity.

Viscosity also affects the FLT and can be described by the Förster–Hoffmann model (eq. 12).

$$\tau = C_m \eta^{\gamma}, \quad (12)$$

where C_m is the temperature and concentration constants, and γ is a dye-dependent parameter.

The FLT of fluorescence dyes, which have a high sensitivity to viscosity (molecular rotors), changes from picoseconds to nanoseconds in viscous media. It is evident that high-temperature and low-viscosity conditions decrease the FLT because these conditions promote barrierless rotation in the excited state. However, system rigidification of the fluorophore-environment due to, for example, a decrease in temperature, high viscosity media, or other restrictions in rotation, that is, a rigid chemical fluorophore structure owing to the presence of a double-bond, increases the FLT.

Alternately, the FLT can be affected by reversible changes in electron distribution, which occur in the excited state. Compared to the previous case, the change in the electronic distribution is less susceptible to temperature and viscosity and is strongly dependent on the chemical structure. Excited-state changes to the electron distribution occur mostly in molecules capable of transferring such electrons. The understanding and manipulation of this process have inspired the development pH probes, which are actively used in FLT imaging.

External quenching mechanisms include Förster resonance energy transfer (FRET), Dexter electron transfer, and dynamic quenching. FRET is a process in which energy is transferred from one chromophore to another. FRET-based methods have been successfully used to determine the distance between interacting molecules (typically in the range 1–10 nm) by monitoring changes in emission intensity on the donor and acceptor chromophore via fluorescence spectroscopy. Subsequently, FRET also becomes a powerful tool in FLIM.

Dexter electron transfer operates at distances significantly shorter than those of FRET. FRET and electron transfer are different processes; in the former, excitation

energy is transferred between two chromophores via a coupled transition, and in the latter, an excited electron is transferred from a donor to an acceptor via a non-radiative path.

Lastly, excited fluorescent molecules can lose their energy via collisions in a non-radiative phenomenon known as dynamic quenching. Various events occur during the collision between an excited molecule and a quencher, which lead to energy transfer. Probes based on a dynamic quenching principle play an important role in lifetime imaging for the measurement of oxygen and other analytes.

The sensor for the time-resolved fluorescence Raman spectrometer used in this study can measure the FLT. Thus, this thesis focusses on its application in the pharmaceutical field.

Table 3 summarises the differences and similarities between Raman scattering, fluorescence, and fluorescence lifetime.

Table 3. Summary of the differences and similarities between Raman scattering, fluorescence, and fluorescence lifetime. *I* = intensity, *K* = constants of the speed of light, **I** = laser power, *a* = polarisability of the electrons, and ω = frequency of the incident radiation

Raman	**Fluorescence**	**Fluorescence lifetime**
Inelastic scattering	Spontaneous emission of radiation (luminescence) from an electronically excited molecular entity with retention of spin multiplicity.[63]	Parameter describing the time evolution of the decay of fluorescent radiant intensity.[63]
Stokes or anti-Stokes shifted	Stokes shifted	
Space domain	Space domain	Time domain
Polarisability	Use an electron-density axioma	
Weak for CW/TG Strong for CARS RSR	Strong	
$I = Kla^2\omega^4$	$I_F \propto [A^*] \propto I_{abs}$	$I_{(t)} = I_0 e^{-t/\tau}$
Chemical composition		
High structural sensitivity	Low structural sensitivity	
No sample preparation	Requires a fluorescence dye	
Depends on the chemical composition and physical state of the sample.	Depends on the fluorophore concentration.	Not dependent on fluorophore concentration, absorption by the sample, sample thickness, method of measurement, fluorescence intensity, photobleaching, or excitation intensity.
Partially affected by changes in pH and temperature.		Affected by external factors, such as temperature, polarity, and the presence of fluorescence quenchers.

2.3.1 FLUORESCE LIFETIME IN PHARMACEUTICAL APPLICATIONS

FLT is used to distinguish the molecular environment in which the fluorophore is located. In the pharmaceutical field, FLT is applied to multiple biomedical processes, including the monitoring of disease progression, drug efficacy, and cell metabolism.

FLT imaging of biological samples can identify cell structures by the different viscosities of the membrane. Numerous dyes have been suggested for this purpose, particularly the meso-substituted BODIPY dye with a rotatable phenyl group. Molecular rotors have been successfully used to study lipid rafts, which are connected to several pathological conditions, including Alzheimer's disease.[64,65] The FRET-FLIM approach has been used to study protein-to-protein and lipid-to-lipid interactions; however, this diverges from the purpose of this thesis. For detailed information, the reader is referred to exhaustive reviews that are available on the subject.[66–68]

2.4 EXTRACELLULAR VESICLES

EVs are bi-layer membrane nanoparticles released by numerous cell types into the extracellular environment. EVs are found in different biofluids, such as blood, urine, tears, and sweat. The physiological role of EVs is not yet fully understood. However, evidence suggests that EVs are involved in both long- and short-distance cell-to-cell communication within the same organism or the organism and its microbiota.[69] EVs are also a pathway utilised by cells to discard excess metabolites (for example, lactic acid). EVs have heterogeneous size distributions and compositions; they contain cytosol, nucleic acid, lipids, proteins, and even entire organelles of the originating cell.[70] Regarding the particle size distribution, EVs range from approximately 30 to 1000 nm in diameter depending on the technique used and the purification method.

EVs have only recently gained interest. However, the first evidence of these nanoparticles dates back to 1946, when Chargaff and West observed pro-coagulant platelet-derived particles in normal plasma. Two decades later, Wolf and his colleagues highlighted the presence of 'platelet dust' in platelet-derived particles in normal plasma. Subsequently, in the decade of 1970–1980, separate and independent studies suggested the presence of nanoparticles in biofluids, and the first detailed study on the EV structure was published. In the following years, an increasing number of studies on the composition, structure, and function of EVs were published. However, it was only in 2011 that the International Society of Extracellular Vesicles (ISEV: www.isev.org/) was founded. The ISEV aims to unify the nomenclature and methodologies of EVs. In 2014 and 2018, the ISEV released MISEV2014 and MISEV2018 (minimal information for studies of extracellular vesicles), respectively, as guidelines for EV-related studies. Owing to the heterogeneity of EVs due to the source, contaminants, EV subpopulations, and lack of consensus on both the purification and characterisation methods, the guidelines are still incomplete. In the last decade, IR and Raman spectroscopy have been applied in the EV field for the first time,[71,72] whereas the first use of time-gated Raman spectroscopy to study EVs[73] was only published in 2020 (Figure 8).

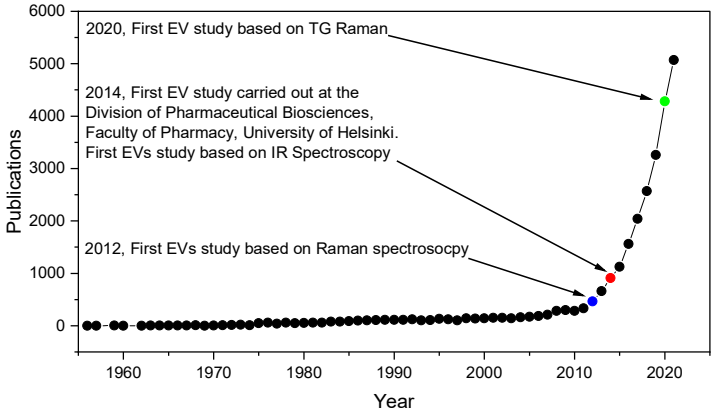

Figure 8 Number of publications based on a search of the literature databases PubMed and science direct with the word 'extracellular vesicles' and/or 'exosomes' and 'microvesicles' (1950–2021).

The classification of EV populations is challenging owing to their heterogeneity in size and composition, their origin, sedimentation speed, and biogenesis pathways. Classification based on their biogenesis pathway is probably the most conventional; it divides EVs into three different populations known as apoptotic bodies, microvesicles, and exosomes.[74] Different authors also suggest the existence of other exotic nanoparticles, such as supermeres and exomeres,[75,76] which can be included in the EV-ome. However, it is often difficult to discriminate between these EV populations because their sizes and compositions overlap; thus, an increasing number of authors categorise EV suspension based on the size of the EVs (that is, small, medium, and large EV)[26] or the purification method used.[77]

2.4.1 APOPTOTIC BODIES

Apoptotic bodies are generated from indiscriminate surface blebbing, which occurs during apoptosis, and are released into the extracellular environment. Their diameters vary from fifty to thousands of nanometers. Because of their origin, apoptotic bodies are not the focus of most studies and are often considered an impurity, which are removed by either centrifugation or filtration from the pool of EVs. Apoptotic bodies exhibit a high level of phosphatidylserine,[78] also known as an 'eat me signal', on the outer surface of the membrane that stimulates the endocytosis by macrophages and Kupffer cells.

2.4.2 MICROVESICLES

Microvesicles (MVs) have sizes ranging from 50 to 1000 nm.[79] MVs are released by outward budding of the plasma membrane, where the generated vesicle is released directly into the extracellular environment. The biogenesis of MVs is generally less defined than that of exosomes. MVs are generated and released into extracellular space by direct outward blebbing and pinching of the plasma membrane.[80,81] MV biogenesis is preceded by localised changes in the lipids and protein composition of the cell membrane, which modify its rigidity and curvature.

These changes are preceded by metabolite redistribution and selective enrichment of MV cargo at the blebbing site. A summary of MV biogenesis and uptake is shown in Figure 9, while a detailed discussion on the MV biogenesis can be found in the following reviews: Triacario et al. and Muralidharan-Chiari et al.[81,82]

2.4.3 EXOSOMES

Exosomes are generated from multi-vesicular bodies (MVBs), which are intracellular endosomal organelles, characterised by multiple intraluminal vesicles enclosed within a single outer membrane. Different mechanisms for the formation, organisation, loading, and release of MVBs have been proposed. These mechanisms can involve four endosomal sorting complexes required for transport (ESCRT) proteins, or they can be ESCRT-independent. ESCRT-independent pathways involve

protein complexes formed by syndecan, syntenin, Alix, and ceramides or tetraspanins, such as CD63 and CD9. However, the biogenesis mechanisms of exosomes seem to be complementary because the knockdown of ESCRT does not eliminate exosome production.[83]

Exosomes are among the smallest particles comprising EVs; their particle sizes range from 30 to 200 nm.

2.4.4 BIOCHEMICAL COMPOSITION OF EVS

EV structure and composition are summarised in Figure 9. EVs contain practically all principal cell components, such as lipids, proteins, nucleic acids, metabolites, and, in some cases, organelles. The relative amount of these components differs significantly between EV subpopulations and EVs produced from different cell types. The lipid composition resembles the cell membrane composition. However, EVs exhibit an enrichment of cholesterol, phosphatidylinositol, phosphatidylethanolamine, phosphatidylserine, and ceramide and a decrease in phosphatidylcholine. This peculiar lipid composition is due to EV geometry.[78] Thus, EVs are enriched in conical shaped lipids, where their head groups are larger than the hydrophobic tails and vice versa. This peculiar lipid composition consequently determines the structure and geometry of EVs, which consist of a lipid bilayer forming a spherical vesicle, a structure such as liposomes. Cholesterol molecules in the lipid bilayer are necessary to increase the rigidity of the membrane. The lipid composition is not homogenous; EVs presents lipid rafts, which are areas resembling small islands in the lipid bilayer membrane consisting of sphingolipids and membrane proteins. Sphingolipids are glycosylated lipids, and it is believed that they play an important role in cell–EV recognition.

EVs also carry cytoplasmic and transmembrane proteins. The first group of proteins include heat shock proteins, cytoskeletal proteins, enzymes, ESCRT components, signal transductors, ribosomal proteins, and histones. The second group includes adhesion proteins, such as tetraspanins and integrins, major histocompatibility complex (MHC) class I and II proteins, and lipid bonded proteins, such as annexins and flotillins. EVs are enriched in proteins that are related to their biogenesis pathways and cargo sorting. Overall, the protein compositions of EV subpopulations and EVs from different sources seem to differ more than the lipid compositions. Moreover, the protein compositions also seem to vary between the suspensions of EVs from the same source when they are purified with different purification methods. This can be explained by the different specificity of the purification methods towards a certain EV subpopulation and/or their ability to remove non-EV proteins.

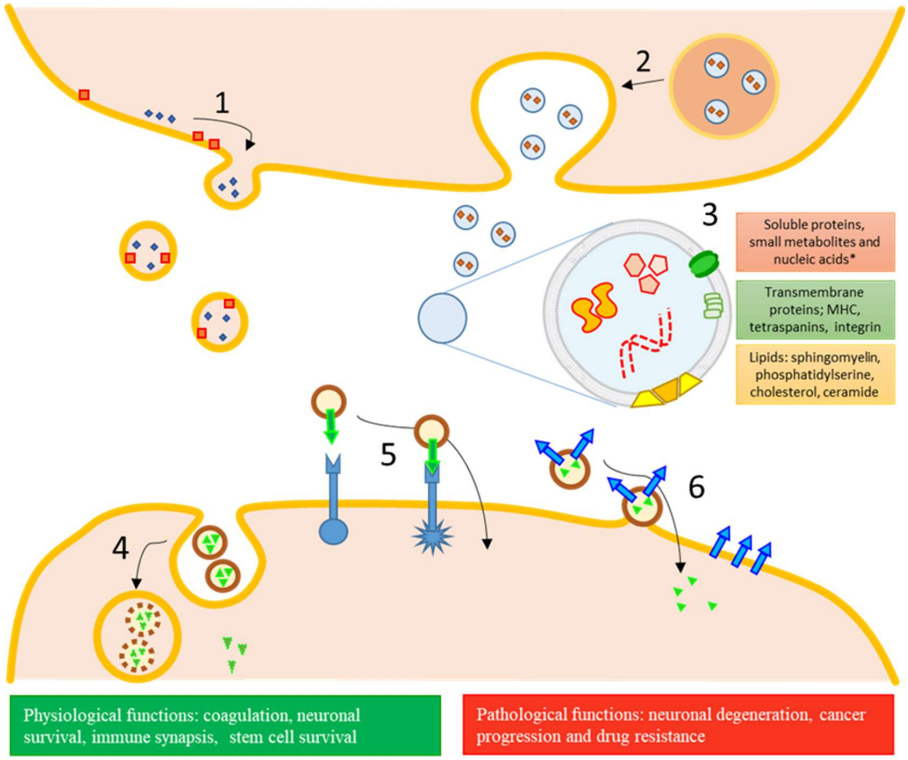

Figure 9 Schematic representation of EVs, structure biogenesis, and EV–cell interaction. 1. Biogenesis of MVs by direct budding from the plasma membrane. 2. Biogenesis of exosomes by fusion of internal multivesicular compartments to the plasmatic membrane. 3. EV structure (*nucleic acids are also present on the surface of the EVs). 4. Cell uptake of EVs mediated by endocytosis. 5. Interaction with membrane receptor. 6. Fusion with the cell membrane.[51]

Evidence suggest that EVs are able to carry nucleic acids, that is, DNA and different types of RNAs, including mRNA, miRNA, and rRNA. Typically, RNA polymers are contain approximately 200 nucleotides, with a smaller portion extending out to 4 kb[84]. It has been speculated that EVs can be physiologically or artificially loaded with oligonucleotides with a size of up to 30 kb, thus making them extremely efficient RNA carriers.[85] DNA is far less common than RNA in EVs, and DNA is mainly found in apoptotic bodies. Several findings indicate that EVs can transfer genetic material horizontally and modify the metabolism of the target cell. This, along with the possibility of loading EVs with selected cargo by modulating the donor cells to favour inclusion, load RNA in EVs *in vitro*, or utilise the potential targeting capability of EVs, has immense therapeutic potential.

The final group of major biomolecules are glycans and glycoproteins, which play a significant role in EV targeting. Various studies have suggested the profiling glycan present on EVs as a potential source of cancer biomarkers.[86] However, owing to the

intrinsic methodological limitation, complex structure, and heterogeneity in both EVs and carbohydrates, an in-depth analysis of the EV glycome remains challenging.

Despite the rapidly increasing number of EV-related publications, the lack of standardisation for characterisation and purification methods, as well as the heterogeneity of EV populations, makes it difficult to compare results from different studies.

2.4.5 EV PHYSIOLOGICAL AND PATHOLOGICAL FUNCTION

EVs can exert their functions in various ways, such as via ligand-cell surface receptor binding and membrane fusion. During membrane fusion, EVs can release their cargo inside the target cell or transfer receptors directly onto the target cell membrane. Moreover, cells can take up EVs via endocytosis, which may lead to the release of the EV content within the cells. In physiological conditions, EVs are involved in various functions, such as tissue repairing, wound healing, stem cell maintenance, blood coagulation, synaptic plasticity, and immune and inflammation modulation. Figure 9 summarises EV–cell interactions and lists several EV functions.

For example, B-lymphocytes spread antigens bound to MHC-II by utilising EVs. Vesicle-associated complexes are capable of activating MHC class II-restricted T-cell responses, suggesting a role for EVs in antigen presentation *in vivo*.[87] EVs derived from dendritic cells can transfer MHC-I and MHC-II proteins and other T-cell co-stimulatory molecules to other dendritic cells or CD4+ and CD8+ T-lymphocytes inducing their activation.[88] Evidence suggest that EVs take part in immune synapsis, where they shuttle miRNA from T-cells to antigen-presenting cells.[89]

Numerous findings suggest that EVs play an important role in different pathologies and their role varies enormously between different pathogenesis. An increasing number of studies note the role of EVs in the progression of neurodegenerative diseases, such as Alzheimer's disease (AD). In AD, EVs are able to carry misfolded beta-amyloids; thus, they seem to be involved in the progression of the neurodegenerative effects of misfolded protein.

Alongside their involvement in neurodegenerative diseases, EVs appear to have different roles in the regulation of tumour microenvironments and cancer progression. For instance, EVs released by aggressive types of tumour cells are prone to promoting a similar aggressive phenotype in other cancer cells. This includes drug resistance, increments of invasiveness, and proliferations. In addition, EVs released by metastatic cancer cells promote the formation of pre-metastatic niches, which facilitate the progression of new metastasis.[90–92]

Cancer cell-derived EVs have shown the ability to alternate the tumour microenvironment. For example, EVs released by Hodgins lymphoma are able to attract fibroblasts and promote the differentiation of these cells in cancer-associated fibroblasts.[93] Cancer cell-derived EVs are also capable of promoting angiogenesis by inducing endothelial cells to form new blood vessels. Additionally, cancer cell-derived EVs might be able to affect the metabolism of the immune system, that is by inducing the production of pro-inflammatory moieties, by influencing the differentiations of

monocytes or inhibiting T-cell proliferations.[94] The effect of cancer cell-derived EVs is summarised in Figure 10.

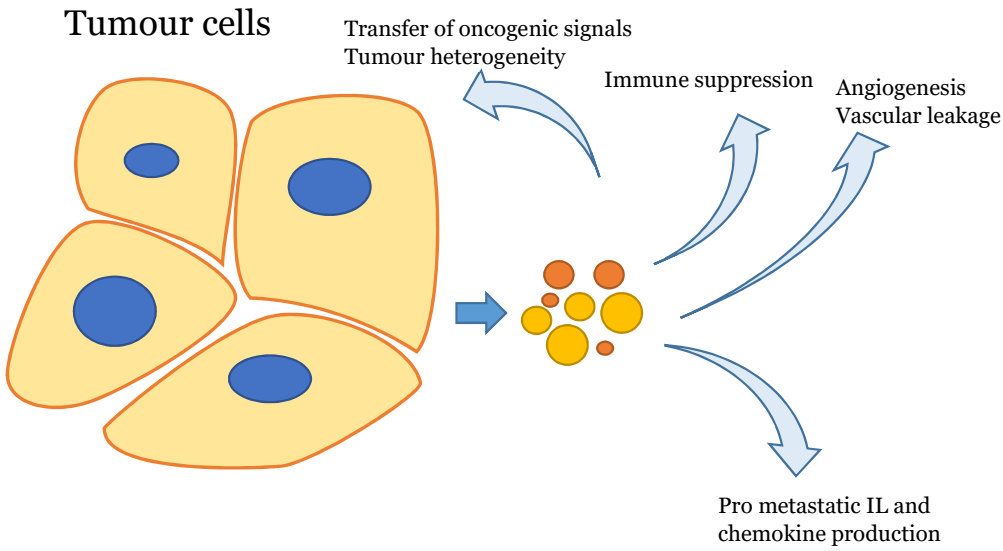

Figure 10 Schematic graphic showing cancer-derived EV metabolism.[95] IL= interleukins

2.5 PURIFICATION METHODS FOR EVS

Different purification methods and protocols have been proposed for EV purification.[96–102] The advantages and disadvantages of the most popular methods are summarised in Table 4. Among these methods, differential gradient (DG) and size exclusion chromatography (SEC) are considered the most efficient methods of removing impurities from EV suspensions.[101,103] However, both of these methods lead to a heavy loss in EVs. To date, there is no clear consensus as to which is the best purification method for EVs because a comprehensive study comparing different purification methods and protocols has not been conducted, and different protocols of the same method are still widely used. As a general rule, we can note that methods with a high recovery, that is, precipitation (PEG, salting out), and low molecular weight cut-off centrifugal filters, have a low specificity, whereas methods that are able to efficiently separate EVs from other impurities have a low recovery. Thus, it is logical to assume that the purification method of choice should depend on the intended use and downstream applications of EVs, rather than the overall purity.

2.5.1 METHODS OF EV CHARACTERISATION

EV samples are suspensions of heterogeneous nanoparticles in their size and composition. The characterisation of such samples is challenging from many aspects; it is important to not only discriminate between EVs and other nanoparticles but also quantify EV and non-EV materials. As for the purification methods, numerous techniques have been proposed and successfully applied to characterise and assess the purity of EVs. Despite efforts in applying and optimising characterisation methods for EVs, studies in which the characterisation methods are cross referenced are still missing. Table 5 summarises the most popular methods of characterising EV suspensions.[104] Note that methods of studying cell uptake/release and the omics of EVs have been left out. In the characterisation methods reported in Table 5, it is still difficult, if not impossible, to fully characterise an EV sample using just one method. Thus, a combination of different methods providing different information is required. It is clear that a few analytical methods, such as multi angle light scattering (MALS), surface Plasmon resonance (SPR), ATR-FTIR, and Raman, can provide information about different EV characteristics. MALS coupled with asymmetric-flow field-flow fractionation (A4F) provides valuable information about EVs, such as the root-mean-square radius (R_{rms}), geometric radius (R_{geom}), and quantity of particles.[105] SPR has been used for molecular profiling and determining the size and concentration of EVs.[106,107]

In contrast, Raman and FTIR spectroscopy provide information about the overall biochemical and protein composition[108,109] as well as particle concentration. These are valuable parameters when considering the purity of EVs purified by different purification protocols. Moreover, Raman and FTIR spectrometers are operator-independent techniques and can be used to assess the purity of EV samples by utilising the spectroscopic lipid-to-protein ratio (Li/Pr).[110,111] More traditional methods, such as Western blot, PCR, SEM, and TEM, reveal specific characteristics of EV samples, for example, the presence of specific EV markers (WB and PCR) or the morphology of EVs (SEM and TEM). Arguably, particle size distributions can also be estimated using TEM and SEM; however, these processes are extremely laborious and time consuming.

Table 4. Summary of the most common purification methods for EVs. DC = Differential centrifugation, DG = density gradient, UF = ultrafiltration, SEC = size exclusion chromatography, IMP = immunoprecipitation, A4F = Asymmetric-flow field-flow fractionation. Other exotic methods are not included.

Method		Advantages	Disadvantages
DC	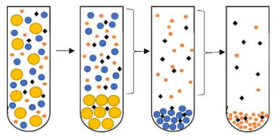	-Well-known and most used method -Easy to perform -Can be implemented with density gradients or SEC	-High g-force -Capacity of the centrifuge might be a limitation -Discriminates particles based on just their radius -Complex scale-up
EV precipitation	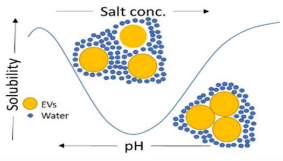	-Easy for large volumes -Low g-force involved	-Co-precipitation of proteins and impurities -Pellets might be difficult to re-suspend, which creates aggregates
DG	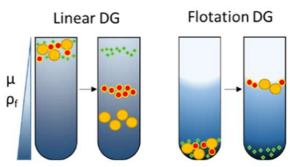	-Produces pure EV preparation -Discriminates particles based on their size and density	-Requires another step to remove iodixanol/sucrose -EVs are exposed to high viscosity and osmolarity[112]
UF	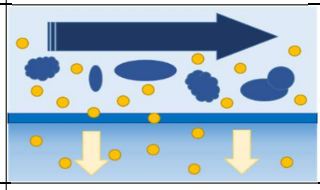	-Easy to scale up -Removes small impurities -Allows buffer exchange -Can concentrate large volumes	-Unable to remove large impurities -Final product might be highly viscous
SEC	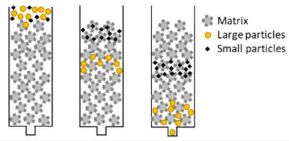	-Easy to scale up -Cost effective -Leads to pure EV preparation	-Might require a previous concentration step -EV fractions might be diluted
IMP	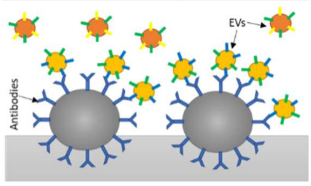	-Epitope-specific purification method -Able to discriminate between EV subpopulations	-Binding site can be saturated, which results in product lost -Target epitope must be known
A4F	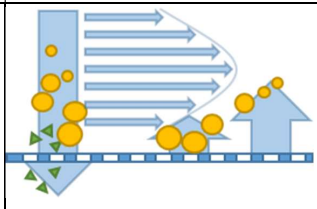	-Different types of detectors can be inserted online -Simultaneous analysis and purification	-Can process a small quantity of samples -Expensive hardware -Requires trained operators

Table 5. Summary of the most popular methods used for EV characterisation and the parameters provided by each method. ¤Methods that must be combined to assess EV purity, that is, the particle-to-protein ratio can be estimated using NTA and BCA data. "IR and RS partially resolve the protein secondary structure and physical status, but do not provide information on the particle size of EVs. *Raman can potentially be used for protein and indirect particle quantification.

Technique	NTA	DLS	MALS	WB	PCR	BCA	Raman	ATR-FTIR	AFM	TEM/TEM	SPR
Particle concentration	yes	no	yes	no	no	no	no*	yes	no	no	yes
Particle size distribution	yes	yes	yes	no	no	no	no	no	no	no	no
Protein concentration	no	no	no	no	no	yes	yes*	yes	no	no	no
Biochemical composition	no	no	no	no	no	no	yes	yes	no	no	no
EV biomarker	no	no	no	yes	yes	no	no	no	no	no	yes
Morphology	no	no	no	no	no	no	yes¨	yes¨	yes	yes	no
Quality control	no	no	yes	no	no	no	yes	yes	no	no	yes
Purity assessment	yes¤	no	yes¤	no	no	yes¤	yes	yes	yes	no	yes
Operator independent	no	yes	yes	no	no	yes	yes	yes	yes	no	yes

2.6 RAMAN AND IR IN THE EV FIELD

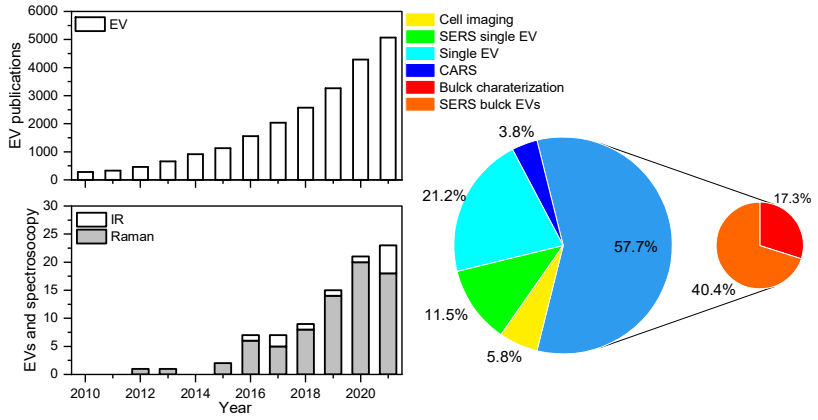

Figure 11 Number of EV-related publications from a search of PubMed with the phrases 'EV and Raman' and 'EV and IR, FTIR, and ATR-FTIR'. No results before 2012 were found.

In the last decade, interest in EVs has rapidly increased, as presented in Figure 11. Numerous studies have indicated the potential of EVs as therapeutic agents, drug carriers, and diagnostic tools. The application of vibrational spectroscopy techniques in the EV field has also increased. However, IR and Raman spectroscopy are still niche methods of studying and characterising EVs. Despite the relatively small number of publications, IR and especially Raman spectroscopy have a wide range of applications. Both techniques allow for the analysis of single EVs[113,114] as well as bulk samples.[110,111] Both methods are also able to discriminate between different EV populations and EVs of different origins.[26,115] These results underline the potential of these techniques as diagnostic tools. At first glance, IR and Raman spectroscopy appear to have the same potential and applicability in the EV field. However, Raman spectroscopy displays several advantages over its IR counterpart, mainly related to the insensitivity towards water and the fact that the Raman signal can be enhanced in different ways, as explained in the previous chapter. The most evident applications of Raman spectroscopy that cannot be executed by any IR technique are cell mapping and EV trafficking, because both applications require an aqueous environment. Arguably, cell mapping and imaging can also be performed by IR microscopy, but in dry samples. The drying process, however, might affect the morphology of the cells and compromise the results. Raman mapping has previously been used to study the passive cell uptake of small molecular drugs[60] and recently to studying EV–cell interactions.[116] Tracking cell uptake and following the distribution of EVs or nanoparticels inside the cells can help understand and optimise the use of EVs as drug carries. Theoretically, Raman spectroscopy represents a valuable candidate for such studies. It is a label-free method that can discriminate between EVs/nanoparticles and the cell components based on their chemical compositions, which can be used to

highlight where in the cells EVs/NPs accumulate and monitor eventual chemical changes. However, in practice, EVs or NPs should present a peculiar Raman spectrum or a peak that is not commonly present in cells. Cells have a heterogeneous composition, and their Raman spectra include peaks originating from amides, phosphodiester bonds, phenylalanine, and CH, CH_2, and CH_3 groups. These occupy most of the fingerprint and functional group areas in the Raman spectrum. Functional groups that are not present or poorly present in cells are polycyclic aromatics, alkynes, cyanides, and C–D bonds. The last three display Raman peaks in the region between 2000 cm^{-1} and 2500 cm^{-1}. An alternative method is to label the EV with a fluorescent dye. Both methods present the same disadvantage: native EVs do not carry fluorescence labels in the alkyne, cyanides, or C–D groups; thus, EVs must be labelled.

Raman spectroscopy has been suggested as a diagnostic tool in the EV field. This application relies upon differences in the Raman spectra of EVs from different origins. The main issues with this application are the weak Raman signal associated with the EVs and the presence of contaminants, which might mask the Raman signal. Research groups have proposed different method of overcoming these difficulties. Gualerzi et al. applied a two-step purification process; EVs where first purified from a serum via SEC and subsequently concentrated using DC. The resulting suspension was sufficiently concentrated to be measured by spontaneous Raman microscopy. Another approach to the bulk analysis of EVs is to dry an EV suspension droplet onto a structured gold substrate and measure it with time-gated Raman (TG-SERS).[73] This last method combines the advantage of SERS (enhancement of the Raman signal and analysis of diluted samples) and the advantage of time-resolved Raman spectroscopy (fluorescence suppression).[117]

Alternatively, other authors proposed methods for single-EV study. Single-particle measurements have the advantage of measuring less concentrated samples. Thus, the effects of the soluble impurities can be reduced by dilution, and non-EV particles, such as low-density lipoprotein (LDL) and high-density lipoprotein (HDL), can be excluded from the analysis. Single-particle characterisation by Raman can be obtained by either a laser tweezer objective[113,115] or SERS.[118] The SERS approach consists of a suspension of positively charged gold NPs added to a dilute EV suspension. Owing to electrostatic interactions, EVs and NPs aggregate. The EV-NP complex is then measured upon drying on a glass substrate. Among the methods proposed for diagnosis based on the Raman spectra of EVs, it is worth mentioning that the only clinical trial conducted so far was performed by Wang et al. in Brisbane, Australia. They developed a multiplex plasma EV phenotype analyser chip, which incorporated a nanomixing enhanced microchip and multiplex SERS nanotag system for direct EV phenotyping without EV enrichment.[119] Through these methods, the authors were able to detect cancer-specific EVs from the plasma of a melanoma patient and monitor the evolution of the EV phenotype throughout therapy. Moreover, the authors were able to identify the EV profiles involved in the development of drug resistance.

In addition to the characterisation of different EV populations/subpopulations, Raman spectroscopy has also been used to describe the purity of EV suspensions.[110] This method is based on the spectroscopic lipid-to-protein ratio calculated by diving

the intensity of the Raman peak associated with lipids by the intensity of the amide I peak associated with proteins. The advantages of this method compared to other EV purity assessment methods (for example, particle-to-protein ratio or EV biomarker enrichment) are that the lipid-to-protein ratio based on Raman spectra is rapid, requires little material, is operator independent, and can provide more information within one measurement.

Regarding IR spectroscopy, ATR-FTIR has recently been applied in the EV field as a tool for quantifying EVs and proteins, purity assessment, and diagnostics. In particular, ATR-FTIR spectra can be used to determine the protein concentration of EVs by integrating the amide I band area or performing PLS on the amide I and II areas.[108] This simple and operator-independent method, however, slightly overestimates the protein concentrations compared to the Bradford or bicinchoninic acid (BCA) assays. All these methods can be affected by the presence of impurities in EV samples, such as non-EV proteins or membrane phospholipids. For example, in presence of BCA, phospholipids have an absorbance peak similar to that of proteins.[120] The lack of a gold standard method for quantifying proteins in EV samples makes it difficult to conclude which method is the most accurate.

IR spectroscopy is widely used for biofluid analysis and has found applications in the characterisation of EVs. In particular, by utilising a multivariate analysis of the functional group areas, FTIR allows for the discrimination between EV subpopulations produced by the same cell line and EVs derived from different cells.[26] Moreover, nanoscale infrared biospectroscopy, which combines AFM and IR spectroscopy, allows for the study and characterisation of single vesicles.[114] AFM-IR is able to reveal the biochemical composition of single EVs and discriminate between EVs and other NPs, such as protein aggregates. Lastly, it is possible to determine a spectroscopic lipid-to-protein ratio (IR Li/Pr) using ATR-FTIR, which is an indicator of the purity of EV preparation.

3 AIMS OF THE STUDY

Biopharmaceutical and biological systems such as EVs are biochemically complex and heterogeneous. The hypothesis of this study was to reveal whether Raman and FLT measurements can add considerable value to the characterisation of complex biological systems. To test this hypothesis, different applications of biophotonics in biopharmaceutical fields were investigated. In particular, the aim was to underline the advantages of a time-gated Raman spectrometer based on CMOS-SPAD sensors in simultaneously measuring Raman spectra and FLT.

More specifically, the objectives were as follows:

1. To evaluate the potential of spontaneous Raman and IR in assessing the purity of EV suspensions [I].

2. To evaluate the efficiency of the passive labelling of EVs with fluorescent dyes and subsequent purification for cell uptake [II].

3. To exploit the potential of the simultaneous measurement of the Raman spectrum and FLT, and to evaluate the potential of Raman spectroscopy in diffusion studies [III]

4 MATERIALS AND METHODS

The main methods are presented and summarised in this chapter. For more comprehensive explanations, the reader is directed to the original publications [I]–[III].

4.2 EV PRODUCTION

EVs were obtained by the purification of cell-conditioned media (CM) extracted using CELLine AD bioreactors. The CM were then centrifuged to remove cell debris and large apoptotic bodies (2500 g for 25 min). The clarified cell-conditioned media (CCM) were then concentrated via differential centrifugation (DC) [I and II] or ultrafiltration (UF) [I]. The workflow used in studies [I] and [II] are presented in Figures 12 and 13, respectively. The setup for [III] is presented in Figure 15.

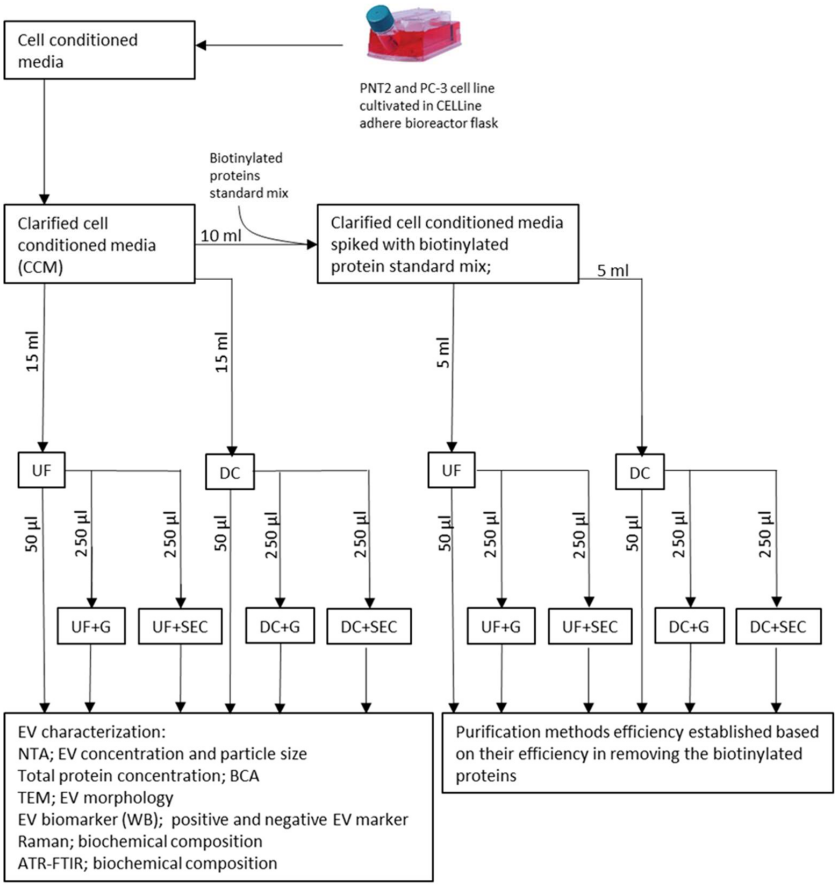

Figure 12 Workflow used in [I].

Summary of Figure 12: The CM collected by the bioreactors was processed via centrifugation to remove large particles, that is, apoptotic bodies and cell debris. The resulting CCM was then divided into three aliquots: Two aliquots of 15 ml each were used for DC and UF, while one aliquot of 10 ml was used for the spiked protein assay. Independent of volume, the aliquots, once processed by either DC or UF, resulted in a volume of ~0.6 ml. From this 600 µl, 50 µl were directly used for analysis, and 250 µl aliquots were further used for SEC and G.

4.3 EV PURIFICATION METHODS

4.3.1 DIFFERENTIAL CENTRIFUGATION

In differential centrifugation, the CCM were first centrifuged at 20000 g for 1 h, and the pellet was suspended in Phosphate-buffered saline (DPBS). The supernatant was subsequently centrifuged at 110000 g for 2 h, and the pellet re-suspended in DPBS. In [I], the pellets were combined, whereas in [II], the pellets were kept separate.

4.3.2 ULTRAFILTRATION

In Ultrafiltration, the CCM were concentrated using a filter unit with a cut-off of 10 kDa [I].

4.3.3 DENSITY GRADIENT CENTRIFUGATION

The density gradient was prepared by layering 6 ml of DPBS on top of 6 ml of iodixanol. In [I], the iodixanol used was prepared as 30% v/v in DPBS, and the EVs were loaded on top of the tube prior to one hour of equilibration. In [II], the iodixanol was prepared as 4 ml 35% in DPBS and 2 ml 45% v/v in DPBS. EVs were loaded on the 45% fraction.

4.3.4 SIZE EXCLUSION CHROMATOGRAPHY

For size exclusion chromatography, a pre-packed Superdex 200 Increase 10/300 GL column was used in [I], whereas in [II], a homemade column of a Sepharose CL-2B (diameter 1 cm, bed size ~13 ml) was used. In both cases, DPBS was the mobile phase, and 1 ml fractions were collected.

4.3.5 EFFICIENCY ASSESSMENT OF THE PURIFICATION METHODS IN REMOVING NON-EV PROTEINS

A standard protein mix of 15–600 kDa containing 0.5 g thyroglobulin bovine (MW ~670 000), 1.0 g γ-globulins from bovine blood (MW ~150 000), 1.0 g chicken egg albumin grade VI (MW ~44 300), and 1.0 g ribonuclease A type I-A from bovine

pancreas (MW ~13 700) was dissolved in DPBS to a final concentration of 3.5 mg/ml. The protein solution was then biotinylated with 4.6×10^{-7} mol of N-Hydroxysuccinimide-Biotin Reagent (NHS-Biotin) dissolved in DMSO immediately before use according to the manufacturer's protocol. Unreacted NHS-Biotin was removed by filtration with a membrane cut-off of 3 kDa at 5000 g and +4 °C, washing the retentate twice with 1 ml of DPBS. The total Biotin–Protein standard mix concentration was measured using the BSA assay. 1 mg of Biotin–Protein standard mix was added to 10 mL of 2500 g CM derived from a PNT2 cell culture and purified with the methods previously described.

Following purification, a volume containing 5 µg of the total protein from the final samples was prepared and processed according to the same WB protocol described above. For detection, the blocked nitrocellulose membranes were incubated with Streptavidin-HRP 1:500 in TBS-T for 2 h at room temperature (RT), and the obtained protein bands were visualised using an Enhanced chemiluminescence (ECL) clarity substrate and a Chemidoc MP imaging system. Signal intensities were used to estimate the residual amount of spiked proteins after purification and were normalised based on the EV number [I].

4.4 EV CARACTERIZATION METHODS

4.4.1 WESTERN BLOT

Western blot (WB) was used to detect the presence of three EV biomarkers, namely, CD9, TSG101, and Hsp70, one negative control, GM130, and a loading control, α-tubulin. CD9 is a transmembrane protein usually enriched in exosomes, and Hsp70 and TSG101 are soluble proteins [I and II].

4.4.2 NANOPARTICLE TRACKING ANALYSIS

Nanoparticle tracking analysis (NTA) was used to determine the particle size distribution and concentration of EV samples [I and II].

4.4.3 BCA ASSAY

A BCA assay was used to determine the protein concentration according to the protocol described by the manufacturer [I].

4.4.4 SPONTANEOUS RAMAN SPECTROMETER

A confocal Raman microscope (NT-MDT Ntegra, Russia) equipped with a 532 nm laser (output power ~20 mW) and a 100× objective (Mitutoyo, Japan) was used to measure the Raman spectra of EVs using backscattering geometry. The Raman peak of silicon at 520.7 cm^{-1} was used to calibrate the system daily. By measuring the full

width at half maximum (FWHM) of the silicon Raman peak at 520.7 cm^{-1}, a spectral resolution of ~4.4 cm^{-1} was confirmed with a 1800/500 grating. 2 µl of the sample with an EV concentration of approximately 5×10^{11} to 2×10^{12} were placed on a CaF_2 substrate and air dried for the Raman measurements. An exposure time of 10 s with an accumulation of two was used for the acquisition of the single spectrum. Raman spectra were measured on the edge of the dried sample. Evaporation of water from the drop induces capillary flow, which carries the dispersed material towards the edge; thus, the edge of the dry drop has a higher concentration of material than the central part. Each sample was measured five to ten times. The baseline for the Raman spectra was drawn in Origin using the baseline mode: least squares smoothing using an asymmetric factor of 0.001, threshold of 0.05, smoothing factor of 5, and number of interactions of 10 [I and II].

4.4.5 ATR-FTIR

The ATR-FTIR data of the EVs were collected using a PerkinElmer IR-spectrophotometer (Spectrum One spectrophotometer, Perkin Elmer Inc., Massachusetts, USA) equipped with the universal ATR sampling accessory (ZnSe Crystal). The measurements were performed at RT via 32 scans with a nominal resolution setting of 4 cm^{-1}. 8 µL of the sample solution with an EV concentration of approximately 5×10^{11} to 2×10^{12} were placed over the ATR crystal and dried with air flow to obtain a thin layer of EVs, which covered the entire crystal surface.

4.4.6 TRANSMISSION ELECTRON MICROSCOPY

EVs were prepared for transmission electron microscopy (TEM), as described in Puhka et al. (2017),[121] by loading EVs onto 200 carbon-coated and glow-discharged mesh copper grids with pioloform support membranes. The EVs were fixed with 2.0 % PFA in an $NaPO_4$ buffer, stained with 2% neutral uranyl acetate, further stained, and embedded in uranyl acetate and methyl cellulose mixture (1.8/0.4 %) [I and II].

4.5 EV PURITY ASSESSMENT

4.5.1 EV BIOMARKER ENRICHMENT

The relative amount of EV biomarkers detected by WB was normalised against the intensity of the same biomarker in UF samples. All the EV biomarkers chosen had an MW larger than the cut-off of UF filters; thus, the free proteins and biomarkers were also retained. The normalisation of EV biomarkers based on their expression in the cell lysate was impossible because CD9 expression in cell lysate was below the detection limit of the assay [I].

4.5.2 PARTICLE-TO-PROTEIN RATIO

The particle concentration measured using NTA was divided by the protein concentration measured using BCA [I].

4.5.3 IR LIPID-TO-PROTEIN RATIO

The total integrated intensity of the CH_2/CH_3 stretching bands from 2700 to 3000 cm^{-1} was used for the lipid component and divided by the integrated area of the deconvoluted amide I peak at 1648 ± 5 cm^{-1} (protein component), as suggested by Mihály et al.[111] [I and II].

4.5.4 RAMAN SPECTROSCOPIC LIPID-TO-PROTEIN RATIO

The lipid component was extrapolated by the total integrated intensity of the CH_2/CH_3 scissoring peak at 1445 ± 5 cm^{-1}, and the protein component was extrapolated by the total integrated intensity of the amide I peak at 1665 ± 5 cm^{-1} [I].

4.6 FLUORESCENT DYES

First, the behaviour of EVs and dye under the purification protocol was studied independently (Figure 13). This facilitated the selection of methods able to separate the unbound dye from the EVs. Second, the purification methods in which EVs and dye did not localise in the same fraction were used to remove free dye from the EV–dye complex (Figure 13).

The molecular structures of the fluorescent dyes used for EV labelling are shown in Figure 14. The light red clouds represent the hydrophobic parts of the molecules intercalating into the EV lipid membrane, and the light blue clouds indicate more hydrophilic parts, probably located in the outer surface of the EVs exposed to the surroundings. Commercially available fluorescent dyes used to label the EVs were Oregon Green™ 488 1,2-dihexadecanoyl-sn-glycero-3-phosphoethanolamine (DHPE-OG), 3,3′-dioctadecyloxacarbocyanine perchlorate (DiO), 4,4-difluoro-1,3,5,7,8-pentamethyl-4-bora-3a,4a-diaza-s-indacene (BP), 4,4′-difluoro-4-bora-3a,4a-diaza-s-indacene meso-substituted with para-dodecylphenyl moiety (BPC12),32, and a tubulin tracer dye Oregon Green 488 taxol, bis-acetate (Ptx-OG).

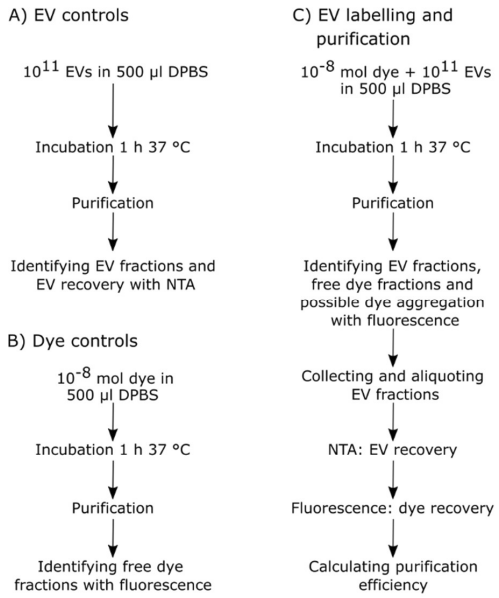

Figure 13 Workflow for A) EV control, B) dye control, and C) EV labelling and purification experiments in [II]. Adapted with permission from the publisher. DOI: https://doi.org/10.1039/D1NA00755F.

4.6.1 EV BIOMARKER ENRICHMENT

The relative quantity of EV biomarkers detected by WB was normalised against the intensity of the same biomarker in UF samples. All the EV biomarkers chosen had an MW larger than the cut-off of UF filters; thus, the free proteins and biomarkers were also retained. The normalisation of the EV biomarkers based on their expression in the cell lysate was impossible because CD9 expression in cell lysate was below the detection limit of the assay [I].

4.6.2 PARTICLE-TO-PROTEIN RATIO

The particle concentration measured using NTA was divided by the protein concentration measured using BCA [I].

4.6.3 IR LIPID-TO-PROTEIN RATIO

The total integrated intensity of the CH_2/CH_3 stretching bands from 2700 to 3000 cm^{-1} was used for the lipid component and divided by the integrated area of the deconvoluted amide I peak at 1648 ± 5 cm^{-1} (protein component), as suggested by Mihály et al.[111] [I and II].

4.6.4 RAMAN SPECTROSCOPIC LIPID-TO-PROTEIN RATIO

The lipid component was extrapolated by the total integrated intensity of the CH_2/CH_3 scissoring peak at 1445 ± 5 cm^{-1}, and the protein component was extrapolated by the total integrated intensity of the amide I peak at 1665 ± 5 cm^{-1} [I].

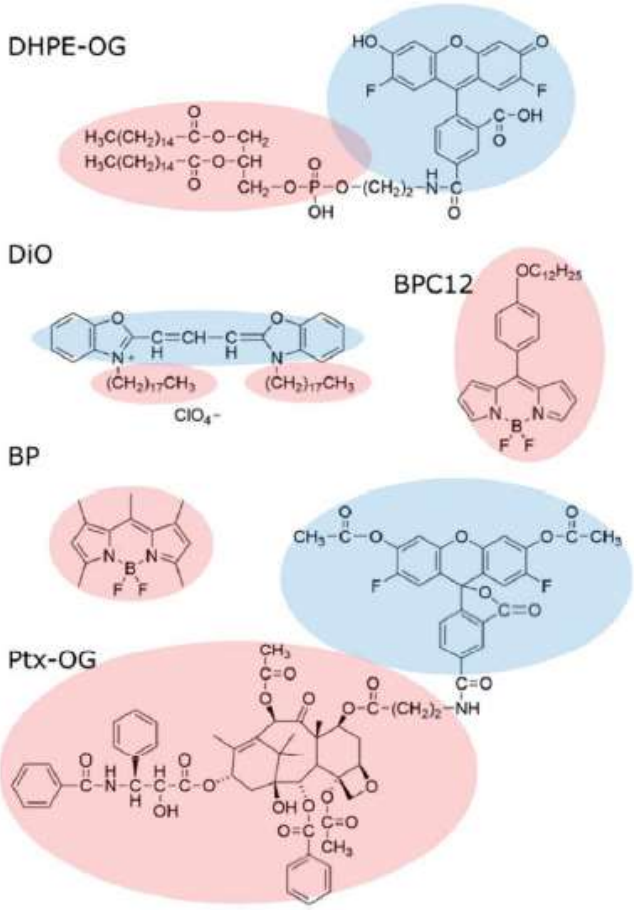

Figure 14 Chemical structure of the fluorescence dye used for EV labelling. The light blue areas indicate the hydrophilic parts, whereas the light red areas represent the lipophilic parts of the molecules. Adapted with permission from the publisher. DOI: https://doi.org/10.1039/D1NA00755F

4.6.5 PASSIVE LABELLING

Five different fluorescent dyes were used for EV labelling. BPC12 was synthesised at Tampere University, and the other dyes were purchased. The molecular structures of the dyes are presented in Figure 14. The dye stocks were solubilised in dimethyl sulfoxide (DMSO), and the emission properties of the dyes were studied without EVs in two different solutions: DPBS and solubilised in DPBS by the addition of 1% Triton X-100. The emission properties were measured with a spectrofluorometer (excitation wavelength of 483 nm, emission range 500–800 nm) to find possible aggregation-related emission bands. For dyes exhibiting clear aggregate emission, the emission spectra were also measured for the purified EVs as one criteria of purification quality. To study the purification abilities of the chosen

methods, the dye-to-EV ratio was chosen to have a significant excess of fluorescent dye. EV aliquots of 10^{11} particles were diluted to a final volume of 0.5 ml in DPBS, and 10−8 mol of dye was added to the EVs while mixing with a vortex mixer to prevent immediate aggregation of the hydrophobic dye in the aqueous buffer solution. The final DMSO concentration in the EV suspension was less than 2.5%. The labelling mixture was then incubated for 1 h at 37 °C upon shaking while being protected from light. All EV labelling was performed in triplicate.

4.6.6 EV–DYE COMPLEX PURIFICATION

Five different methods were used including UF, DC, DC+G, SEC (previously described), and anion exchange chromatography (AEC). AEC had a positively charged solid phase and two mobile phases: 30 mM of Tris-HCl (pH 7.5) and 1 M of NaCl. The samples were injected under Tris-HCl flow. The elution was performed with NaCl.

4.6.7 CONTROL PURIFICATIONS

The resolution of EV–dyes can be resolved only when the free dye behaves different to the EVs during the purification protocol. Thus, the behaviours of EVs and dye were independently studied. In the EV control, the EV recovery was determined by the ratio of EVs loaded and EVs recovered after the purification protocol. For the dye control, the fluorescence intensity was used.

4.6.8 CHARACTERISATION AFTER PURIFICATION

The particle concentrations of the EVs recovered after labelling and purification were measured with NTA to obtain the EV recovery (R_{EV}).

$$R_{EV} = \frac{N_f}{N_i} \times 100\ \%, \qquad 13$$

where N_f is the final number of EVs recovered after purification, and N_i is the number of initially-labelled EVs.

The dye concentration in the purified samples was measured against a dye calibration curve using either a plate reader (Ptx-OG, DHPE-OG, BPC12, DiO, BP UCG, and BP AEC) or fluorescence spectrophotometer (BP UC and BP UF). The fluorescence of the samples with a known amount of dye was measured to form the calibration curve. The dyes were released from the EVs and solubilised in the buffer by adding 1 % Triton X-100 to both the EV and calibration samples. Ptx-OG was hydrolysed to its fully fluorescent form by adding sodium hydroxide (0.015 M final concentration) along with 1 % Triton X-100 to both the EV and calibration samples; these were incubated at 37 °C for 1 h before the measurements. The dye recovery R_{dye} was calculated as

$$R_{dye} = \frac{n_f}{n_i} \times 100\ \%, \qquad 14$$

where n_f is the remaining molar amount of dye in the recovered EV-containing sample, and n_i is the molar amount of the dye initially added to the EV suspension for labelling.

To compare the purification results of the different methods and dyes, the relative purification efficiency E_{rp} was calculated using

$$E_{rp} = \frac{R_{EV}}{R_{dye}}. \qquad (13)$$

Given that a significant excess of dye was always used, $E_{rp} < 1$ indicates that the method concentrated the unbound dye more efficiently than the EVs. Therefore, it was not suitable for the purification of EVs after fluorescent labelling. For the methods yielding $E_{rp} > 1$, the relative purification efficiency was used to compare the suitability of the purification methods for each dye.

4.7 TIME-RESOLVED RAMAN SPECTROMETER

The time-resolved spectrometer was an in-house-built custom spectrometer. It contained a 532 nm wavelength pulsed laser as an excitation source. ~98% of the optical power was delivered to a sample through a microscope objective lens, and a small fraction (~2%) was guided to the trigger detector to synchronise the time-resolving CMOS SPAD line sensor to measure the ToA of backscattered photons from the sample. A detailed description of this time-resolved CMOS SPAD line sensor is given in reference.[122]

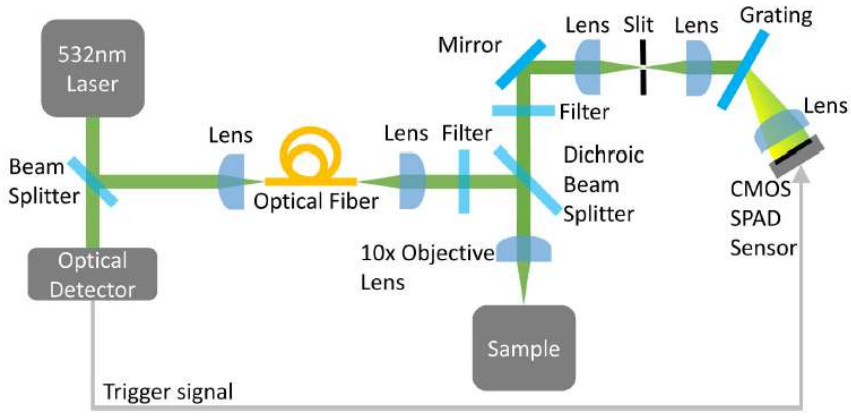

Figure 15 Block diagram of the time-resolved Raman and fluorescence measuring setup. Adapted with permission from the publisher. DOI: https://doi.org/10.1016/j.jconrel.2021.04.032.

4.7.1 DRUG DIFFUSION MEASUREMENTS

The drug molecules metronidazole and vitamin C (Vit C) in the form of dry powder were mixed with anionic nanofibrilated cellulose (ANFC) hydrogel. The drug concentration exceeded the aqueous drug solubility by approximately five times. The hydrogel concentrations were 0.9%, 0.45%, and 0.225% ANFC in Milli-Q water in m/m%. 0.75 ml of such dispersions were placed at the bottom of a 3.5 ml fused quartz cuvette and layered on top with 2 ml of ANFC with the same cellulose concentration as that of the reservoir (Figure 16).

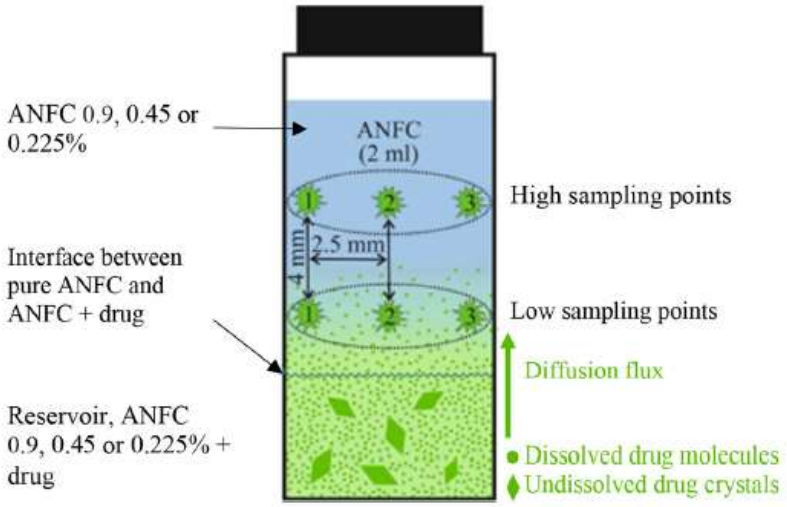

Figure 16 Schematic of sample configuration for the diffusion studies in [III]. The reservoir and pure ANFC had the same hydrogel concentration. Adapted with permission from the publisher. DOI: https://doi.org/10.1016/j.jconrel.2021.04.032.

5 RESULTS

The main results with comments are collated and summarised in Figure 17. Detailed and comprehensive presentations of the results are given in the original publications [I–III]

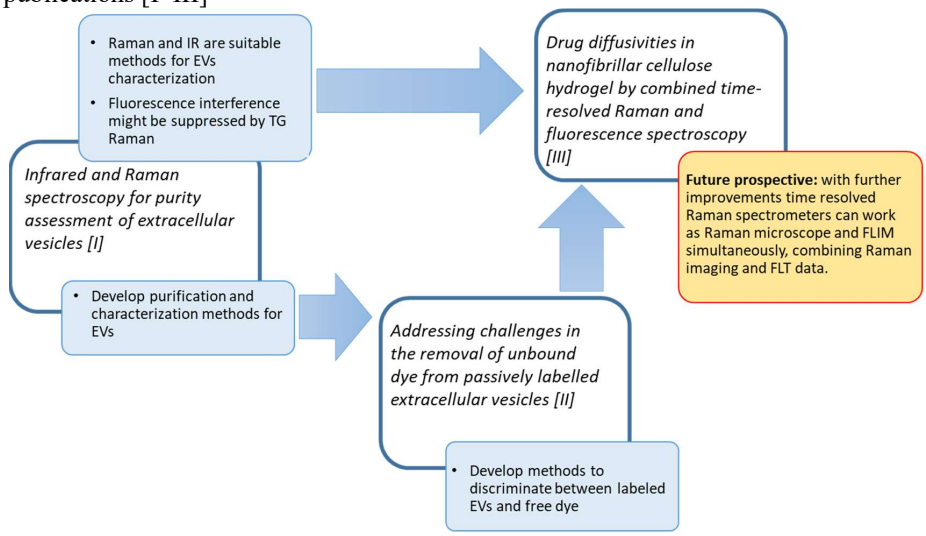

Figure 17 Summary of the main results of the study.

5.1 RAMAN AND ATR-FTIR AS PURITY ASSESSMENT AND CHARACTERISATION METHODS FOR EV SUSPENSIONS [I]

A comparison of different EV studies is often difficult owing to the lack of standardised characterisation for EV samples. MISEV 2018 states that EV suspensions should be characterised by their concentration, particle size distribution, presence of EV biomarkers, and presence of impurities, whereas the purity of the samples can be assessed by either the particle-to-protein or lipid-to-protein ratio.[110,111] For this thesis, I investigated the application of vibrational spectroscopy techniques as tools for EV characterisation and purity assessment [I]. I compare the results obtained by Raman spectroscopy and ATR-FTIR with those obtained by other commonly used methods for EV characterisation and purity assessment.

EVs derived from two different prostate cell lines, PNT2 and PC-3, were collected and purified using six different methods: differential centrifugation (DC), DC+density gradient centrifugation (DC+G), DC+size exclusion chromatography (DC+SEC), ultra-filtration (UF), UF+G, and UF+SEC. The samples were subsequently characterised by ATR-FTIR, Raman spectra, NTA, transmission electron microscopy (TEM), total protein content, and presentation of EV biomarkers (Table 6). Moreover, the purity of the EV suspensions was assessed by the spectroscopic protein-to-lipid (Pr/Li) ratio and particle-to-protein (Pa/Pr) ratio obtained via NTA and BCA measurements, as well as by EV biomarker enrichment obtained using WB.

Among the characterisation methods used, TEM and WB were able to assess only one feature of EV suspensions, that is, the morphology of EVs and the presence of EV biomarkers, respectively.

In contrast, ATR-FTIR, Raman spectra, and Pa/Pr were able to reveal various EV suspension characteristics. The Pa/Pr ratio, which is based on NTA, and BCA measurements provide data on the particle size distribution, particle numbers, and protein concentrations. ATR-FTIR and Raman spectra provide detailed information about the chemical composition of the analyte. Thus, these spectra can be used to reveal the biochemical composition of EV samples, which can be further used to assess sample purity and concentration.

In both IR and Raman spectra, the intensity of a peak is related to the concentration of the functional group that absorbs or scatters radiation at that specific frequency. Thus, both techniques, if properly calibrated, can measure the quantity of the analyte in samples.

In study [I], four methods were used to assess the purity of EVs: the spectroscopic Li/Pr obtained by ATR-FTIR or Raman spectrometry, the Pa/Pr ratio, and EV biomarker enrichment (Figure 18). The ATR-FTIR spectroscopic Li/Pr ratio was calculated by integrating the total intensity of the CH_2/CH_3 stretching bands from 2700 to 3000 cm^{-1} divided by the area of the deconvoluted amide I peak at 1648 ± 5 cm^{-1} (C=O stretching). The Raman spectrum-based spectroscopic Li/Pr ratio was obtained by integrating the total intensity of the CH_2/CH_3 scissoring peak at 1445 ± 5 cm^{-1} divided by the total integrated intensity of the amide I peak at 1665 ± 5 cm^{-1}. The Li/Pr ratio obtained from the Raman spectrum, the Li/Pr ratio obtained from the IR

spectrum, and the Pa/Pr ratio obtained via NTA and BCA suggest that DC+SEC is the most efficient purification method for both PNT2 (Figure 18A) and PC-3 (Figure 18B)-derived EVs. The Li/Pr ratio obtained via Raman spectroscopy and the Pa/Pr ratio from NTA and BCA ranked the purification protocols in the same descending order, where DC+SEC is the best, followed by DC+G, DC, UF+SEC, and UF+G, while UF is the worst for both PC-3 and PNT2-derived EVs. The Li/Pr ratio calculated from the IR spectra ranked the purification protocols in a slightly different order, with DC+SEC as the most efficient, followed by UF+SEC, DC+G, DC, UF+G, and UF.

The EV biomarker enrichment results are not consistent and differ not only between different biomarkers, but also between cell lines (Figure 18C and D).

Table 6. Evaluation of characterisation methods for EV purity.

Method	EV concentration	Particle size distribution	Protein concentration	Biochemical composition	3D structure	Identification of specific EV BM
Pa/Pr	yes	yes	yes	no	no	no
WB	no	no	no	no	no	yes
ATR-FTIR	yes*	no	yes*	yes	yes^	no
RS	no*	no	no*	yes(+)	yes^	no
TEM	no	no	no	no	yes	no

*calibration is required. IR calibration for EV protein is presented by Szentirmai et al.[108] IR calibration for EV concentration is presented [I].
(+)Raman spectrum has more detail than that of IR.
^Raman and IR spectra can reveal information on the secondary structure of proteins and the physical status.
BM = biomarker

Because there is no clear consensus in literature on which is the best purification method for EVs, I first studied the efficiency of the used purification protocols in removing non-EV proteins from EV suspensions. Thus, a biotinylated protein mixture (BPM) containing proteins of different sizes of 670, 150, 44, and 13 kDa was added to the CCM prior to purification. The efficiency in removing the BPM from the CCM for each purification protocol is shown in Figure 18E. Predictably, different purification protocols performed differently in removing the spiked BPM from the CM. The results show that DC+SEC is the most efficient method, followed by the DC+G and DC methods. The same trend was also observed for UF-based methods, where the UF+SEC outperformed UG+G and UF. Overall, the UF-based methods appear to be less efficient in removing the spiked BPM from the CM than the DC-based methods. However, these results only highlight the capability of the used purification protocol in removing soluble proteins within the size range from 1.58 ± 0.04 nm (ribonuclease A, 13.7 kDa) to 7.56 ± 0.19 nm (thyroglobulin, 670 kDa),[123] and the capability of removing larger impurities, such as organelles and small apoptotic bodies, was not assessed. Therefore, these results provide valuable information on the performance of the purification protocols. The spiked proteins with BPM were used as an additional method to evaluate the overall quality of the purification protocols; however, this still requires further optimisation.

In summary, the spiked protein method ranked the purification protocols in the following order: DC+SEC, DC+G, DC, UF+SEC, UF+G, and UF, where DC+SEC is the most efficient method in removing non-EV proteins. Among the characterisation methods, the Pa/Pr ratio obtained via NTA and BCA measurements and the Li/Pr ratio obtained using Raman ranked the purification protocols in the same order as the spiked proteins method, whereas the Li/Pr ratio obtained using IR had a slightly different order, as previously mentioned.

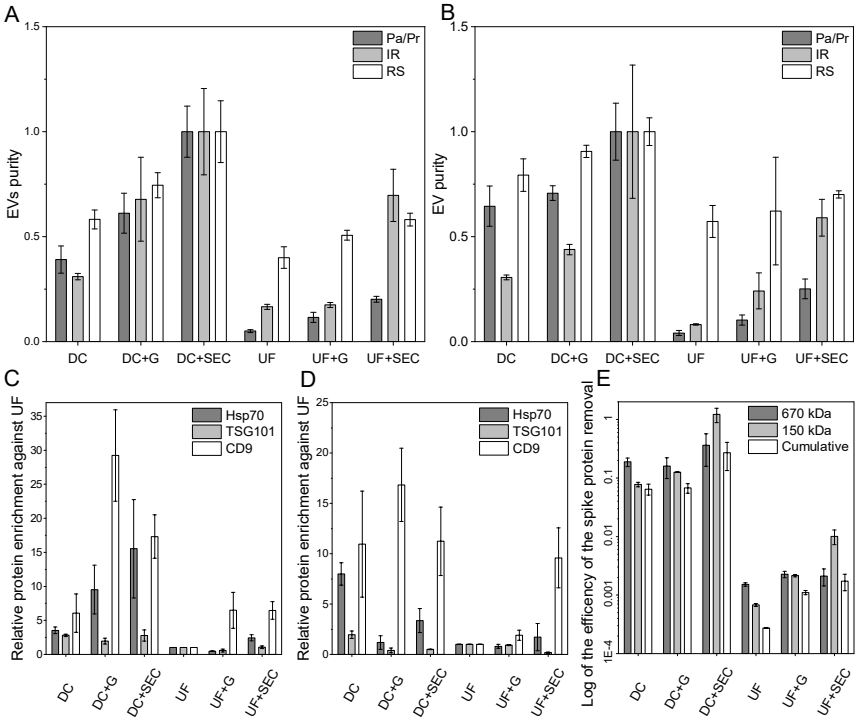

Figure 18 Evaluation of EV purity with different methods. A) and B) Evaluation of EV purity using the particle-to-protein ratios (Pa/Pr Dark grey) measured by NTA and BSA, lipid-to-protein ratios measured by ATR-FTIR (IR grey), and lipid-to-protein ratios measured by spontaneous Raman microscopy (RS, white) of PNT2 and PC-3-derived EVs, respectively. Results are normalised to the protocol, which presents the highest score (DC+SEC). C) and D) Relative EV biomarker enrichment against the UF (Hsp70 dark grey, TSG101 grey, and CD9 black) of PNT2 and PC-3-derived EVs. E) Efficiency of the protocols in removing the spiked proteins.

These differences may be due to the different vibrations used to assess the Li/Pr ratio or the different sampling techniques used. The vibrations used were CH_2/CH_3 stretching and C=O stretching for ATR-FTIR, and CH_2/CH_3 scissoring and C=O

stretching for Raman. Regarding the sampling technique, the ATR-FTIR spectrum represents the average of all the IR beam–ATR crystal surface interactions; thus, the spectrum measured represents a discrete area of the dry EV suspension droplet. However, owing to the setup used, the Raman spectrum could only be measured for a small portion (~400 nm of diameter) of the dry droplet. Thus, features of the Raman spectra can be affected by the location of measurements. However, the capillary flow induced by evaporation carries the dispersed material present in the droplet towards the edge; thus, we can assume that the EVs were mainly present at the edge of the dry droplet. This assumption is supported by the data in Figure 19, which clearly shows an increment of green fluorescence (Figure 19A); this is related to EV-associated GFP-CD9 at the edge of the droplet. Moreover, the CARS spectra confirm the presence of the CH_2 and CH_3 groups (Figure 19B) at the edge of the droplet. In particular, Figure 19C shows the intensities of the CH_2 and CH_3 CARS peaks, indicating a greater presence of such groups at the edge of the dry droplet.

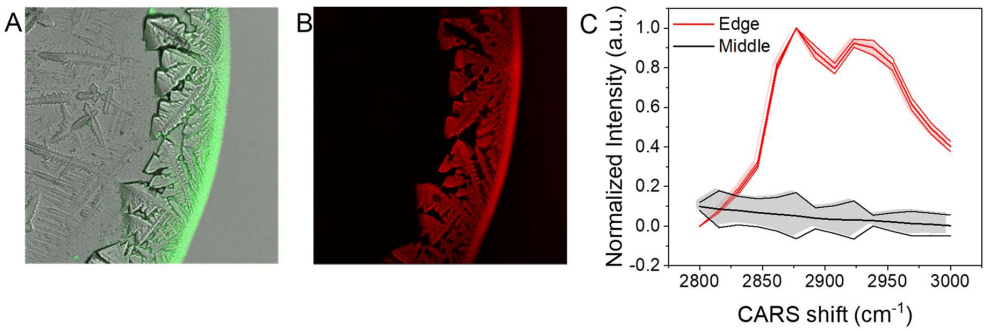

Figure 19 Fluorescence and coherent anti-Stokes Raman scattering (CARS) imagine of an air-dried GFP-CD9 EV droplet. A) Fluorescence image (green) overlapped with optical image. B) CARS spectra intensity of the same spot (red) as in A). C) Normalised average CARS spectra of figure B, where the CARS spectra of the edge of the droplet (red) is compared to the CARS spectra of the centre of the droplet (black). The shaded areas represent ± standard deviation. *Zini J. unpublished data.*

5.2 CHALLENGES IN FLUORESCENCE-BASED METHODS OF STUDYING EXTRACELLULAR VESICLES [II]

EVs must be labelled with fluorescent dyes to study the interaction and trafficking of EVs in cells, or to enhance the sensitivity for EV characterisation. In study [II], five fluorescent dyes were used for the passive labelling of two PC-3-derived EV subpopulations. The subpopulations of the EVs were purified via ultra-centrifugation (UC) and distinguished based on their sedimentation speed; the first EV subpopulation was pelleted at 20 000 g, while the second subpopulation was pelleted at 110 000 g. Subsequently, five different purification methods were used to separate the unbound dye from the labelled EVs. The five fluorescent labels used were 1) DHPE-OG, 2) DiO, 3) BP, 4) BPC12, and 5) Ptx-OG.

DHPE-OG, DiO, BP, and BPC12 are lipid tracers, whereas Ptx-OG is a tubulin tracker. These dyes have different physico-chemical properties, and therefore not all the purification methods are suitable for the separation of the unbound dye from the EV–dye complex. First, I studied the behaviour of the dyes during purification. DHPE-OG, a fluorescent conjugate of a lipid molecule, and Ptx-OG both aggregated in DPBS solution. DHPE-OG and Ptx-OG aggregated into pellets during UC and were retained by the filter in UF as EVs. Moreover, ion exchange chromatography was not suitable for removing unbound DHPE-OG and Ptx-OG because both dyes were negatively charged due to their carboxyl groups. Thus, they interacted with the gel phase and consequently eluted into the EV fraction. However, DHPE-OG could be separated from the labelled EVs by SEC and density gradient centrifugation (DC+G). In contrast, BP did not pellet during UC and was not retained by the filter during UF. Thus, UC and UF may be suitable purification methods to remove unbound BP from the labelled EVs. Furthermore, DC+G also appears to be an effective method of removing unbound BP because the EV–dye complex migrated to the interphase between the iodixanol solution and DPBS while the unbound BP remained at the bottom fraction of the tube. Conversely, BPC12 exhibited a peculiar behaviour: it interacted strongly with both the filter membrane and centrifuge tube walls during UF. These interactions could not be removed even with Triton-X washes, thus indicating the strong surface adsorption of BPC12. Furthermore, unbound BPC12 could not be separated or removed from the labelled EVs by anionic exchange chromatography (AEC) DC+G or SEC. In these three methods, the unbound BPC12 aggregates tended to be localised in the same fraction as EVs. Lastly, DiO, the most water insoluble dye, could only be removed by AEC. DiO crystallised in PBS solution; thus, it pelleted during UC and was retained by the filter membrane in UF. DiO also localised in the same EV fraction in SEC and G. The results of the EV recoveries, R_{EV}, dye recoveries in the EV fractions, R_{dye}, and relative purification efficiencies, E_{rp}, for the labelled and purified EVs are presented in Figure 20. EV recovery is the percentage of EVs recovered, and dye recovery is the percentage of dye recovered in the EV fraction after EV labelling and purification. E_{rp} is the ratio of R_{EV} and R_{dye} and represents the efficiency in removing the unbound free dye from the EV fraction. The differences in R_{EV} between the two EV subpopulations appear to be negligible. G allows the recovery

of more than 50% of EVs at 110 000 g in the case of BP, 20 000 g in the case of DHPE-OG and BP, and more than 40 % at 110 000 g in the case of DHPE-OG, whereas all other purification methods and combinations are consistently below 20% (Figures 20A and B). However, R_{dye} at 110 000 g and 20 000 g in the case of DHPE-OG indicates that a consistent fraction of the dye is recovered in the EV fraction. Conversely, R_{dye} at 110 000 g and 20 000 g in the case of BP-G is low, especially for 110 000 g, which indicates efficient purification of the unbound dye (Figures 20C and D). As expected, BP-G exhibits the highest E_{rp} among the 110 000 g and 20 000 g EV subpopulations. Despite having a low R_{EV}, AEC has only a negligible fluorescence in the expected EV fractions; thus, E_{rp} of DiO-AEC at both 110 000 g and 20 000 g is the second highest (Figures 20E and F).

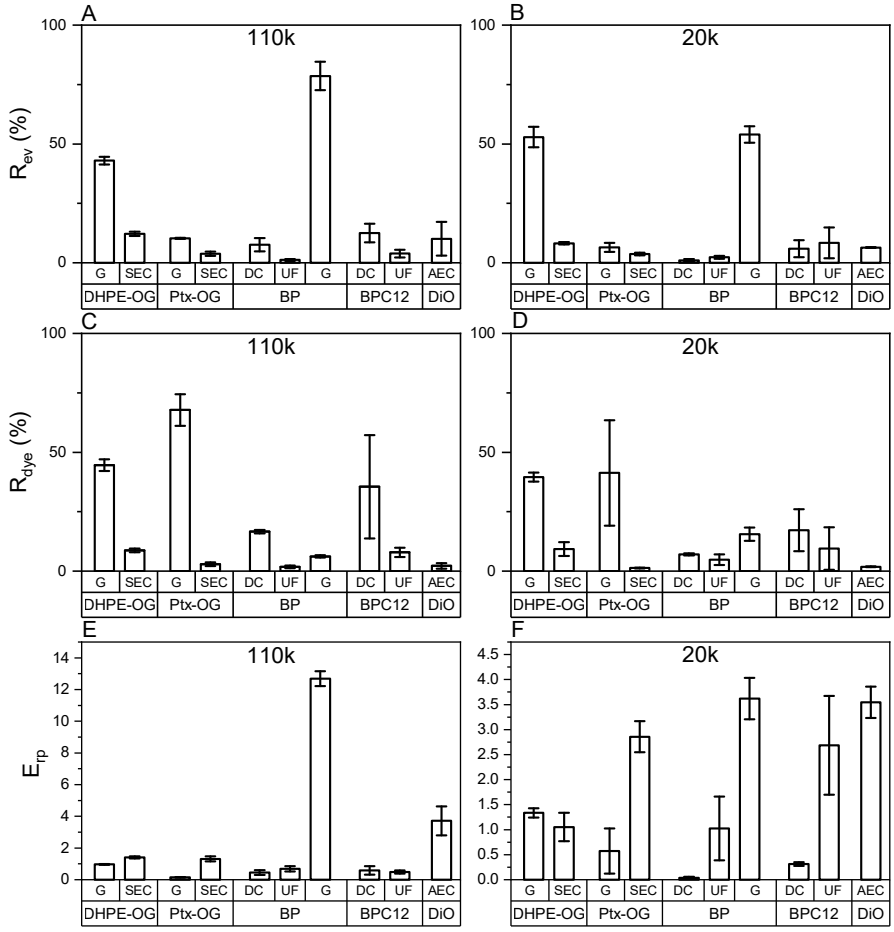

Figure 20 EV recoveries R_{EV} (A, B), dye recoveries in the EV fractions R_{dye} (C, D), and relative purification efficiencies E_{rp} (E, F) for the labelled and purified EVs. The removal of unbound dye was studied with ultracentrifugation (UC), ultracentrifugation with density gradient without ultrafiltration (G), ultrafiltration (UF), size-exclusion chromatography (SEC), and anion exchange chromatography (AEC).

It might not be sufficient to use only R_{rp} to evaluate the efficiency of the purification methods for a specific dye. Therefore, the fluorescence spectra of the purified dye–EV complexes should also be measured. BPC12-UF and -DC have similar E_{rp} values in the 110 000 g EV subpopulation, whereas the E_{rp} value for 20 000 g BPC12-UF is approximately three times higher than for 20 000 g BPC12-UC. However, the standard deviation in all four cases is high. Moreover, the aggregates of BPC12 have particle sizes that are comparable to the particle sizes of the EVs, which can further influence the reliability of the E_{rp} values.

Thus, measurement of the fluorescence spectra can help to determine whether the purification method is suitable for dye removal. Figure 21 shows a comparison of the fluorescence spectra of the monomer and aggregated BPC12 dye. The BPC12 label in its monomeric form exhibits one emission peak at 520 nm, whereas aggregated BPC12 has two peaks located at 630 nm and 700 nm. Therefore, the emission spectra of labelled EVs, as presented for BPC12 in Figure 21B, could reveal whether a purification method is efficient in removing BPC12. Figure 21B demonstrates that UF is efficient at purifying 20 000 g and 110 000 g BPC12 labelled EVs because their emission spectra present only one band at 520 nm (monomeric form of BPC12), whereas the emission spectra of 20 000 g and 110 000 g BPC12-DC exhibit a broad tail ranging from 600 to 800 nm with two clear peaks at 630 nm and 700 nm. The peaks at 630 nm and 700 nm are associated with the aggregated form of the dye, thus indicating the presence of BPC12 aggregates that have been co-purified with the EVs.

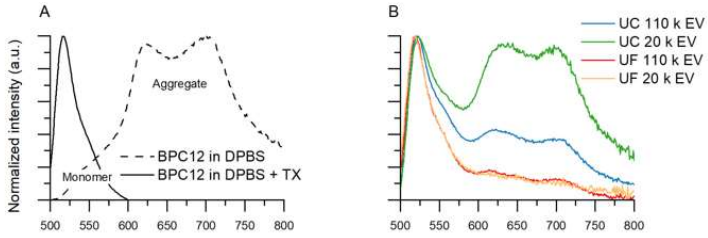

Figure 21 Fluorescence spectra of BPC12 in different conditions. (A) Fluorescence spectra of BPC12 in lipophilic and hydrophilic solutions. (B) Fluorescence spectra of EVs labelled with BPC12 and purified by DC. Adapted with permission from the publisher. DOI: https://doi.org/10.1039/D1NA00755F.

Unfortunately, all the purification methods proposed to remove unbound dyes led to a substantial loss or dilution of labelled EVs. Therefore, the characterisation of labelled EVs by Raman and IR was impossible with these systems.

5.3 COMBINING TIME-RESOLVED RAMAN AND FLUORESCENCE SPECTROSCOPY IN A DIFFUSIVITY STUDY [III]

In study [III], an in-house-built Raman spectrometer equipped with a time-gated SPAD sensor fabricated with HVCMOS technology was used to study the diffusion of small molecular drugs in a hydrogel. The advantage of CMOS SPAD circuits is that they can resolve the ToA of photons relative to the laser pulse. This capability enables the realisation of a time-resolved Raman spectrometer that measures the spectral and temporal distributions of the scattered photons (Figure 22). Thus, the spectral resolution is used to measure the Raman spectra, while the temporal distribution reveals the FLT of the analyte. Moreover, in the data post-processing phase, the time-gate width can be adjusted to suppress fluorescence disturbance. Figure 23 shows the comprehensive Raman spectra and FLT of Vit C as powder in water and ANFC solution, measured with the COMS SPAD Raman spectrometer.

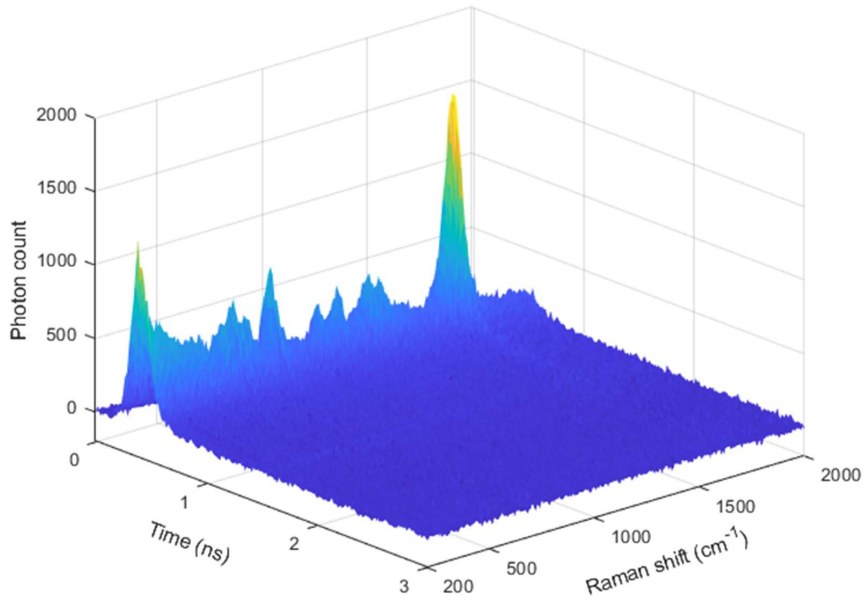

Figure 22 Combined 3D time-resolved Raman and fluorescence spectra of vitamin C.

As expected, the Raman spectra reveal information on the chemical composition and physical state of the sample. The C=C stretching band is the most intense peak in the spectra and is present both in the crystal and solution form of Vit C (1665 and 1692 cm^{-1}, respectively). The peaks at 642, 1129, 1257, and 1321 cm^{-1} are related to the –OH deformation, C–O–C stretching, C–O–H, and C–H bending of

the solid form of the material, respectively. The Raman spectra of Vit C in water solution and an anionic nanofibrillated cellulose (ANFC) hydrogel are similar, and both display intense peaks at 1692 cm^{-1} (C=C) and 830 cm^{-1} (C–C stretching). For complete peak assignments for the Vit C spectra, see Table 7.

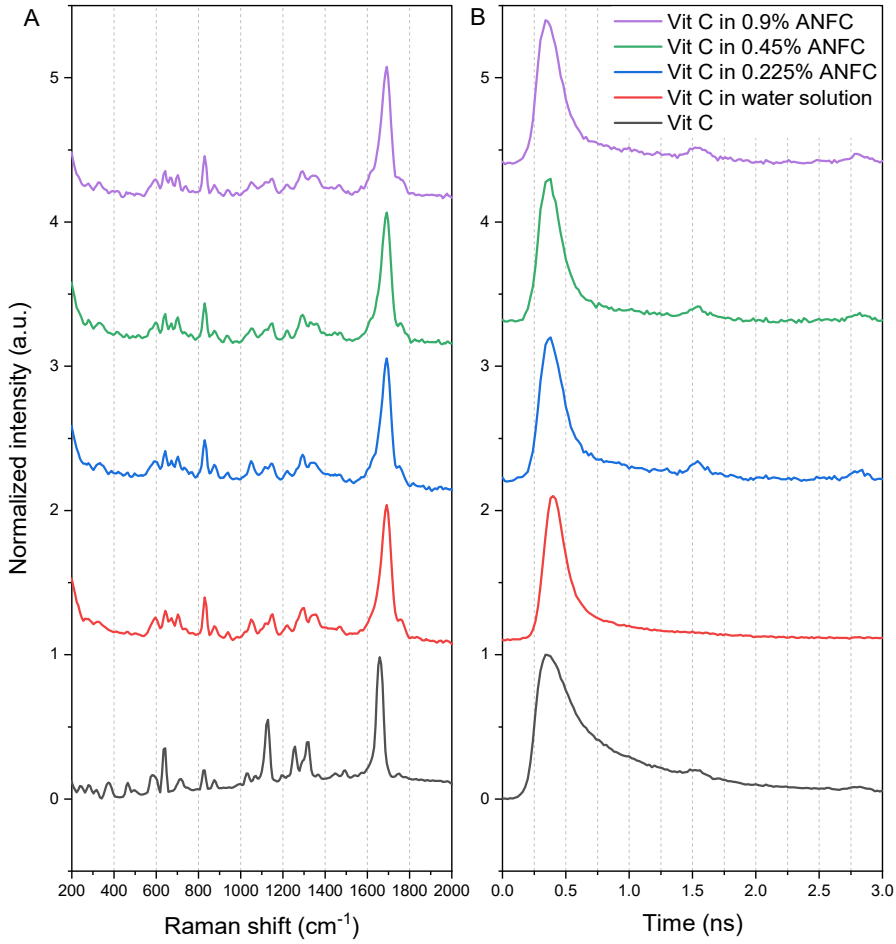

Figure 23 Raman spectra and FLT of Vit C in crystal form, in water solution and solution with ANFC. (A) Raman spectra of Vit C in ANFC 0.225% (purple), 0.45% (green), 0.225% (blue), saturated water solution (red), and solid form (black). (B) FLT of Vit C in ANFC 0.225% (purple), 0.45% (green), 0.225% (blue), saturated water solution (red), and solid form (black).

Changes in Raman spectra between different Vit C formulations are expected; they underline the different physical statuses of the drug (powder and water solutions). The Raman spectra of Vit C in water and hydrogel solutions are similar, indicating that ANFC does not interfere with Raman spectra measurement. Molecular interactions

between Vit C and water are similar to the interactions of Vit C and ANFC, as also reported in Table 7. The FLT of Vit C in different ANFC concentrations are also similar, which confirms the previous speculation.

The amplitude of the 1692 cm^{-1} and 830 cm^{-1} peaks were subsequently used to monitor the diffusion of Vit C in ANFC hydrogel. Figure 24 shows the Raman and fluorescence spectra of Vit C at different time points. It is clear that the intensity of the peaks increases over time, which indicates diffusion of the drug in the hydrogel (Figure 24 B, E, and H). Furthermore, the temporal distribution of the photons reveals that the FLT of Vit C remained stable throughout the experiment (Figure 24C, F, and I), indicating that there were no changes in the interactions between the hydrogel and drug. The diffusion coefficients of Vit C and metronidazole measured using Raman are reported in Table 8.

Table 7. Peak assignments for Vit C Raman spectra.

Vit C in solid state	Vit C in water	Vit in ANFC	Assignment
642 (s)	642 (vw)	642 (vw)	OH out-of-plane deformation C–C ring stretching
718 (w)	702 (vw)	702 (vw)	OH out-of-plane deformation
830 (s)	830 (s)	830 (m)	C–C ring stretching
1028 (w)	1050 (w)	1050 (w)	C–O–H bending, C–O–C stretching
1129 (s)	1151 (vw)	1151 (vw)	C–O–C stretching
1257 (m)	-	-	C–O–H bending (twisting)
1321 (m)	1349 (vW)	1349 (vw)	CH bending (wagging)
1453 (vw)	1467 (vw)	1467 (vw)	CH bending
1665 (s)	1692 (s)	1692 (s)	C=C ring stretching

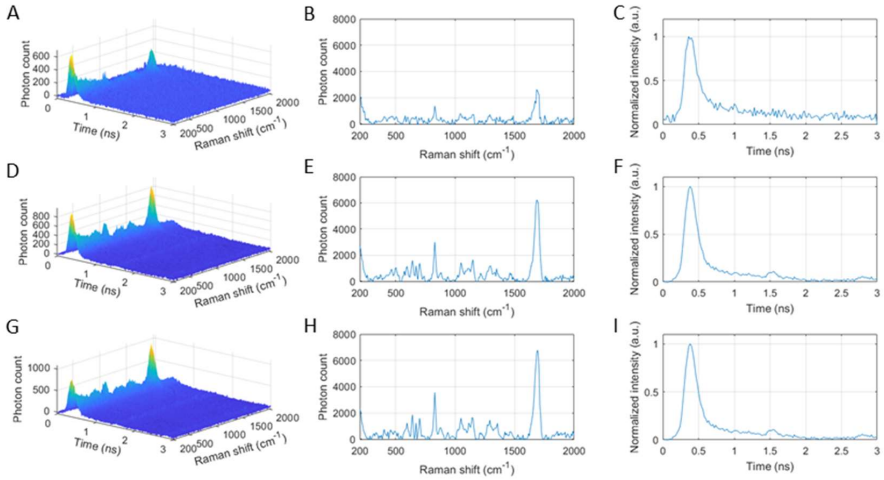

Figure 24 Combined 3D time-resolved Raman and fluorescence spectra of Vit C measured after 5 h, 24 h, and 48 h in 0.9 % anionic nanofibrillated cellulose (ANFC) hydrogel (figures A, D, and G on the left). The figures on the right show the post-processed time-gated Raman spectra with a time-gate width of 600 ps. The data was collected from the lower sampling point 2 (see Figure 15).

Table 8. Diffusion coefficients of Vit C and metronidazole in various ANFC concentrations based on Raman measurements and theoretical fitting, and the values in water found in literature. Diffusion coefficients are expressed in 10^{-6} cm^2/s

	D in 0.225% ANFC	D in 0.45% ANFC	D in 0.9% ANFC	D in water
Vit C	5.0	6.0	4.8	5,32±0.26[124] 6.8±0.6[125]
Metronidazole	15	10	n.d.	4.3[126]

Vit C is a small hydrophilic molecule, and its diffusion does not appear to be affected by the ANFC concentrations used. Because Vit C is not retained by low concentrations of ANFC, it is logical that its diffusion coefficient in such hydrogels resembles that in water. However, metronidazole appears to diffuse faster in ANFC than in water. Moreover, its diffusion coefficient is higher in ANFC (0.45% and 0.225%) than in water. This might be explained by the hydrophobicity of the drug.

6 DISCUSSION

6.1 RAMAN AND IR FOR EVS [I]

The purity level of EV suspensions purified by six different methods was assessed using ATR-FTIR and Raman spectra. These results were compared to the particle-to-protein (Pa/Pr) ratio obtained via NTA and BCA measurements and the relative EV biomarker enrichment results determined by WB. The lipid-to-protein (Li/Pr) ratio and Pa/Pr ratio calculated from Raman spectra ranked the purification methods according to their efficiency in removing the spiked proteins from CM. However, the Li/Pr ratio obtained from IR spectra ranked the purification methods in a slightly different order. These small differences between the Raman and IR results might be due to the different vibrations used to calculate the lipid and protein components. The CH_2/CH_3 symmetric and asymmetric stretching between 2800 and 3000 cm^{-1} were used as the lipid component and the C=O stretching at 1445 cm^{-1} of the peptide backbone (amide I) as the proteins when determining Li/Pr via the IR method.[111] In the case of Raman spectra, the C=O stretching of amide I (1661 cm^{-1}) for the protein components and the CH_2/CH_3 band and stretching (1441 cm^{-1}) for the lipid component were used to determine the Li/Pr ratio.[127,128] It is challenging to use the same vibrations for lipids and proteins in both techniques because of the complementary nature of Raman and IR spectra. The bands present in Raman spectra are due to changes in the polarisability of the chemical bonds during the vibrations. The chemical bonds that are sensitive to the changes in polarisability are relatively neutral in nature (C–C, C=C, and C–H). IR active bands, however, are linked more to polar bonds (C–O and O–H), which undergo changes in the dipole moments during the vibrations.

These results, along with those of other studies,[110,111] suggest that the Li/Pr ratio obtained by IR and Raman measurements is a reliable indicator of the purity of cell-derived EV suspensions. However, two significant issues remain unsolved: i) Until now, there have been no studies on the use of IR and Raman spectroscopy for the purity assessment of blood- or plasma-derived EVs, and ii) there are no studies in which different methods of measuring IR or Raman spectra are challenged.

Regarding lipoproteins, HDL and LDL are common impurities found in blood- and plasma-derived EVs and are also lipid-enriched particles with a size and density comparable to EVs. Thus, they can be co-purified with EVs in DC, UF, and precipitation-based methods. Therefore, the spectroscopic Li/Pr ratio of blood- or plasma-derived EV samples might be high because of the presence of lipids from the HDL and LDL particles.

The interference of HDL and LDL in IR and Raman spectra might be overcome by applying more advanced data post-processing to the spectra, such as PCA or Partial least squares regression (PLSR). Therefore, the quality of EV suspensions, which might include lipoproteins as impurities, can be deduced by comparing the suspension spectra with the spectra of pure lipoproteins or EVs. There are currently no studies published in this area; however, both techniques have successfully been used to

differentiate EVs with different origins.[26,113,115] Thus, IR and Raman spectroscopy can both potentially distinguish EVs from HDL and LDL.

Furthermore, the sampling technique used to acquire the IR or Raman spectra might have affected the results of the study. There is little discussion on the performance of IR spectroscopy in measuring aqueous suspension because ATR-FTIR has clear advantages; however, discussions on the measurement method of EV Raman spectra are ongoing. At the time of writing, different methods have been proposed: measuring EV spectra by randomly mapping the centre and edges of an air-dried EV suspension on CaF[129] or by measuring the Raman spectra at the edge of an air-dried EV suspension on a gold NP-coated surface.[130] Alternatively, EVs can be measured directly in suspension, either with single-particle analysis[113] or by enhancing the signal with SERS.[131] Despite growing interest and publications on the use of Raman in the EV field, the various Raman methods have not yet been compared. It must be noted that Samoylenko et al. measured the spectra of different EVs in suspension with TG-Raman and conventional continuous-wave excitation Raman. Subsequently, they further enhanced the Raman signal using Ag NPs.[132] However, the spectra reported by Samoylenko et al., obtained using TG, CW, and TG-SERS, displayed few similarities.

Raman and IR spectroscopy have been used to differentiate between EVs derived from healthy cells and EVs originating from cancerous cells. Owing to their ductility, Raman spectra have been further applied in this specific field. In particular, Raman spectroscopy has been used to detect EVs released in neurodegenerative diseases and after ischemic episodes. Overall, Raman spectroscopy appears to outperform its IR counterpart in various applications related to EVs. It can be speculated that Raman spectroscopy is a more ductile technique. For example, Raman microscopy has a better resolution than IR, that is, 300 nm vs 3–30 μm,[133] respectively.

Raman and IR spectrometers can be combined with atomic force microscopy (AFM) to obtain both spatial and chemical information. Additionally, Raman signals can be enhanced by utilising tip-enhanced Raman scattering (TERS) in AFM. Lastly and most importantly, Raman signals are not as sensitive to water as those of IR. This advantage of Raman spectroscopy is particularly important from the perspective of EV production. Time-gated Raman spectrometers can be used to measure the Raman spectra of EV suspensions through glass or plastic containers, thus enabling the use of Raman spectrometers as a PAT tool for the real-time quality control of EVs.

6.2 FLUORESCENCE LABELS IN EV STUDIES [II]

In study [II], we applied previously acquired knowledge of EV characterisation and purification related to the labelling and removal of unbound dye from passively labelled EVs. EV interactions with tissue and cells have been extensively studied using fluorescence-based methods.[134–137] Passive labelling, which consists of the incubation of EVs with lipid-tracer fluorescent dyes, is the most common method of EV labelling. Independent of the protocol used for EV labelling, not all labels are taken up by the EVs. Thus, the labelling process results in a complex mixture of labelled EVs and free labels.[138–140] The unbound dye might affect the outcome of studies and therefore must be removed. The methods used to separate the free dye from the EV–dye complexes

are usually the same as those used for EV purification. These methods include DC,[136] filtration/ultrafiltration,[136] and SEC,[141] which are the same methods as those used for EV purification in study [I]. Subsequently, the purified labelled EV suspensions should be characterised in a qualitative and quantitative manner to facilitate the reproducibility and comparison of published material found in literature. In this study, it was first proposed to investigate the behaviour of free dye in the chosen purification method and EV recovery. These two parameters can clarify whether the free dye localises in the EV fraction (that is, pellet for the DC or EV fraction in SEC/AEC) and the amount of EVs recovered after purification. Subsequently, E_{rp} was suggested as a parameter to describe the success of the purification protocol. E_{rp} represents the EV-recovery-to-dye-recovery ratio and can be used as an approximate parameter to rapidly assess the performance of purification methods in removing free dye. However, E_{rp} introduces an intrinsic error; EV recovery is evaluated by NTA measurements, which are not able to distinguish EVs from other particles, such as dye aggregates. Thus, dye aggregates can artificially increase the particle count, which is reflected in a faulty increase in the EV recovery. Another critical point of E_{rp} is the dye recovery ratio, which does not discriminate between the dye present in the EVs and the unbound dye co-purified with the EV–dye complex.

Another rapid method proposed to evaluate the quality of labelled EV suspensions is the acquisition of the fluorescence spectra of the dye, which reveals the physical state of the dye, that is, whether the dye is aggregated or in its monomer form. This method can per se reveal the relative quantity of the aggregated or monomeric dye; however, it does not reveal quantitative information on the number of labelled EVs. Thus, fluorescence measurements should be combined with other quantitative measurements. Lastly, it is worth noting that, in the case of EV–cell interaction studies, the FLIM image of the free dye and dye–EV complex should be presented together. This can help distinguish between signals originating from the free dye and the signal from the EV–dye complex.

Based on this study, it can be concluded that there is no purification method suitable for all the dyes used in EV labelling; therefore, the purified and labelled EVs should be thoroughly characterised in each case.

Other methods have been suggested for characterising the dye–EV complex. Asymmetric-flow field-flow fractionation (A4F) coupled to a multi-angle light-scattering detector (MALS)[46] is a promising technology for EV characterisation and can be considered a gold standard for EV particle quantification and size distribution studies. However, A4F is usually coupled to a MALS, DLS, or UV detector, which are not able to discriminate between fluorescent and non-fluorescent particles. Therefore, A4F-MALS/DLS is not able to differentiate EVs from other particles, such as dye aggregates, in labelled EV preparation. Nonetheless, studying the fractograms of EVs, labelled EVs, and free dyes can reveal information on the efficiency of purification methods in removing free dye. Moreover, A4F analysis is time consuming and requires expensive instrumentation, which may not be available in all laboratories.

Unfortunately, in this study, the concentration of the dye–EV purified complexes was too low to be characterised by either the Raman or ATR-FTIR spectrometers in these processes. However, other set-ups, especially laser tweezer objectives, would

enable an in-depth characterisation of EV–dye complexes, as well as provide an estimate on the quantity of dye aggregates.

6.3 CMOS SPAD RAMAN SPECTROMETER FOR DIFFUSION MONITORING [III]

In study [III], an in-house-built custom-planned time-resolved Raman spectrometer based on a CMOS SPAD line sensor was shown to measure the Raman spectra as well as the FLT of drugs during their diffusion in a hydrogel. This study had two different outcomes that will be discussed separately. First, the applicability of the Raman spectrometer as a tool for diffusion studies, and second, the combination of Raman and FLT spectra for analyte characterisation.

Diffusion of the drug was monitored by utilising the amplitude of the Raman spectra peaks attributed to the analysed drug. The use of a spectroscopic technique for diffusion studies is not a novelty per se; however, in most studies performed to date, a UV-Vis spectrometer has been used.[126,142] UV-Vis spectroscopy has several advantages over that of Raman; UV-Vis spectrometers are cheap, easy to use, and are well suited for studying the diffusion of drugs in water. However, in most cases, UV-Vis spectrometers detect only one wavelength. Thus, information on the chemical structure obtained by UV-Vis spectrometers is limited. Moreover, UV-Vis spectroscopy is based on the absorption of UV or Vis light and the following emission of photons at a lower energy. Thus, part of the incident light energy is dissipated into radiationless phenomena, including heat. Temperature plays a significant role in the diffusion of molecules and particles; therefore, heating of the system during measurement might affect the results.

In contrast, Raman spectra provide exhaustive information on the chemical composition and physical state of drugs, and the amplitude of the peaks can be correlated to the concentration of the analyte.[143] Moreover, the intensities of the Raman peaks are additive. Thus, it is possible to subtract the spectra of the medium or hydrogel in which the diffusion study is performed. In the case of this study, this was not necessary because the concentrations of ANFC were low (0.225%, 0.45%, and 0.9%) and therefore had a negligible effect on the measured peak intensities.

Raman spectrometry is based on the inelastic scattering of light, which is a two-photon phenomenon that occurs at low energies. The electromagnetic radiation used in Raman studies has less energy than UV-Vis. Therefore, heating of the samples is less likely to occur in Raman studies.

This advantage of Raman spectroscopy compared to UV-Vis was utilised in the present study by performing measurements using a time-gated Raman spectrometer.

Time-gated Raman spectrometers enable the suppression of background fluorescence. Moreover, they can differentiate photons based on their ToA. Thus, the signal from the container of the hydrogel can be excluded. Again, in this study, this was not necessary because a quartz cuvette was used.

The CMOS SPAD line sensor can be used to measure Raman spectra as well as FLT. These two spectra reveal different information about the sample. Raman measurements clearly reflect changes in the physical state (that is, ascorbic acid in

solution or crystal form in this study) and chemical composition of the analyte. Thus, it is possible to monitor changes in the chemical structure, which might be linked to the decomposition or hydrolysis of the analyte. Raman spectra can also be used for qualitative analysis. The Raman spectrum of a mixture of different molecules is equal to the weighted sum of the Raman signals of the mixed components. This linear superposition can be used to distinguish between the media signal and analyte signal. However, it is important to note that chemical interactions between the components of the mixture may significantly modify their Raman spectra. Thus, in case of significant changes in the spectra, the principle of linear superposition may not be applied to the pure component but to the spectra of the mixture.

Conversely, Raman spectra do not reveal information on the environment in which the analyte is located. This information can be deduced by FLT decay.

7 FUTURE PROSPECTS

Vibrational spectroscopy, especially Raman spectroscopy, is a powerful tool that can qualitatively, quantitatively, and non-destructively resolve the composition of complex samples. Owing to these properties, these techniques are particularly suitable for the study and characterisation of biological samples and in biopharmaceutical production. This thesis highlights two diverse aspects of Raman spectroscopy that are applied in the biopharmaceutical field and opens a path to different prospects. First, this study and associated publications confirm that Raman and IR spectroscopy can be used to assess EV suspension purity and potentially be used as quality control tools in EV production. At the time of writing, there are no clinical applications of EVs or any EMA or FDA guidelines for EV production. However, vibrant interest in EVs as diagnostic or therapeutic tools could soon bring these biological NPs into clinical use. In this context, Raman spectroscopy is a strong candidate for both applications. However, there are still several issues to be resolved to promote and facilitate the transition of Raman spectrometers from research laboratories to a clinical or industrial environment. Biological samples are complex to analyse, and there is often fluorescence interference present. The spectrometers available in the market are currently state-of-art research tools, which are complex and costly. However, time-gated Raman spectrometers based on a time-resolved CMOS SPAD sensor have a reduced size, complexity, and cost compared to traditional Raman devices. Additionally, the time-resolved CMOS SPAD sensor can discriminate photons based on their ToA; thus, it is able to separate the Raman signal from the fluorescence tail. CMOS SPAD sensors utilising the time-correlated single-photon counting procedure allow a wide time gate, which can be modified in the data post-processing phase to obtain the best possible Raman signal-to-noise ratios. Moreover, this enables the simultaneous measurement of FLT. Fluorescence suppression is useful in both biopharmaceutical production and research. In particular, fluorescence suppression can be used to characterise EVs with fluorescent dyes. Laser tweezer Raman spectroscopy or other single-particle analysis techniques have already been used to characterise single EVs. However, with labelled EVs, the fluorescent dye might heavily interfere with this characterisation. Thus, single-EV studies performed with a time-resolved Raman spectrometer could theoretically analyse the EV–dye complex and distinguish it from other particles.

Moreover, the CMOS SPAD-based Raman spectrometer could also be used to study the diffusion of EVs in a hydrogel; EVs produce a weak Raman spectrum and as such cannot be measured in low concentrations. However, EV diffusion could be studied by labelling the EVs with a fluorescent dye. Furthermore, using a CMOS SPAD sensor to measure the FLT of diffusing particles could confirm that the molecular rotor is effectively present in the EVs and that it is not diffusing out, and the diffusion of the EV–dye complex could be studied by the overall (Raman and fluorescence photons) signal intensity.

Subsequently, a CMOS SPAD sensor-based Raman spectrometer could be further implemented by exploiting the capability of such an instrument to discriminate photons based on their ToA.

Owing to the wide time-gate range of CMOS SPAD sensors, Raman spectrometers equipped with these sensors could be implemented in multiport spectrometers, allowing the measurement of Raman spectra at different points in space. CMOS SPAD sensors can discriminate photons based on their ToA; thus, the laser pulse generated by the laser source can be conducted to different Raman probes by glass fibres of different lengths. Because of differences in glass fibre length, photons will travel from the laser source to the sample in different times. This difference in time is preserved by the scattered Raman photons traveling from the Raman probes to the spectrograph with the sensor. This solution can dramatically reduce the cost of time-resolved Raman spectrometers because it allows one spectrometer to measure spectra at different points, which can be useful in the manufacturing of biopharmaceutical products. As an example, the EV production could be monitored by measuring the Raman spectra at different stages of the purification protocols.

Furthermore, CMOS SPAD sensors could potentially be used and implemented in SRS spectrometers. SRS signals are generated when the energy difference between the two co-aligned beams matches the molecular vibration, which results in an excitation of the Raman active molecular vibration. Thus, SRS spectrometers have two lasers, pump and Stokes beams, with the latter enhancing the Raman signal in a small part of the spectrum. CMOS SPAD-based Raman spectrometers could theoretically be equipped with Stokes beams of different wavelengths, which could be synchronised to fire at precise intervals, resulting in an enhancement of all Raman spectra.

Finally, CMOS SPAD sensors could also be utilised in Raman-FLIM imaging. A time-resolved Raman microscope equipped with this sensor could provide a combination of Raman imaging and FLIM data, thus highlighting the cellular distribution of the fluorophore and its environment by measuring the FLT, because FLT is susceptible to viscosity and pH. Moreover, Raman data could help to elucidate the chemical composition of the samples.

8 CONCLUSIONS

I. Raman and IR can be used to assess the purity of EV suspensions. Both techniques are rapid, operator-independent, label-free, and require a small amount of the sample. Neither IR nor Raman spectroscopy are able to fully characterise an EV suspension per se. Thus, they should be coupled with methods that are able to measure particle size distributions and the presence of EV biomarkers.

II. Labelling EVs with fluorescent dyes is a challenging process. The efficiency of the purification method in removing the unbound dye may change based on the dye and EVs used. The EV–dye complex should be thoroughly characterised, and the possibility of dye leakage from the EV–dye complex should be considered in fluorescence-based measurements, such as FLIM studies.

III. A time-resolved Raman spectrometer based on a CMOS SPAD sensor can be used to study the diffusion of a drug through hydrogels by simultaneously recording the Raman spectra and FLT.

IV. The development of time-resolved Raman spectrometers could help to overcome bottlenecks in pharmaceutical and clinical applications of EVs. For example,

a. A multiport CMOS SPAD sensor Raman spectrometer could be used to monitor the different steps in EV production and purification in an automated manner. Combined with the implementation of statistical methods, this could be used as a PAT tool.
b. Single-particle analysis could differentiate between fluorescence dye aggregates and EV–dye complexes.
c. Implementation of Raman CMOS SPAD devices as Raman-FLIM for intracellular EV trafficking.

REFERENCES

1. Einstein, A. Über einen die Erzeugung und Verwandlung des Lichtes betreffenden heuristischen Gesichtspunkt. *Annalen der Physik* **322**, 132–148 (1905).

2. Lewis, G. N. The Conservation of Photons. *Nature* **118**, 874–875 (1926).

3. Vankeirsbilck, T. *et al.* Applications of Raman spectroscopy in pharmaceutical analysis. *TrAC Trends in Analytical Chemistry* **21**, 869–877 (2002).

4. Saarinen, J. Non-linear Label-free Optical Imaging of Cells, Nanocrystal Cellular Uptake and Solid-State Analysis in Pharmaceutics. 102.

5. Buckley, K. & Ryder, A. G. Applications of Raman Spectroscopy in Biopharmaceutical Manufacturing: A Short Review. *Appl Spectrosc* **71**, 1085–1116 (2017).

6. De Bruyne, S., Speeckaert, M. M. & Delanghe, J. R. Applications of mid-infrared spectroscopy in the clinical laboratory setting. *Critical Reviews in Clinical Laboratory Sciences* **55**, 1–20 (2018).

7. Grdadolnik, J. ATR-FTIR spectroscopy: Its advantages and limitations. *Acta Chimica Slovenica* **49**, 631–642 (2002).

8. Bassan, P. *et al.* The inherent problem of transflection-mode infrared spectroscopic microscopy and the ramifications for biomedical single point and imaging applications. *Analyst* **138**, 144–157 (2012).

9. Morisseau, K. M. & Rhodes, C. T. Pharmaceutical Uses of Near-Infrared Spectroscopy. *Drug Development and Industrial Pharmacy* **21**, 1071–1090 (1995).

10. Zeeshan, F., Tabbassum, M., Jorgensen, L. & Medlicott, N. J. Attenuated Total Reflection Fourier Transform Infrared (ATR FT-IR) Spectroscopy as an Analytical Method to Investigate the Secondary Structure of a Model Protein Embedded in Solid Lipid Matrices. *Appl Spectrosc* **72**, 268–279 (2018).

11. Lima, C. A., Goulart, V. P., Côrrea, L., Pereira, T. M. & Zezell, D. M. ATR-FTIR Spectroscopy for the Assessment of Biochemical Changes in Skin Due to Cutaneous Squamous Cell Carcinoma. *Int J Mol Sci* **16**, 6621–6630 (2015).

12. Sun, X., Xu, Y., Wu, J., Zhang, Y. & Sun, K. Detection of lung cancer tissue by attenuated total reflection–Fourier transform infrared spectroscopy—a pilot study of 60 samples. *Journal of Surgical Research* **179**, 33–38 (2013).

13. Zelig, U. *et al.* Early detection of breast cancer using total biochemical analysis of peripheral blood components: a preliminary study. *BMC Cancer* **15**, 408 (2015).

14. Griebe, M. *et al.* Infrared spectroscopy: a new diagnostic tool in Alzheimer disease. *Neurosci Lett* **420**, 29–33 (2007).

15. Perez-Guaita, D. *et al.* Evaluation of infrared spectroscopy as a screening tool for serum analysis: Impact of the nature of samples included in the calibration set. *Microchemical Journal* **106**, 202–211 (2013).

16. Jessen, T. E. *et al.* Simultaneous determination of glucose, triglycerides, urea, cholesterol, albumin and total protein in human plasma by Fourier transform infrared spectroscopy: direct clinical biochemistry without reagents. *Clin Biochem* **47**, 1306–1312 (2014).

17. Zou, Y. & Ma, G. A New Criterion to Evaluate Water Vapor Interference in Protein Secondary Structural Analysis by FTIR Spectroscopy. *Int J Mol Sci* **15**, 10018–10033 (2014).

18. Hoşafçi, G., Klein, O., Oremek, G. & Mäntele, W. Clinical chemistry without reagents? An infrared spectroscopic technique for determination of clinically relevant constituents of body fluids. *Anal Bioanal Chem* **387**, 1815–1822 (2007).

19. Petibois, C., Cazorla, G., Cassaigne, A. & Déléris, G. Plasma protein contents determined by Fourier-transform infrared spectrometry. *Clin Chem* **47**, 730–738 (2001).

20. Petibois, C. *et al.* Determination of glucose in dried serum samples by Fourier-transform infrared spectroscopy. *Clin Chem* **45**, 1530–1535 (1999).

21. Petibois, C., Melin, A.-M., Perromat, A., Cazorla, G. & Déléris, G. Glucose and lactate concentration determination on single microsamples by Fourier-transform infrared spectroscopy. *The Journal of Laboratory and Clinical Medicine* **135**, 210–215 (2000).

22. Shaw, R. A., Kotowich, S., Leroux, M. & Mantsch, H. H. Multianalyte Serum Analysis Using Mid-Infrared Spectroscopy. *Ann Clin Biochem* **35**, 624–632 (1998).

23. Liu, K. Z. *et al.* Comparison of infrared spectroscopic and fluorescence depolarization assays for fetal lung maturity. *Am J Obstet Gynecol* **183**, 181–187 (2000).

24. Liu, K. Z., Dembinski, T. C. & Mantsch, H. H. Rapid determination of fetal lung maturity from infrared spectra of amniotic fluid. *Am J Obstet Gynecol* **178**, 234–241 (1998).

25. Khaustova, S., Shkurnikov, M., Tonevitsky, E., Artyushenko, V. & Tonevitsky, A. Noninvasive biochemical monitoring of physiological stress by Fourier transform infrared saliva spectroscopy. *Analyst* **135**, 3183–3192 (2010).

26. Paolini, L. *et al.* Fourier-transform Infrared (FT-IR) spectroscopy fingerprints subpopulations of extracellular vesicles of different sizes and cellular origin. *J Extracell Vesicles* **9**,.

27. McGrane, S. D., Moore, D. S., Goodwin, P. M. & Dattelbaum, D. M. Quantitative Tradeoffs between Spatial, Temporal, and Thermometric Resolution of Nonresonant Raman Thermometry for Dynamic Experiments. *Appl Spectrosc* **68**, 1279–1288 (2014).

28. Mie, G. Beiträge zur Optik trüber Medien, speziell kolloidaler Metallösungen. *Annalen der Physik* **330**, 377–445 (1908).

29. Smith, E. & Dent, G. *Modern Raman spectroscopy: a practical approach*. (Wiley, 2019).

30. Wei, D., Chen, S. & Liu, Q. Review of Fluorescence Suppression Techniques in Raman Spectroscopy. *Applied Spectroscopy Reviews* **50**, 387–406 (2015).

31. Van Duyne, R. P., Jeanmaire, D. L. & Shriver, D. F. Mode-locked laser Raman spectroscopy. New technique for the rejection of interfering background luminescence signals. *Analytical Chemistry* **46**, 213–222 (1974).

32. Blacksberg, J., Alerstam, E., Maruyama, Y., Cochrane, C. J. & Rossman, G. R. Miniaturized time-resolved Raman spectrometer for planetary science based on a fast single photon avalanche diode detector array. *Appl. Opt., AO* **55**, 739–748 (2016).

33. Li, Z. & Deen, M. J. Towards a portable Raman spectrometer using a concave grating and a time-gated CMOS SPAD. *Opt. Express, OE* **22**, 18736–18747 (2014).

34. Nissinen, I. *et al.* A sub-ns time-gated CMOS single photon avalanche diode detector for Raman spectroscopy. in *2011 Proceedings of the European Solid-State Device Research Conference (ESSDERC)* 375–378 (2011). doi:10.1109/ESSDERC.2011.6044156.

35. Zumbusch, A., Holtom, G. R. & Xie, X. S. Three-Dimensional Vibrational Imaging by Coherent Anti-Stokes Raman Scattering. *Phys. Rev. Lett.* **82**, 4142–4145 (1999).

36. Day, J. P. R. *et al.* Quantitative Coherent Anti-Stokes Raman Scattering (CARS) Microscopy. *J. Phys. Chem. B* **115**, 7713–7725 (2011).

37. Hellwarth, R. W. Theory of Stimulated Raman Scattering. *Phys. Rev.* **130**, 1850–1852 (1963).

38. Rathore, A. S. Roadmap for implementation of quality by design (QbD) for biotechnology products. *Trends Biotechnol* **27**, 546–553 (2009).

39. Read, E. K. *et al.* Process analytical technology (PAT) for biopharmaceutical products: Part I. concepts and applications. *Biotechnology and Bioengineering* **105**, 276–284 (2010).

40. Read, E. K. *et al.* Process analytical technology (PAT) for biopharmaceutical products: Part II. Concepts and applications. *Biotechnology and Bioengineering* **105**, 285–295 (2010).

41. Li, B. *et al.* Rapid characterization and quality control of complex cell culture media solutions using raman spectroscopy and chemometrics. *Biotechnol Bioeng* **107**, 290–301 (2010).

42. Xu, Y. *et al.* Raman measurement of glucose in bioreactor materials. in *Biomedical Sensing, Imaging, and Tracking Technologies II* vol. 2976 10–19 (International Society for Optics and Photonics, 1997).

43. Lee, H. L. T., Boccazzi, P., Gorret, N., Ram, R. J. & Sinskey, A. J. In situ bioprocess monitoring of Escherichia coli bioreactions using Raman spectroscopy. *Vibrational Spectroscopy* **1–2**, 131–137 (2004).

44. Real time monitoring of multiple parameters in mammalian cell culture bioreactors using an in-line Raman spectroscopy probe - Abu-Absi - 2011 - Biotechnology and Bioengineering - Wiley Online Library. https://onlinelibrary.wiley.com/doi/full/10.1002/bit.23023.

45. Craven, S., Whelan, J. P. & Glennon, B. Glucose concentration control of a fed-batch mammalian cell bioprocess using a nonlinear model predictive controller. (2014) doi:10.1016/J.JPROCONT.2014.02.007.

46. Matthews, T. E. *et al.* Closed loop control of lactate concentration in mammalian cell culture by Raman spectroscopy leads to improved cell density, viability, and biopharmaceutical protein production. *Biotechnol Bioeng* **113**, 2416–2424 (2016).

47. De Beer, T. R. M. *et al.* In-line and real-time process monitoring of a freeze drying process using Raman and NIR spectroscopy as complementary process analytical technology (PAT) tools. *Journal of Pharmaceutical Sciences* **98**, 3430–3446 (2009).

48. Merivaara, A. *et al.* Preservation of biomaterials and cells by freeze-drying: Change of paradigm. *Journal of Controlled Release* **336**, 480–498 (2021).

49. Zhang, L. & Yu, D. Exosomes in cancer development, metastasis, and immunity. *Biochim Biophys Acta Rev Cancer* **1871**, 455–468 (2019).

50. Soares Martins, T. *et al.* Diagnostic and therapeutic potential of exosomes in Alzheimer's disease. *Journal of Neurochemistry* **156**, 162–181 (2021).

51. Kalluri, R. & LeBleu, V. S. The biology, function, and biomedical applications of exosomes. *Science* **367**, eaau6977 (2020).

52. Corsetti, S., Rabl, T., McGloin, D. & Nabi, G. Raman spectroscopy for accurately characterizing biomolecular changes in androgen-independent prostate cancer cells. *J Biophotonics* **11**, e201700166 (2018).

53. Aubertin, K. *et al.* Combining high wavenumber and fingerprint Raman spectroscopy for the detection of prostate cancer during radical prostatectomy. *Biomed Opt Express* **9**, 4294–4305 (2018).

54. Lernhardt, W. *et al.* 062 - Raman micro-spectroscopy: Potential for diagnosis and prediction of prostate cancer outcome. *European Urology Supplements* **15**, 145–146 (2016).

55. Evans, C. L. *et al.* Chemically-selective imaging of brain structures with CARS microscopy. *Opt. Express, OE* **15**, 12076–12087 (2007).

56. Li, S. *et al.* Noninvasive prostate cancer screening based on serum surface-enhanced Raman spectroscopy and support vector machine. *Appl. Phys. Lett.* **105**, 091104 (2014).

57. Baker, M. J. *et al.* Clinical applications of infrared and Raman spectroscopy: state of play and future challenges. *Analyst* **143**, 1735–1757 (2018).

58. Byrne, H. J., Knief, P., Keating, M. E. & Bonnier, F. Spectral pre and post processing for infrared and Raman spectroscopy of biological tissues and cells. *Chem. Soc. Rev.* **45**, 1865–1878 (2016).

59. Singh, I., Juneja, P., Kaur, B. & Kumar, P. Pharmaceutical Applications of Chemometric Techniques. *ISRN Analytical Chemistry* **2013**, e795178 (2013).

60. El-Mashtoly, S. F. *et al.* Label-free imaging of drug distribution and metabolism in colon cancer cells by Raman microscopy. *Analyst* **139**, 1155–1161 (2014).

61. Zhao, M., He, P., Rudek, M. A., Hidalgo, M. & Baker, S. D. Specific method for determination of OSI-774 and its metabolite OSI-420 in human plasma by using liquid chromatography–tandem mass spectrometry. *Journal of Chromatography B* **793**, 413–420 (2003).

62. Masters, A. R., Sweeney, C. J. & Jones, D. R. The quantification of erlotinib (OSI-774) and OSI-420 in human plasma by liquid chromatography–tandem mass spectrometry. *Journal of Chromatography B* **848**, 379–383 (2007).

63. Braslavsky, S. E. Glossary of terms used in photochemistry, 3rd edition (IUPAC Recommendations 2006). *Pure and Applied Chemistry* **79**, 293–465 (2007).

64. Ariola, F. S., Mudaliar, D. J., Walvick, R. P. & Heikal, A. A. Dynamics imaging of lipid phases and lipid-marker interactions in model biomembranes. *Phys. Chem. Chem. Phys.* **8**, 4517–4529 (2006).

65. Reid, P. C., Urano, Y., Kodama, T. & Hamakubo, T. Alzheimer's Disease: cholesterol, membrane rafts, isoprenoids and statins. *J Cell Mol Med* **11**, 383–392 (2007).

66. de Almeida, R. F. M., Loura, L. M. S. & Prieto, M. Membrane lipid domains and rafts: current applications of fluorescence lifetime spectroscopy and imaging. *Chem Phys Lipids* **157**, 61–77 (2009).

67. Levitt, J. A., Matthews, D. R., Ameer-Beg, S. M. & Suhling, K. Fluorescence lifetime and polarization-resolved imaging in cell biology. *Curr Opin Biotechnol* **20**, 28–36 (2009).

68. Duncan, R. R. Fluorescence lifetime imaging microscopy (FLIM) to quantify protein-protein interactions inside cells. *Biochem Soc Trans* **34**, 679–682 (2006).

69. Liu, S., Gao, J., Liu, K. & Zhang, H.-L. Microbiota-gut-brain axis and Alzheimer's disease: Implications of the blood-brain barrier as an intervention target. *Mech Ageing Dev* **199**, 111560 (2021).

70. Crewe, C. *et al.* Extracellular vesicle-based interorgan transport of mitochondria from energetically stressed adipocytes. *Cell Metab* **33**, 1853-1868.e11 (2021).

71. Tatischeff, I., Larquet, E., Falcón-Pérez, J. M., Turpin, P.-Y. & Kruglik, S. G. Fast characterisation of cell-derived extracellular vesicles by nanoparticles tracking analysis, cryo-electron microscopy, and Raman tweezers microspectroscopy. *J Extracell Vesicles* **1**, (2012).

72. Pascucci, L. *et al.* Paclitaxel is incorporated by mesenchymal stromal cells and released in exosomes that inhibit in vitro tumor growth: a new approach for drug delivery. *J Control Release* **192**, 262–270 (2014).

73. Koponen, A. *et al.* Label-free characterization and real-time monitoring of cell uptake of extracellular vesicles. *Biosens Bioelectron* **168**, 112510 (2020).

74. Colombo, M., Raposo, G. & Théry, C. Biogenesis, Secretion, and Intercellular Interactions of Exosomes and Other Extracellular Vesicles. *Annual Review of Cell and Developmental Biology* **30**, 255–289 (2014).

75. Clancy, J. W., Boomgarden, A. C. & D'Souza-Schorey, C. Profiling and promise of supermeres. *Nat Cell Biol* **23**, 1217–1219 (2021).

76. Zhang, H. *et al.* Identification of distinct nanoparticles and subsets of extracellular vesicles by asymmetric flow field-flow fractionation. *Nat Cell Biol* **20**, 332–343 (2018).

77. Rautaniemi, K. *et al.* Addressing challenges in the removal of unbound dye from passively labelled extracellular vesicles. *Nanoscale Adv.* **4**, 226–240 (2021).

78. Skotland, T., Hessvik, N. P., Sandvig, K. & Llorente, A. Exosomal lipid composition and the role of ether lipids and phosphoinositides in exosome biology. *J Lipid Res* **60**, 9–18 (2019).

79. Raposo, G. & Stoorvogel, W. Extracellular vesicles: Exosomes, microvesicles, and friends. *J Cell Biol* **200**, 373–383 (2013).

80. Shifrin, D. A., Demory Beckler, M., Coffey, R. J. & Tyska, M. J. Extracellular vesicles: communication, coercion, and conditioning. *Mol Biol Cell* **24**, 1253–1259 (2013).

81. Muralidharan-Chari, V., Clancy, J. W., Sedgwick, A. & D'Souza-Schorey, C. Microvesicles: mediators of extracellular communication during cancer progression. *J Cell Sci* **123**, 1603–1611 (2010).

82. Tricarico, C., Clancy, J. & D'Souza-Schorey, C. Biology and biogenesis of shed microvesicles. *Small GTPases* **8**, 220–232 (2016).

83. Hugel, B., Martínez, M. C., Kunzelmann, C. & Freyssinet, J.-M. Membrane microparticles: two sides of the coin. *Physiology (Bethesda)* **20**, 22–27 (2005).

84. Batagov, A. O. & Kurochkin, I. V. Exosomes secreted by human cells transport largely mRNA fragments that are enriched in the 3'-untranslated regions. *Biol Direct* **8**, 12 (2013).

85. O'Brien, K., Breyne, K., Ughetto, S., Laurent, L. C. & Breakefield, X. O. RNA delivery by extracellular vesicles in mammalian cells and its applications. *Nat Rev Mol Cell Biol* **21**, 585–606 (2020).

86. Krafft, C. *et al.* A specific spectral signature of serum and plasma-derived extracellular vesicles for cancer screening. *Nanomedicine: Nanotechnology, Biology and Medicine* **13**, 835–841 (2017).

87. Raposo, G. *et al.* B lymphocytes secrete antigen-presenting vesicles. *J Exp Med* **183**, 1161–1172 (1996).

88. Iraci, N., Leonardi, T., Gessler, F., Vega, B. & Pluchino, S. Focus on Extracellular Vesicles: Physiological Role and Signalling Properties of Extracellular Membrane Vesicles. *Int J Mol Sci* **17**, (2016).

89. Mittelbrunn, M. *et al.* Unidirectional transfer of microRNA-loaded exosomes from T cells to antigen-presenting cells. *Nat Commun* **2**, 282 (2011).

90. Schillaci, O. *et al.* Exosomes from metastatic cancer cells transfer amoeboid phenotype to non-metastatic cells and increase endothelial permeability: their emerging role in tumor heterogeneity. *Sci Rep* **7**, 4711 (2017).

91. Yokoi, A. *et al.* Malignant extracellular vesicles carrying MMP1 mRNA facilitate peritoneal dissemination in ovarian cancer. *Nat Commun* **8**, 14470 (2017).

92. Dorayappan, K. D. P. *et al.* Hypoxia-induced exosomes contribute to a more aggressive and chemoresistant ovarian cancer phenotype: a novel mechanism linking STAT3/Rab proteins. *Oncogene* **37**, 3806–3821 (2018).

93. Dörsam, B. *et al.* Hodgkin Lymphoma-Derived Extracellular Vesicles Change the Secretome of Fibroblasts Toward a CAF Phenotype. *Frontiers in Immunology* **9**, 1358 (2018).

94. Salimu, J. *et al.* Dominant immunosuppression of dendritic cell function by prostate-cancer-derived exosomes. *J Extracell Vesicles* **6**, 1368823 (2017).

95. Kosaka, N., Yoshioka, Y., Fujita, Y. & Ochiya, T. Versatile roles of extracellular vesicles in cancer. *J Clin Invest* **126**, 1163–1172.

96. Théry, C., Amigorena, S., Raposo, G. & Clayton, A. Isolation and Characterization of Exosomes from Cell Culture Supernatants and Biological Fluids. *Current Protocols in Cell Biology* **30**, 3.22.1-3.22.29 (2006).

97. Cantin, R., Diou, J., Bélanger, D., Tremblay, A. M. & Gilbert, C. Discrimination between exosomes and HIV-1: Purification of both vesicles from cell-free supernatants. *Journal of Immunological Methods* **338**, 21–30 (2008).

98. Tauro, B. J. *et al.* Comparison of ultracentrifugation, density gradient separation, and immunoaffinity capture methods for isolating human colon cancer cell line LIM1863-derived exosomes. *Methods* **56**, 293–304 (2012).

99. Brownlee, Z., Lynn, K. D., Thorpe, P. E. & Schroit, A. J. A novel "salting-out" procedure for the isolation of tumor-derived exosomes. *Journal of Immunological Methods* **407**, 120–126 (2014).

100. Nordin, J. Z. *et al.* Ultrafiltration with size-exclusion liquid chromatography for high yield isolation of extracellular vesicles preserving intact biophysical and functional properties. *Nanomedicine* **11**, 879–883 (2015).

101. Lobb, R. J. *et al.* Optimized exosome isolation protocol for cell culture supernatant and human plasma. *J Extracell Vesicles* **4**, 27031 (2015).

102. Stranska, R. *et al.* Comparison of membrane affinity-based method with size-exclusion chromatography for isolation of exosome-like vesicles from human plasma. *Journal of Translational Medicine* **16**, 1 (2018).

103. Théry, C. *et al.* Minimal information for studies of extracellular vesicles 2018 (MISEV2018): a position statement of the International Society for Extracellular Vesicles and update of the MISEV2014 guidelines. *Journal of Extracellular Vesicles* **7**, 1535750 (2018).

104. Royo, F., Théry, C., Falcón-Pérez, J. M., Nieuwland, R. & Witwer, K. W. Methods for Separation and Characterization of Extracellular Vesicles: Results of a Worldwide Survey Performed by the ISEV Rigor and Standardization Subcommittee. *Cells* **9**, (2020).

105. Sitar, S. *et al.* Size Characterization and Quantification of Exosomes by Asymmetrical-Flow Field-Flow Fractionation. *Anal. Chem.* **87**, 9225–9233 (2015).

106. Rupert, D. L. M. *et al.* Determination of exosome concentration in solution using surface plasmon resonance spectroscopy. *Anal. Chem.* **86**, 5929–5936 (2014).

107. Im, H. *et al.* Label-free detection and molecular profiling of exosomes with a nano-plasmonic sensor. *Nat Biotechnol* **32**, 490–495 (2014).

108. Szentirmai, V. *et al.* Reagent-free total protein quantification of intact extracellular vesicles by attenuated total reflection Fourier transform infrared (ATR-FTIR) spectroscopy. *Anal Bioanal Chem* **412**, 4619–4628 (2020).

109. Eryilmaz, M., Zengin, A., Boyaci, I. H. & Tamer, U. Rapid quantification of total protein with surface-enhanced Raman spectroscopy using o-phthalaldehyde. *Journal of Raman Spectroscopy* **48**, 653–658 (2017).

110. Gualerzi, A. *et al.* Raman spectroscopy as a quick tool to assess purity of extracellular vesicle preparations and predict their functionality. *Journal of Extracellular Vesicles* **8**, 1568780 (2019).

111. Mihály, J. *et al.* Characterization of extracellular vesicles by IR spectroscopy: Fast and simple classification based on amide and CH stretching vibrations. *Biochimica et Biophysica Acta (BBA) - Biomembranes* **1859**, 459–466 (2017).

112. Ford, T., Graham, J. & Rickwood, D. Iodixanol: A Nonionic Iso-osmotic Centrifugation Medium for the Formation of Self-Generated Gradients. *Analytical Biochemistry* **220**, 360–366 (1994).

113. Smith, Z. J. *et al.* Single exosome study reveals subpopulations distributed among cell lines with variability related to membrane content. *Journal of Extracellular Vesicles* **4**, 28533 (2015).

114. Kim, S. Y., Khanal, D., Tharkar, P., Kalionis, B. & Chrzanowski, W. None of us is the same as all of us: resolving the heterogeneity of extracellular vesicles using single-vesicle, nanoscale characterization with resonance enhanced atomic force microscope infrared spectroscopy (AFM-IR). *Nanoscale Horiz.* **3**, 430–438 (2018).

115. Lee, W. *et al.* Label-Free Prostate Cancer Detection by Characterization of Extracellular Vesicles Using Raman Spectroscopy. *Anal. Chem.* **90**, 11290–11296 (2018).

116. Horgan, C. C. *et al.* Molecular imaging of extracellular vesicles in vitro via Raman metabolic labelling. *J. Mater. Chem. B* **8**, 4447–4459 (2020).

117. Kögler, M., Itkonen, J., Viitala, T. & Casteleijn, M. G. Assessment of recombinant protein production in E. coli with Time-Gated Surface Enhanced Raman Spectroscopy (TG-SERS). *Sci Rep* **10**, 2472 (2020).

118. Stremersch, S. *et al.* Identification of Individual Exosome-Like Vesicles by Surface Enhanced Raman Spectroscopy. *Small* **12**, 3292–3301 (2016).

119. Wang, J. *et al.* Tracking extracellular vesicle phenotypic changes enables treatment monitoring in melanoma. *Sci Adv* **6**, eaax3223 (2020).

120. Kessler, R. J. & Fanestil, D. D. Interference by lipids in the determination of protein using bicinchoninic acid. *Analytical Biochemistry* **159**, 138–142 (1986).

121. Puhka, M. *et al.* KeepEX, a simple dilution protocol for improving extracellular vesicle yields from urine. *European Journal of Pharmaceutical Sciences* **98**, 30–39 (2017).

122. Vogt, F. G. & Strohmeier, M. Confocal UV and Resonance Raman Microscopic Imaging of Pharmaceutical Products. *Mol. Pharmaceutics* **10**, 4216–4228 (2013).

123. Mylonas, E. & Svergun, D. I. Accuracy of molecular mass determination of proteins in solution by small-angle X-ray scattering. *J Appl Cryst* **40**, s245–s249 (2007).

124. Zou, G., Liu, Z. & Wang, C. Flow injection analysis methods for determination of diffusion coefficients. *Analytica Chimica Acta* **350**, 359–363 (1997).

125. Meulemans, A., Paycha, F., Hannoun, P. & Vulpillat, M. Measurement and clinical and pharmacokinetic implications of diffusion coefficients of antibiotics in tissues. *Antimicrob Agents Chemother* **33**, 1286–1290 (1989).

126. Ye, F. *et al.* Real-time UV imaging of drug diffusion and release from Pluronic F127 hydrogels. *European Journal of Pharmaceutical Sciences* **43**, 236–243 (2011).

127. Kuhar, N., Sil, S., Verma, T. & Umapathy, S. Challenges in application of Raman spectroscopy to biology and materials. *RSC Adv.* **8**, 25888–25908 (2018).

128. Yu, Y., Ramachandran, P. V. & Wang, M. C. Shedding new light on lipid functions with CARS and SRS microscopy. *Biochimica et Biophysica Acta (BBA) - Molecular and Cell Biology of Lipids* **1841**, 1120–1129 (2014).

129. Gualerzi, A. *et al.* Raman spectroscopy uncovers biochemical tissue-related features of extracellular vesicles from mesenchymal stromal cells. *Scientific Reports* **7**, 1–11 (2017).

130. Park, J. *et al.* Exosome Classification by Pattern Analysis of Surface-Enhanced Raman Spectroscopy Data for Lung Cancer Diagnosis. *Anal Chem* **89**, 6695–6701 (2017).

131. Ferreira, N. *et al.* Label-Free Nanosensing Platform for Breast Cancer Exosome Profiling. *ACS Sens.* **4**, 2073–2083 (2019).

132. Samoylenko, A. *et al.* Time-gated Raman spectroscopy and proteomics analyses of hypoxic and normoxic renal carcinoma extracellular vesicles. *Sci Rep* **11**, 19594 (2021).

133. Dazzi, A. *et al.* AFM–IR: Combining Atomic Force Microscopy and Infrared Spectroscopy for Nanoscale Chemical Characterization. *Appl Spectrosc* **66**, 1365–1384 (2012).

134. Ruan, Z. *et al.* Alzheimer's disease brain-derived extracellular vesicles spread tau pathology in interneurons. *Brain* **144**, 288–309 (2021).

135. Saari, H. *et al.* FLIM reveals alternative EV-mediated cellular up-take pathways of paclitaxel. *Journal of Controlled Release* **284**, 133–143 (2018).

136. Tian, T. *et al.* Exosome Uptake through Clathrin-mediated Endocytosis and Macropinocytosis and Mediating miR-21 Delivery. *J Biol Chem* **289**, 22258–22267 (2014).

137. Kamerkar, S. *et al.* Exosomes facilitate therapeutic targeting of oncogenic KRAS in pancreatic cancer. *Nature* **546**, 498–503 (2017).

138. Dehghani, M. & Gaborski, T. R. Fluorescent labeling of extracellular vesicles. *Methods Enzymol* **645**, 15–42 (2020).

139. Morales-Kastresana, A. *et al.* Labeling Extracellular Vesicles for Nanoscale Flow Cytometry. *Sci Rep* **7**, 1878 (2017).

140. Pužar Dominkuš, P. *et al.* PKH26 labeling of extracellular vesicles: Characterization and cellular internalization of contaminating PKH26 nanoparticles. *Biochim Biophys Acta Biomembr* **1860**, 1350–1361 (2018).

141. Kooijmans, S. A. A. *et al.* Display of GPI-anchored anti-EGFR nanobodies on extracellular vesicles promotes tumour cell targeting. *Journal of Extracellular Vesicles* **5**, 31053 (2016).

142. di Cagno, M. P. *et al.* Experimental Determination of Drug Diffusion Coefficients in Unstirred Aqueous Environments by Temporally Resolved Concentration Measurements. *Mol. Pharmaceutics* **15**, 1488–1494 (2018).

143. Pelletier, M. J. Quantitative Analysis Using Raman Spectrometry. *Appl Spectrosc* **57**, 20A-42A (2003).